Parallel Radiofrequency Transmission for Safe Magnetic Resonance Imaging of Deep Brain Stimulation Patients at 3 Tesla

By: Benson Yang

Bachelor of Science, Queen's University 2004

Master of Applied Science, McMaster University 2012

A thesis is submitted to the School of Graduate Studies in partial fulfillment of the requirements for the degree of Doctor of Philosophy

McMaster University
Hamilton, Ontario

Doctor of Philosophy (2023)
(Department of Electrical and Computer Engineering)

TITLE: Parallel Radiofrequency Transmission for Safe Magnetic Resonance Imaging of Deep Brain Stimulation Patients at 3 Tesla

AUTHOR: Benson Yang
B.Sc. Queen's University, Kingston, Ontario, Canada
M.A.Sc. McMaster University, Hamilton, Ontario, Canada

SUPERVISOR: Prof. Chih-Hung (James) Chen

NUMBER OF PAGES: xxi, 150

Thesis Motivation

Deep brain stimulation (DBS) improves the quality of life for patients suffering from neurological disorders such as Parkinson's disease and, more recently, psychiatric/cognitive disorders such as depression and addiction. This treatment option involves the implantation of an implantable pulse generator (or neurostimulator) and leads (or electrodes) implanted deep within the human brain. Magnetic resonance imaging (MRI) is a powerful diagnostic tool that offers superior soft tissue contrast and is routinely used in clinics for neuroimaging applications. MRI is advantageous in DBS pre-surgical planning as precise lead placement within the brain is essential for optimal treatment outcomes. DBS patients can also benefit from post-surgery MRI, and studies have shown that DBS patients are more likely to require MRI within 5-10 years post-surgery. However, imaging DBS patients is restricted by substantial safety concerns that arise from localized electric charge accumulation along the implanted device during resonant radiofrequency (RF) excitation, which can potentially lead to tissue heating and bodily damage. With the technological advancement of ultra-high field (UHF) MRI systems and a growing DBS patient population, DBS MRI safety will become increasingly problematic in the future and needs to be addressed.

Parallel RF transmission (pTx) is a promising technology that utilizes multiple transmit channels to generate a desired electromagnetic profile during MRI RF excitation. Several proof-of-concept studies successfully demonstrated its efficacy in creating a "safe mode" of imaging that minimizes the localized RF heating effects. However, pTx MRI systems are not easily accessible and are often custom-built and integrated onto existing MRI systems. Consequently, it adds system characterization and verification complexity to the DBS MRI safety problem. System channel count is also an important consideration as implementation costs can be very high, and the impact of system transmit channel count remains unexplored. Furthermore, in practice, DBS patients with motor-related disorders will impact the pTx MRI system's ability to precisely generate these safe mode electromagnetic profiles. Commercial DBS devices (i.e., the neurostimulator and leads) are manufactured with fixed dimensions, and the caring surgeon typically manages the surgical orientation of the implanted DBS device and leads. Therefore, lead trajectories can vary hospital-

to-hospital. As a result, standard phantoms, i.e., the ASTM International Standard, used in safety verification experiments may not be suitable for DBS MRI applications.

To advance DBS patient safety in MRI, this thesis studied the implant heating effects of pTx system uncertainty, system channel count, patient motion on a novel pTx MRI research platform and its associated safe mode of imaging. It developed a new anthropomorphic heterogeneous phantom to improve safety verification experiments.

Thesis Contribution

The research work undertaken in this thesis has resulted in several peer-reviewed journal and conference publications.

Journal Publications:

1. B. Yang, C.-H. Chen, and S. J. Graham, "Technical note: system uncertainty on four- and eight-channel parallel RF transmission for safe MRI of deep brain stimulation," *Med. Phys*. 50(9):3745-3751, 2023.
2. B. Yang, C.-H. Chen, and S. J. Graham, "RF heating dependence of head model positioning using 4-channel parallel transmission MRI and a deep brain stimulation construct," *IEEE Letters on Electromagnetic Compatibility Practice and Applications*, vol. 4, no. 3, pp. 83-87, 2022. Doi: 10.1109/LEMCPA.2022.3180974.
3. B. Yang, F. Tam, B. Davidson, P. S. Wei, C. Hamani, N. Lipsman, C.-H. Chen, and S. J. Graham, "Technical note: An anthropomorphic phantom with implanted neurostimulator for investigation of MRI safety," *Med. Phys.*, 47(8):3745-3751, 2020.

Conference Publications:

1. B. Yang, C.-H. Chen, and S. J. Graham, "Safety of 4-channel parallel radiofrequency transmission MRI at 3 T: Effects of system uncertainty and system failure pertinent to deep brain stimulation," *Proc. 30th scientific meeting, Intl. Soc. Mag. Reson. Med.*, London UK, 2022, p. 2813.
2. B. Yang, F. Tam, B. Davidson, C. Hamani, N. Lipsman, C.-H. Chen, and S. J. Graham, "An anthropomorphic phantom for deep brain stimulation MRI safety investigations," *Proc. 29th scientific meeting, Intl. Soc. Mag. Reson. Med.*, Virtual, 2021, p. 2297.
3. B. Yang, F. Tam, B. Davidson, C. Hamani, N. Lipsman, C.-H. Chen, and S. J. Graham, "MRI safety of deep brain stimulation devices: Radiofrequency heating of a commercial lead and an insulated copper wire," *Proc. 28th scientific meeting, Intl. Soc. Mag. Reson. Med.*, Virtual, 2020, p. 4182.

4. B. Yang, C.-H. Chen, and S. J. Graham, "Signal-to-noise measurement of a 4-channel parallel radiofrequency transmission system for MRI at 3 T", *Proc. 28th scientific meeting, Intl. Soc. Mag. Reson. Med.*, Virtual, 2020, p. 4035.

Thesis Organization

This thesis is divided into six chapters. Chapter 1 briefly introduces DBS and MRI physics and discusses the MRI safety risks associated with imaging DBS patients, primarily the risk of RF power coupling onto the implanted device, causing localized hot spots capable of damaging adjacent tissue. It also introduces the concept of an emerging technology known as parallel RF transmission (or pTx) and the basic theory of a novel pTx MRI method that enables a safe mode of imaging that may potentially address this DBS safety concern. The chapter concludes with the research contributions and organization of this thesis.

Based on the theory of pTx MRI described in Chapter 1, Chapter 2 introduces a novel flexible pTx MRI research platform to enable experimental studies. It presents the hardware complexities of the pTx MRI platform and the importance of studying the practical limitations of hardware devices. It also discusses the hardware impact on the generation of the presented pTx MRI safe mode and its safety implications on DBS patient imaging. It evaluates the DBS implant heating effects for system uncertainty on the proposed 4-channel pTx MRI system based on the technical specifications of the presented pTx MRI research platform. In addition, it presents the study of a worst-case imaging scenario and the effect of system channel failure for the pTx setup.

After understanding the limitation and uncertainties of the hardware, Chapter 3 investigates the effect of system channel counts on DBS implant safety. Due to the very high cost of enabling pTx technology on MRI systems, it is crucial to determine the optimal system configuration capable of effectively minimizing the MRI safety risks and the concerns associated with system uncertainty while maintaining economic feasibility and system design simplicity. The chapter concludes with the design, fabrication, and characterization of a prototype 8-channel head coil for pTx MRI experiments.

After we obtained an optimum system configuration, Chapter 4 turns our attention to the implications of patient motion on image reconstruction in MRI. Since safe mode pTx MRI is derived for a subject from a fixed position in space. Consequently, any displacement from this reference position will alter the electromagnetic distribution and may alter the system parameters required for safe mode. More importantly, it may result in an unsafe imaging condition,

particularly for DBS patients suffering from motor-related symptoms. Therefore, it is crucial to study patient motion effects. Chapter 4 investigates the DBS implant heating in proof-of-concept in 4-channel pTx MRI safe mode for typical DBS patient head movements and rotations. Simulation and experiment are conducted to assess the robustness of the presented pTx safe mode technique.

To better replicate the actual lead trajectories of DBS patients, Chapter 5 presents the design and development of an anthropomorphic phantom. It starts with a simple experiment using a conventional method to evaluate and compare the DBS implant heating effects. It also compares the use of copper wire as a DBS lead substitute in two lead geometries. These simple experiments served as an initial step in assessing the need for improved phantom structures in DBS safety studies and demonstrated the advantage of using real DBS devices. It is then followed by a detailed description of the design and development of a novel anthropomorphic heterogeneous phantom with MRI experiments to evaluate its utility. The preliminary results suggest that advanced phantoms with improved realism are advisable for DBS MRI safety experiments.

Finally, Chapter 6 concludes this thesis and discusses future study topics relevant to the main results presented in each chapter. It is then followed by general recommendations relevant to the presented pTx MRI safe mode technique and DBS patient safety.

Acknowledgements

I would first like to thank my academic supervisor, Prof. Chih-Hung Chen, for his support and the opportunity to continue my academic journey with him. I have learned a lot and matured as a researcher under his guidance. I would also like to thank Prof. Simon J. Graham from the University of Toronto, my supervisor from Sunnybrook Research Institute for bringing this clinical problem to my attention and supporting this unique collaboration between two high-level institutions. I have learned a great deal over the years, and working with both of you has been a great honour.

I would like to thank the members of my supervisory committee, Prof. Jamal Deen and Prof. Natalia Nikolova, for all their advice and contributions to this thesis and Cheryl Gies for helping me navigate through the logistics of the university.

Finally, I would like to thank my family for their patience and support. As a final remark, a message to my daughters, Mackenzie and Kara; never stop learning, dream, believe, and work hard, and you will achieve.

Table of Contents

List of Figures

List of Tables

Chapter 1

Introduction

Magnetic resonance imaging (MRI) is an essential diagnostic tool for overall patient healthcare management, especially for neuroimaging applications. Deep brain stimulation (DBS) is a highly effective treatment option for patients suffering from neurological disorders such as Parkinson's disease (PD). It involves the surgical implantation of an implantable pulse generator (IPG) and long conductive electrodes to the targeted deep brain anatomy. DBS has been widely used as a treatment option for motor-related disorders [1], and more recently, it has shown the quality of life benefits for patients suffering from addiction and depression [2]. MRI is advantageous for pre-surgical planning patients who opt for DBS treatment because of the superior soft tissue contrast in MRI images. As a result, better targeting of brain anatomy during DBS surgery and patient outcomes can be expected [3]. Similarly, there are post-surgical benefits for using MRI to evaluate surgical outcomes, disease progression, or other underlying medical complications [4]. It is also known that DBS patients are more susceptible to developing other medical conditions in the future, which are likely to require advanced imaging such as MRI [5]. However, there is a significant safety concern for DBS patients to undergo MRI due to the risk of induced RF heating effects, causing potentially dangerous levels of electrical charge to accumulate along and scatter from the implanted DBS device. Routine clinical MRI duration can last up to 90 minutes, and as a result, temperature elevations can reach levels capable of damaging adjacent human tissue and, in the worst-case, necrosis [6]. The safety risks are apparent in clinical MRI systems (i.e., 1.5 and 3 T) and will become increasingly important in the future with the eventual adoption of ultra-high field (UHF) MRI systems (i.e., 7 T and above) in clinics.

With the growth in DBS treatment utility in patients, progression to UHF MRI, and increasing human life expectancy, there is an immediate need and future importance to address this safety issue. This thesis focuses on the emergence of a new technology known as Parallel Radiofrequency Transmission (pTx), the continual development of a specialized pTx safe mode technique, and the technical and clinical challenges to advance the technology towards a goal of safe pTx MRI of DBS patients in the future.

1.1 Deep Brain Stimulation

DBS became a treatment option in the 1990s for patients diagnosed with PD [1, 7]. PD is a neurodegenerative disease affecting the central nervous system, causing motor impairments such as tremors, rigidity, difficulty walking, and general cognitive decline [8]. The symptoms of PD are caused by the breakdown or death of specific neurons in the motor-control linking pathways of the brain [9]. Prior to the emergence of DBS, the treatment options available to PD patients were dopaminergic medications or ablation therapy, which involves a permanent lesion in the brain target to assist with the severity of the motor-related impairment. Drug-related side effects and body tolerance remain a concern for long-term PD patients, and also, ablation therapy brain lesions can be misplaced and are permanent. However, recent developments in magnetic resonance-guided focused ultrasound have improved the efficacy of ablation therapy, but concerns about adverse side effects still remain [7, 10].

DBS has been highly successful in treating patients with PD; 70% of patients have reported improving symptoms from slowness, rigidity, tremor, and the ability to reduce medication, thus lessening side effects, including dyskinesia (i.e., uncontrolled wiggling) [11]. DBS is also known to be an effective treatment option for other movement disorders such as essential tremors (i.e., involuntary rhythmic tremors in the head, arms, and hands) and dystonia (i.e., involuntary movement and prolonged muscle contractions). Patients with DBS have reported very good long-term disease management and overall better quality of life and sleep [12]. Recent studies show promising initial success in treating addiction and depression, expanding the DBS utility to the potential treatment of psychiatric disorders in the future [2].

A DBS device consists of an IPG or neurostimulator used for electrical pulse delivery and is typically placed underneath the skin in the upper chest region of a patient. Long conductive leads attached to the IPG (on one end) with an exposed electrode near the lead tip (on the other end) are implanted deep within the brain, providing a therapeutic effect without drug medication or permanent brain lesions. A stereotactic frame is attached to the patient to prevent head movements and assist with electrode positioning and alignment during surgery. It also assists with pre-surgery local anesthesia injections. Fig. 1-1 displays a DBS patient setup with a typical stereotactic frame attached.

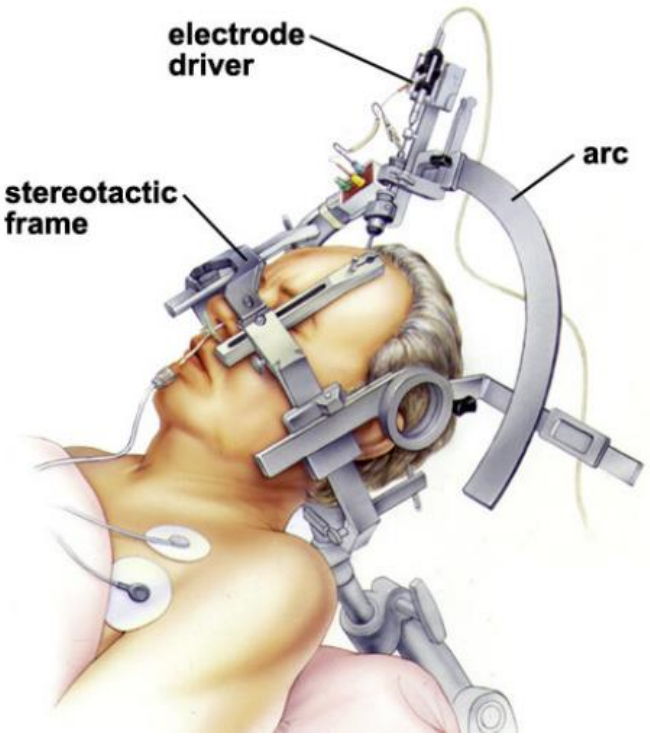

Fig. 1-1: Typical patient setup with a stereotactic frame attached.
(Photo from: https://www.iowaclinic.com/webres/File/deep-brain-stim.pdf)

There are three main brain targets known for effective DBS treatment of movement disorders; the ventral intermediate nucleus (Vim), which is effective for essential tremors, the subthalamic nucleus (STN), which is commonly used for treating PD and the internal globus pallidus (GPi), which is effective for dystonia and also PD. Fig. 1-2 illustrates the typical placement of the DBS device in a patient and a cross-sectional view of the human brain that highlights the locations of the three main brain targets common to DBS patients. Precise placement of DBS lead(s) into these small and deep brain regions is essential for optimal patient benefits [13]. Because of the complex interconnections of the human brain, typical DBS leads are designed with multiple programmable electrodes, providing therapeutic flexibility, for example, different electrode activation combinations and possible electrode placement coverage of multiple brain targets and, to a lesser extent, a surgical placement error margin to improve surgical outcomes. Fig. 1-3 (a) displays a typical DBS lead with four exposed electrodes.

Medical imaging plays an important role throughout DBS surgery for guidance, lead positioning, and general patient safety. Patients typically undergo a pre-surgical scan to aid

neurosurgeons with brain mapping for better implant placement and intra-operative scans for lead placement verification and to monitor surgical complications such as hemorrhaging. Using MRI over other imaging modalities, such as computed tomography (CT), can be advantageous, given its excellent soft tissue contrast. Fig. 1.3 (b) displays a post-operative, longitudinal relaxation time-weighted MRI brain image of a DBS patient for STN targeting. Because of the higher-quality MRI images, clinicians can easily identify surgery-related complications and confirm the correct lead depth and position. However, at present, there is a significant safety concern for DBS patients to undergo MRI post-surgery, and it is a clinical challenge that requires immediate attention. These topics and a promising technology capable of addressing this concern will be discussed in the proceeding sections.

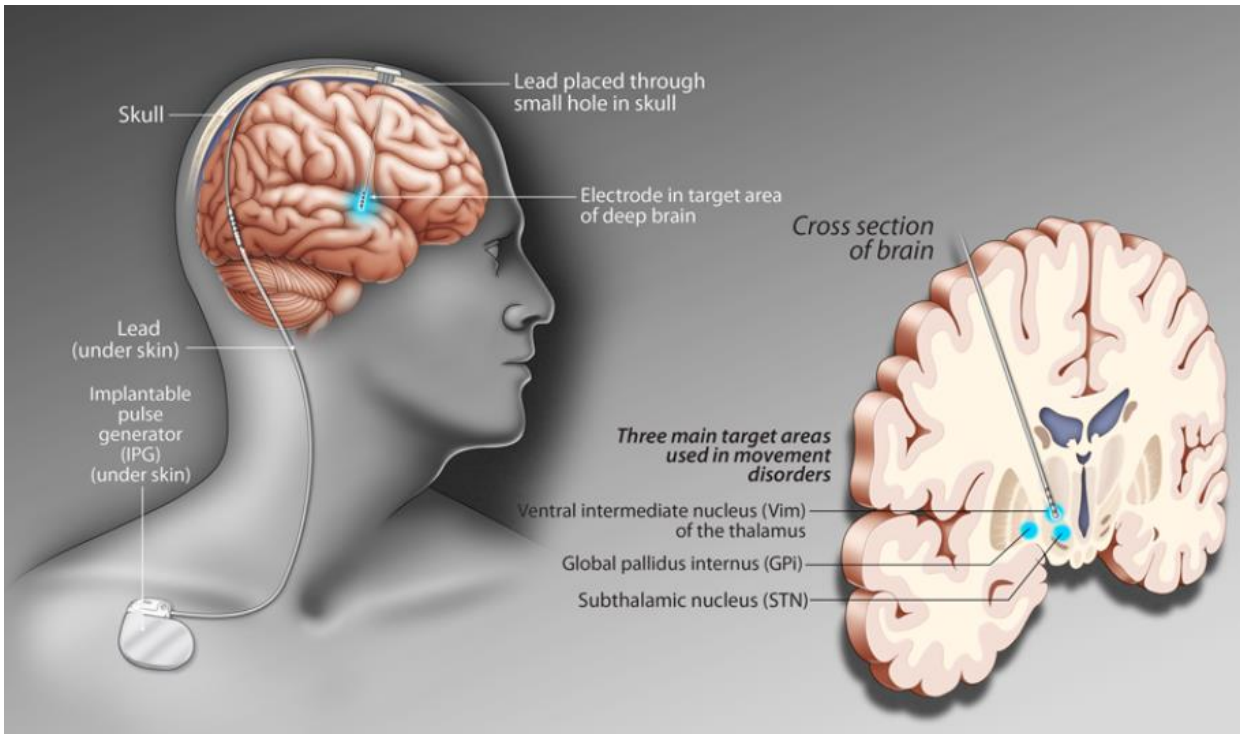

Fig. 1-2: Typical deep brain stimulation device placement in a patient and cross-section of the human brain that highlights the common brain targets for patients with movement disorders.
(Photo from: https://www.healthplexus.net/iTherapies/deep-brain-stimulation)

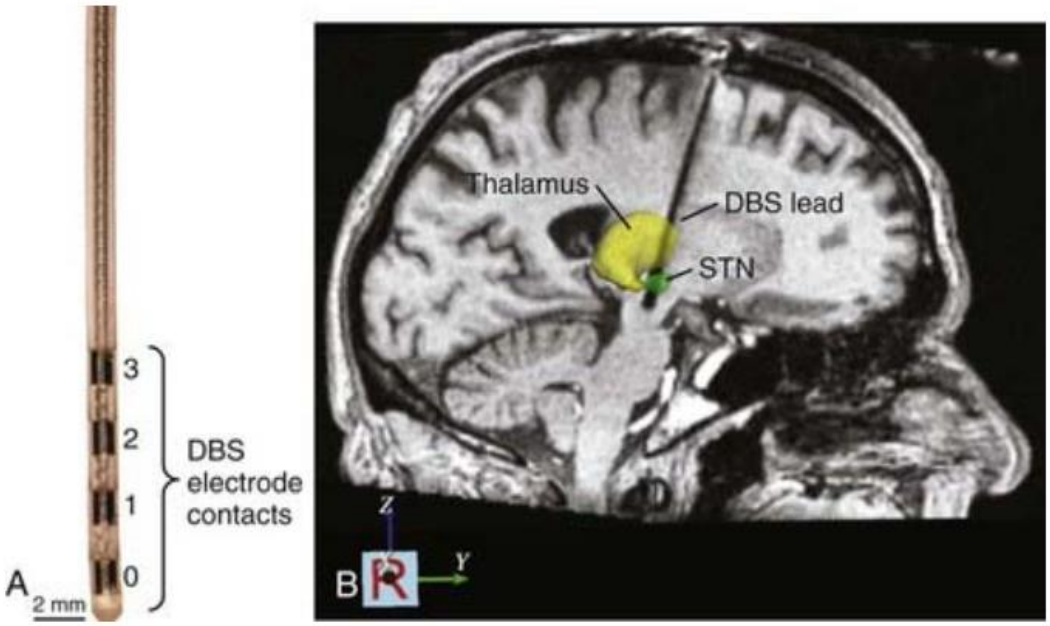

Fig. 1-3: (a) A typical deep brain stimulation lead (Medtronic model 3387) with four programable electrodes for flexible treatment options and targeting of brain regions. (b) Post-operative, longitudinal relaxation time-weighted magnetic resonance image to verify lead depth and position. DBS = deep brain stimulation; STN = subthalamic nucleus. (Photo from: https://clinicalgate.com/deep-brain-stimulation-2/#bib4)

1.2 MRI Physics

MRI is a powerful non-invasive and non-ionizing imaging modality that offers superior soft tissue contrast, making it a safer alternative to ionizing modalities such as x-ray and CT imaging. MRI is based on nuclear magnetic resonance theory, particularly the nuclear spin phenomena. MRI images are derived from the quantum mechanical interactions between specific atomic nuclei and external magnetic fields. The human body contains an abundance of hydrogen atoms that possess nuclear spin enabling high-quality MRI images to be reconstructed. When the human body enters a large static magnetic field (B_0), the nuclear spins within the body align parallel or anti-parallel to this magnetic field and undergo precession around B_0 at a frequency known as the Larmor frequency ($\omega_0 = \gamma B_0$, where γ is the gyromagnetic ratio, a nuclear constant). As a result, a net magnetization (M) is created from the magnetic moment of each nuclear spin. By perturbing M with additional magnetic fields that vary in time and space, nuclei begin to tilt away from the axis of B_0 and lead to producing signals that enable image formation. The entire system is governed by the Bloch equation, which is [14],

$$\frac{dM}{dt} = \gamma M \times B - \frac{M_x\hat{i} - M_y\hat{j}}{T_2} - \frac{(M_z - M_0)\hat{k}}{T_1}, \quad (1\text{-}1)$$

where M is the time-dependent magnetization of the subject, M_0 is the initial magnetization, $M_{x,y,z}$ is the transverse and longitudinal relaxation of M, B is the time-dependent applied magnetic field, and T_1 and T_2 are relaxation constants. The additional magnetic fields used in MRI are known as gradient fields, which are time and position-dependent magnetic fields oriented in the z-direction (i.e., $B = B_0 + B_{gradient}(r,t))\hat{k}$, where r is the position and t is time). The applied gradient is a temporary and spatially varying precession frequency and is used for spatial encoding of detected MRI signals for image reconstruction. To produce these MRI signals, radiofrequency (RF) magnetic fields are applied at resonance with nuclear spins to perturb M from equilibrium and tilt magnetization into the transverse plane (i.e., x-y plane), a process known as RF body excitation. When the RF fields are removed, a process known as relaxation begins, and the RF energy, which is the MRI signal, induces current flow on a receiving coil tuned to the resonance frequency of the nuclei of interest. This data, which is spatially encoded because of the gradient fields, is collected by an RF receive coil and processed by a console to reconstruct an image.

MRI systems are complex and consist of multiple hardware components. Fig. 1-4 shows a typical MRI room organization and a cross-sectional view of a scanner. The room is commonly divided into three sections, the console room, where the main computer that controls the MRI scanner and imaging processing occurs, the equipment room that stores all the major hardware components, such as the power amplifiers and receiver sub-systems and the magnet room, a shielded room where the main magnet, coils, and patient table are located. As labeled in Fig. 1-4, the magnet aligns the nuclear spins to this magnetic field. The gradient amplifier and coils are used for the spatial localization of image data. The RF amplifier and coil deliver the time-varying fields to perturb the entire system from equilibrium, producing the MRI signal that is received and processed for image reconstruction by the console. Table 1-I shows the technical specifications for a standard 1.5 T MRI system [15].

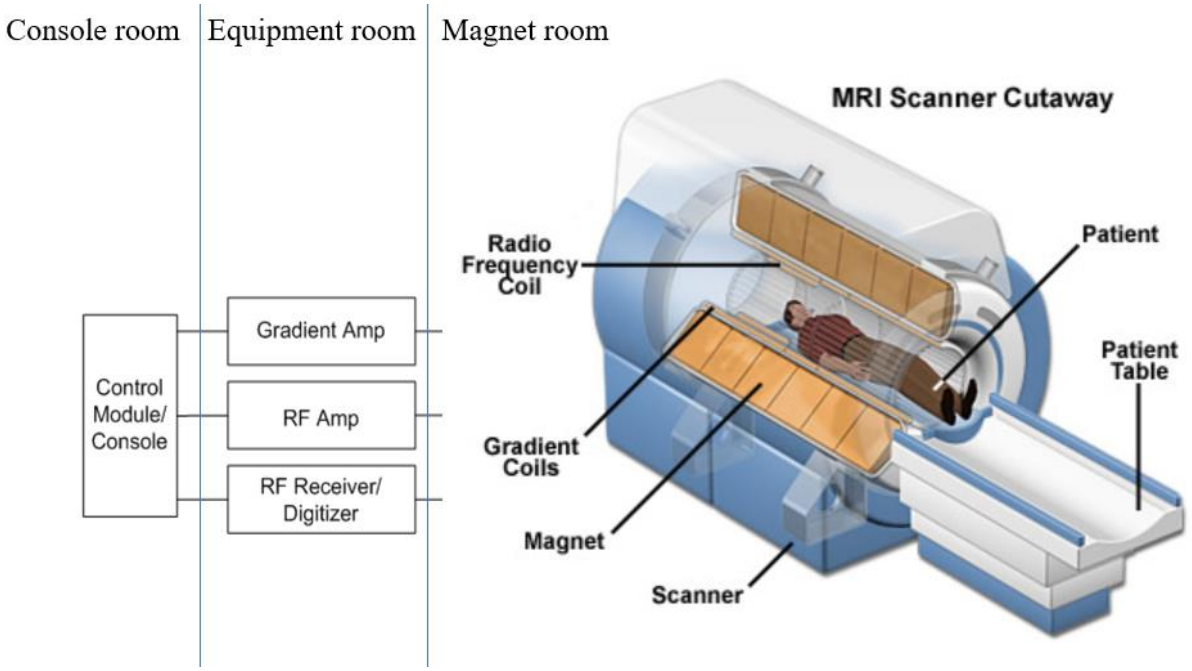

Fig. 1-4: Typical MRI room organization, the key hardware components, and cross-sectional view of an MRI system. Amp = amplifier; RF = radiofrequency. (Photo from: https://nationalmaglab.org/education/magnet-academy/learn-the-basics/stories/mri-a-guided-tour)

Table 1-I: Typical Specifications of an MRI System at 1.5 T [15]

Frequency (hydrogen)	64 MHz
Bore diameter	60 – 70 cm
Gradient amplifier	30 – 45 mT/m
RF power amplifier	~20 kW

1.3 MRI Safety and DBS Implant Heating

There are several safety concerns for patients to consider when entering an MRI area. It is common for imaging clinics to have patient screening protocols in place prior to imaging to inform patients of the general MRI safety guidelines when entering these restricted areas. The major MRI safety concerns arise from the electromagnetic fields used to generate an image, which are the main static magnetic field, the gradient magnetic field, and the RF magnetic field. The typical strength of these fields is listed in Table 1-I for a main magnet field MRI system at 1.5 T.

The main static magnetic field strongly interacts with ferromagnetic objects and can cause them to accelerate at very high speeds toward the centre of the magnet. Standard protocols have the equipment and objects clearly labeled for MRI compatibility, and areas outside the magnet room are tested and clearly marked according to magnetic field strength measurements to inform personnel of and prevent ferromagnetic objects from entering these restricted zones. In the case of DBS patients, implanted devices can shift, causing device malfunction or tissue damage [16]. Therefore, implant device manufacturers are required to meet specific design specifications to be granted MRI-compatible labeling [17].

The gradient magnetic fields can induce currents in conductive materials according to Faraday's law of induction, causing unwanted biological effects such as peripheral nerve stimulation. Similarly, for DBS patients, in addition to the biological effects, device malfunctions may also occur and cause bodily harm [18].

The primary safety concern associated with the RF magnetic field is the result of core body temperature elevations caused by resistive heating effects. RF power deposition in MRI is evaluated by the specific absorption rate (SAR), which is given by [19],

$$SAR_{\Delta v}(t) = \int \frac{\sigma(r)|E(r,t)|^2}{\rho(r)} dv, \tag{1-2}$$

where r is the position, σ is the conductivity of tissue, ρ is the mass density, $E(r,t)$ is the total E-field vector at position r as a function of time, dv is the differential volume element, and Δv is the volume over which the integral is calculated. There are two main SAR levels to consider in MRI, the global SAR, which is the whole-body average, and the local SAR, which can be the average value calculated for a 1- or 10-gram volume.

Due to RF safety risks, regulatory bodies place strict limits on SAR and body temperature increases. The limit for temperature elevation for a local temperature rise is +1.0 °C, and for the core body rise is +0.5 °C [20]. The peak SAR levels for the US Federal Drug and Food Agency (FDA) and International Electrotechnical Commission (IEC) are listed in Table 1-II [20]. A recent 10-year (2008 – 2017) study conducted by the FDA reported that of the adverse events reviewed, 59% of respondents had some thermal-related injury such as skin reddening, blisters, burns, warming, heating sensations, fire, and smoke [21]. These thermal-related injuries are serious and

are a major concern for patients in general. However, DBS patients also face the substantial risk of localized heating along the long conductive lead(s) implanted in critical functional regions of the human brain. The implanted DBS device can alter the local SAR spatial distribution in patients and, as a result, increase the risk of localized heating or bodily harm in DBS patients during RF body excitation. Severe patient incidents such as comatose or severe to permanent neurological damage have been reported in the literature [6, 22]. As a result, implantable medical devices including DBS devices, undergo rigorous safety testing prior to be granted MR-conditional labeling and often result in cautious imaging and the use of lower RF power protocols [18, 23].

Table 1-II Peak SAR MRI Safety Limits

	Whole-body SAR (W/kg)	Whole-head SAR (W/kg)	Head/torso 1g SAR (W/kg)	Extremities 1g SAR (W/kg)
FDA	4.0	3.0	8.0	12.0
IEC	2.0	3.2	10.0	20.0

DBS implant heating is a well-known safety issue and has been studied extensively in the literature [24-26]. In general, the tangential component of the electric field induces current flow along the DBS device, causing charge accumulation at the end of the lead that dissipates into the surrounding regions resulting in localized body heating that can potentially damage human tissue. Researchers have presented several simplified models to explain the mechanism of effect. Nitz *et al*. modeled the DBS lead as a resistance, inductance, and capacitance circuit with a conductance per unit length [27]. Konings *et al*. modeled the DBS lead as a waveguide with electromagnetic characteristics like that of a dipole antenna [28]. Yeung *et al*. assumed the DBS lead as a thin wire and a perfect conducting antenna. They demonstrated implant heating characteristics under two conditions: a uniform electric field with constant magnitude and phase and a uniform electric field generated by specific phases producing constructive interference at the tip of the lead [29]. Yeung *et al*. found that under the uniform field with constant magnitude and phase scenario, similar results reported by Konings *et al*. and Nitz *et al*. were demonstrated. However, under the second tested scenario with varying phases, differing and higher heating patterns were observed, demonstrating

that the mechanism of effect is more complex and that the simplified models may not be entirely conclusive.

Numerous simulation studies and MRI experiments using phantoms, an artificial test structure commonly filled with a single tissue-mimicking solution, have been published in the literature to predict temperature elevations under various imaging scenarios. Imaging studies recording temperatures at the tips of DBS leads or lead substitutes such as copper wire have reported a wide range of temperature results from +1 °C up to +46 °C and SAR levels [6, 18, 24-26, 30-31]. As a result, phantoms play an important role in safety verification experiments. Furthermore, the electromagnetic interactions between phantom dimensions, designs, DBS devices, and tissue-mimicking solutions can vary across assembled phantoms. Recent DBS studies suggest that using more sophisticated human models and phantoms may prove beneficial over conventional methods for predicting DBS patient safety outcomes [30].

Several different methods presented in the literature have the potential to address this patient safety issue. For example, Kazemivalipour *et al*. suggested utilizing the inherent low electromagnetic field band of the MRI system and a reconfigurable RF birdcage (i.e., circularly polarized) coil capable of re-orienting the low field band to a location that intersects the DBS lead and thus, reduces the RF heating effects along the DBS device [32]. Das *et al*. proposed a new lead design that offered greater RF coupling protection [33]. Golestanirad *et al*. studied the electromagnetic interactions and the application of field cancellation for strategic lead trajectories to reduce RF heating effects [34]. Another promising technique known as Parallel RF Transmission (or pTx) has also shown great promise at addressing DBS safety concerns and other clinical challenges, particularly at UHF strengths [35-36]. This thesis continued the development of a novel pTx safe mode technique proposed by McElcheran *et al*. [35] for DBS MRI safety and its implementation onto a novel pTx MRI platform proposed by Yang *et al*. [37]. The pTx safe mode method and system development will be described in detail in the proceeding sections.

1.4 Parallel RF Transmission

Parallel RF transmission (pTx) is garnering lots of research interest, particularly in resolving MRI challenges at UHF strengths (i.e., 7 T and above) [36, 38]. In addition, it has also shown

promise in resolving DBS safety issues at present clinical field strengths [35]. The full potential of pTx remains unclear and will continue to be an active research topic in the future.

The concept of pTx and optimized RF pulse design for MRI applications was first introduced by Katscher *et al*. for accelerated imaging. It involved using multiple RF transmit coils, each with independent time-dependent waveforms and spatial sensitivity, to under-sample the imaging space for speed enhancement and apply the superposition principle for data reconstruction and image formation [39]. In MRI, this is achieved during "body excitation", where RF pulses are used to perturb the human body from net magnetization alignment with the main static field (or B_0). This interaction can be explained mathematically by the net magnetization change into the transverse plane that occurs for a single, homogeneous transmit coil and can be calculated using the small tip-angle approximation defined as,

$$M(x)=i\gamma M_0(x) \int_0^T B_1(t) e^{ix\cdot k(t)} dt, \tag{1-3}$$

where $B_1(t)$ is the temporal sensitivity profile of the RF coil's magnetic transmit field for the duration of T, and $k(t)$ represents the k-space trajectory. When considering pTx, where multiple transmit coils are used with spatially varying B_1 profiles, a resultant transmit field pattern M_{res} can be expressed as a linear, sensitivity-weighted combination of virtual single-element patterns M_n:

$$M_{res}(x) = \sum_n S_n(x)\, M_n(x) \tag{1-4}$$

with

$$M_n(x)=i\gamma M_0(x) \int_0^T B_{1,n}(t) e^{ix\cdot k(t)} dt, \tag{1-5}$$

where S_n is the sensitivity of the n-th channel of the applied RF waveform $B_{1,n}$ and $k(t)$ is the (reduced) k-space trajectory [40]. There are several methods in determining $B_{1,n}$ to generate a desired M_n [39, 41]. Similar expressions can be derived for the electric field portion of the electromagnetic field through Maxwell's relationships [42]. As a result, with the appropriate inputs, tailored magnetic or electric field patterns can be produced. Because MRI coil interactions with the human body operate in the electromagnetic near-field of the coil (or antenna), reactive near-field effects are present, generating conditions where the electric or magnetic field component is dominant in a spatial location. In contrast, the opposite may be true a short distance away [43].

This characteristic behaviour with pTx technology is exploited to generate a safe mode of imaging capable of addressing the safety concerns for DBS patients used in this thesis.

There are two main pTx modes that enable the development of custom RF excitations: the RF shimming mode and the full pTx mode. The RF shimming mode relies on the replication of a single signal source across the different channels, each varying in amplitude and/or phase to produce the desired net electromagnetic condition, and in full pTx mode, completely arbitrary RF waveforms are delivered to each pTx channel. Fig. 1-5 and fig. 1-6 illustrate the basic concept of RF shimming and full pTx, respectively.

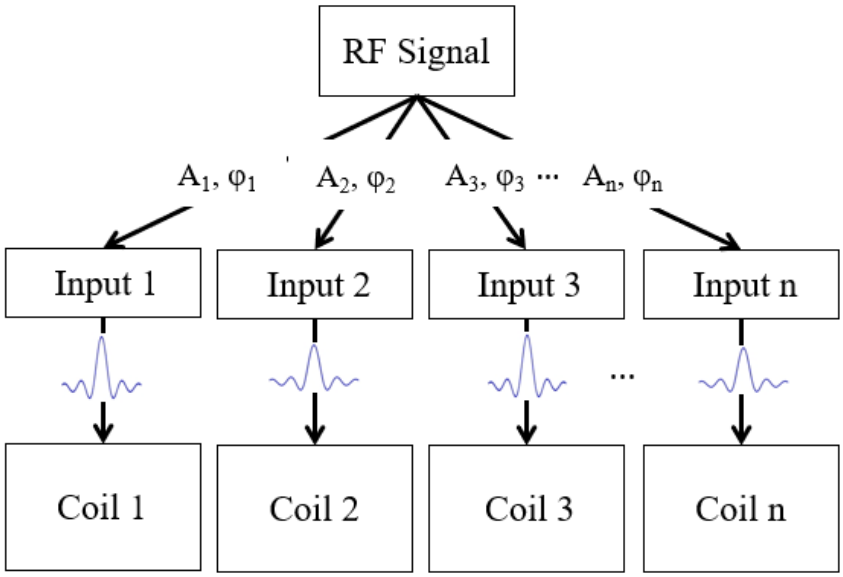

Fig. 1-5: Basic concept of pTx RF shimming mode.

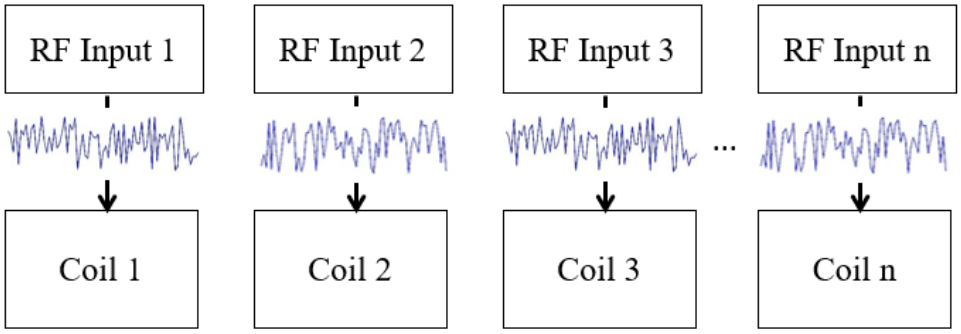

Fig. 1-6: Basic concept of full pTx mode.

1.5 RF Heating Minimization and Optimization

In MRI, patient safety is measured by the level of RF power deposited into the human body and is evaluated by SAR. According to equation (1-2), it is directly related to the square of the electric field for a time and position in space. More specifically, for DBS implants, the tangential component of the electric field with respect to the device and lead position is the dominant factor responsible for DBS implant heating effects. Thus, theoretically, minimization of the electric field (or its tangential component) will reduce the overall SAR and, in turn, the risks of DBS implant heating. Because the electric field is dependent on a position in space, minimization can be centralized to a specific region in space. It is well-known that the accumulation of charge build-up in a long conductive DBS lead occurs at the tip of the lead. Therefore, electric field minimization at the lead tip and/or its surrounding region should result in a significant reduction in DBS implant heating effects and minimize the risk of tissue heating.

As described in the previous section, RF shimming is a form of pTx that replicates a single source waveform across all system channels, each possibly varying in amplitude and/or phase. Mathematically, the total electric and magnetic field for an MRI coil with n-channels and a common input waveform can be written as [44],

$$E_{tot}(r,t) = \sum_N V_n(t) e_n(r) \tag{1-6}$$

and

$$B^+_{1,tot}(r) = \sum_N V_n(t) b^+_{1,n}(r) \tag{1-7}$$

where $V_n(t) = A_n e^{i\phi_n} V(t)$ and is the n^{th} coil input, $e_n(r)$ is the n^{th} coil electric field map produced for a particular coil sensitivity profile and $b_1{}^+{}_n(r)$ is the n^{th} coil magnetic field map produced for a particular coil sensitivity profile, respectively. Electromagnetic simulation can be used to obtain these field maps for a defined coil and imaging volume for a specific input signal; thus, determining the appropriate amplitudes and phases becomes a mathematical optimization problem.

There are several mathematical approaches to solving this optimization problem. This thesis focuses on one of many pTx optimization approaches and is proposed by McElcheran *et al*. that

utilized the RF shimming mode to create a safe mode of imaging [35]. The cost function used to determine the safe mode pTx parameters is defined as,

$$min\left((|E(r)|)_{ROM} + \lambda \frac{max_r(|B_1(r)|)-|B_1(r)|}{max_r(|B_1(r)|)}\right), \tag{1-8}$$

where $|E(r)|$ is the magnitude of the electric field at position r, $|B_1(r)|$ is the magnitude of the RF magnetic field at position r, r is the position, and λ is a weighting factor that prioritizes the importance of electric field minimization or B_1 homogeneity. For example, a weighting factor of 1 is the balanced condition between electric field minimization and optimal magnetic field homogeneity. The optimization is defined for a region of minimization (ROM) over an imaging plane or volume. Preliminary results utilizing the equation (1-8) demonstrated that for a specific 2-, 4- and 8-channel pTx coil design and a homogeneous cylindrical model with a straight copper wire insert, the RF shimming pTx inputs can be determined that minimizes the electric field in a ROM encompassing the wire tip with acceptable B_1 homogeneity over a plane of interest when compared to a conventional MRI birdcage coil [35].

The initial work demonstrated the potential of pTx to suppress localized RF heating effects in proof-of-concept. However, it did not consider a realistic DBS patient scenario where bilateral leads are implanted loosely, producing uniquely curved lead trajectories, or the case where multiple ROMs may be required [34]. Furthermore, the initial study estimated the tangential component of the electric field as approximately the magnitude of the electric field. This was a reasonable approximation for a straight wire as the net electric field and the tangential component are in parallel, but for actual DBS trajectories, this estimation does not hold. Thus, the cost function in equation (1-8) was modified for the added complexity to account for the vector components and potential of multiple ROM requirements [31]. Initial conditions were then included in the cost function; in addition, SAR and B_1 pre-conditions to improve simulation efficiency and constrain the solution space [31, 44]. The new modified cost function is expressed by,

$$min_{A_n,\varphi_n}\left[\left(\frac{\sigma_{VOI}(|B_{1,tot}^+|)}{\mu_{VOI}(|B_{1,tot}^+|)}\right) + \lambda \cdot \mu_{ROM}\left(\frac{(|E_{tot}|^2)}{(|E_{quad}|^2)}\right)\right], \tag{1-9}$$

where $\sigma_{VOI}()$ is the standard deviation of the total B_1^+-field over the VOI; $\mu_{VOI}()$ is the mean of the total B_1^+-field over the VOI; $\mu_{ROM}()$ is the ratio of the means of the total electric field and E_{quad}

over the ROM; $B_1^+{}_{tot}$ is the net excitation magnetic field produced by all coil elements; λ is a weighting factor; and E_{quad} is the electric field in the pTx quadrature mode (A_n = 1, φ_n = ((π(n-1))/2)), a circularly-polarized field and the optimized initial condition. The modified cost function was demonstrated to successfully suppress RF heating effects at several ROM in a multi-layer human head model with bilateral copper wire inserts [31]. The cost function presented in equation (1-9) is utilized to derive the different pTx inputs that produced the DBS MRI safe mode scenarios studied in this thesis.

1.6 Electromagnetic Simulation and Temperature Modelling

Electric and magnetic field maps, as mentioned, play an integral role in determining the pTx parameters required for MRI safe mode generation. Electromagnetic simulation solvers are ideal for studying DBS implant heating effects and provide the electric and magnetic field vector maps at every position based on Maxwell's equations for any discretized model. Built-in tools such as the optimization feature can provide an interface to implement custom cost functions with constraints to calculate the optimal pTx inputs necessary to minimize localized RF heating effects while maximizing B_1 homogeneity for a specific MRI coil design and imaging object. There are three main solver methods implemented in commercial simulation tools, the finite difference time domain method, the finite element method, and the method of moments (MoM). FEKO (Altair Engineering, MI, USA), a frequency-based MoM solver was used for all the electromagnetic simulation studies conducted in this thesis.

The basic concept of MoM is to minimize the residual between an unknown response function and an approximation of the response function [45]. Consider a linear operator formula,

$$L[f(x)]=g(x), \tag{1-10}$$

where L is a linear operator, $f(x)$ is the unknown response function, and $g(x)$ is a known function. $f(x)$ can then be represented by a series of basis functions as,

$$f(x) \approx f_\alpha(x) = \sum_{n=1}^{N} \alpha_n h_n(x), \tag{1-11}$$

where α_n is a set of unknown expansion coefficients and $h_n(x)$ is a series of known expansion functions. Then substituting equation (1-11) back into equation (1-10) yields,

$$L[f(x)] = \sum_{n=1}^{N} \alpha_n L[h_n(x)] \approx g(x), \tag{1-12}$$

A residual function then can be defined as,

$$r(x) = L[f(x)] - L[f_\alpha(x)] = g(x) - L[f_\alpha(x)]. \tag{1-13}$$

Theoretically, the goal of MoM is to minimize the residual function to zero, which would result in the approximate function equaling the response function. To minimize the residual function, MoM forces the 'weighted' residual to zero by first defining a set of suitable weighting functions (w_1, w_2, ... w_N) and then performing the inner product in (1-13) with each w_m (for m = 1, 2, 3, …, N) yielding,

$$\sum_{n=1}^{N} \alpha_n \langle w_m(x), L[h_n(x)] \rangle \approx \langle w_m(x), g(x) \rangle \tag{1-14}$$

and by converting (1-14) into matrix form yields,

$$\begin{bmatrix} Z_{11} & Z_{12} & \dots & Z_{1N} \\ Z_{21} & Z_{22} & \dots & Z_{2N} \\ \vdots & \vdots & \dots & \vdots \\ Z_{N1} & Z_{N2} & \dots & Z_{NN} \end{bmatrix} \begin{bmatrix} \alpha_1 \\ \alpha_2 \\ \vdots \\ \alpha_N \end{bmatrix} = \begin{bmatrix} w_1(x), g(x) \\ w_2(x), g(x) \\ \vdots \\ w_N(x), g(x) \end{bmatrix}, \tag{1-15}$$

where $Z_{mn} = \langle w_m(x), L[h_n(x)] \rangle$. Using an iterative method, the expansion coefficients of the basis functions can be obtained by matrix inversion. The choice of weighting functions will affect the accuracy and convergence of the solution space.

In this work, FEKO was used to provide the required electric and magnetic field maps for a defined RF coil design and phantom model (i.e., simple patient). These electromagnetic field maps were then inputted into a custom-scripted heuristic local search optimization method to solve the cost function presented in the equation (1-9) to determine the RF shim parameters (i.e., the amplitudes and phases) for safe mode generation. In general, a heuristic search optimization begins by solving a cost function under two conditions, a defined initial condition and a defined incremental step from this initial condition. These two solutions are then compared, and a decision is made based on whether the step direction within the solution space better satisfies the convergence criteria. If so, the latter condition becomes the new reference or comparator for the next step. Otherwise, the former condition remains the reference, and the process continues for the

next incremental step. This iterative process continues until the incremental steps do not result in further improvements that satisfy a preset convergence criterion. At this point in the optimization, an optimum solution has been reached. In general, a local search bounds the search space to solutions nearby a defined initial condition. This approach offers faster convergence but calculates the local optima within the optimization boundaries, which may not result in finding the global optimum, the optimal solution in the entire solution space. Regarding pTx MRI and RF shimming, it was found that several amplitude/phase channel combinations can substantially reduce RF heating effects; as a result, a local search implementation for this application was suitable [31, 35].

SAR is the primary RF safety measure used in MRI; however, assessing local SAR for implanted DBS devices in experiments can be challenging, and translating SAR into an absolute temperature is more useful and practical. A widely accepted model used to estimate biological heat transfer in the human body is known as Penne's bioheat transfer equation [46], a differential equation that simulates the spatial and temporal changes in temperature and can be expressed as,

$$\rho c \frac{\partial T}{\partial t} - \nabla \cdot k \nabla T - Q_{met} + \rho_b c_b w (T - T_b) = (SAR)\rho, \tag{1-16}$$

where T is the temperature rise, c is the specific heat capacity, k is the thermal conductivity, Q_{met} is metabolic heating, ρ_b is the mass density of blood, c_b is the specific heat capacity of the blood, w is the perfusion of blood, T_b is the blood temperature, SAR is the local specific absorption rate, and all parameters are assumed to depend on position. In this work, a custom script available in FEKO (i.e., the thermal analysis macro) that implemented a finite difference approximation method to estimate the temperature change at the tip of the lead was used. The finite difference approximates differential equations by approximating derivatives with finite differences that approximate them [47]. To estimate the temperature change in (1-16), a time step is set with an initial condition that progressively iterates on the previous temperature value for a specific duration. The temperature change predicted in the simulation can then be validated in experiments with a temperature sensor(s) attached to the lead tip(s).

1.7 Research Contribution

The research work presented in this thesis has resulted in several publications and contributed to the knowledge of DBS MRI safety in two major topics, pTx MRI technology

development and phantom fabrication design. The following is a list of my specific academic achievements:

1. I reviewed a promising pTx MRI safe mode technique with the potential to minimize the effects of implant heating in DBS patients and its implementation onto a novel pTx MRI research platform. I studied and evaluated the impact of system uncertainty in a simulation study according to the technical specifications of the presented pTx MRI platform for a 4 and 8-channel safe mode pTx MRI system configuration. A worst-case system error analysis that predicted the temperature elevation at the lead tip was also simulated for both pTx setups. This work was published in *Medical Physics* in July 2023, and was authored in order by Benson Yang, my academic supervisor Chih-Hung Chen from McMaster University, and my reporting supervisor Simon J. Graham from Sunnybrook Research Institute.
2. I expanded on the previous simulation study and further investigated the impact of system channel count on DBS implant heating minimization and its associated safe mode of imaging. I evaluated a third pTx system configuration and, based on the simulation results, proposed an optimal system configuration that was economically feasible and also effective at reducing DBS implant heating effects. The proposed 8-channel RF coil was constructed, tuned, and matched for future pTx MRI experiments.
3. I studied in simulation and experiment the effects of patient motion on safe mode pTx MRI in proof-of-concept to assess the clinical applicability and robustness of the applied pTx safe mode technique. The study included typical DBS patient head movements and rotations with temperature measurements during 4-channel safe mode pTx MRI. This work was published in *IEEE Letters on Electromagnetic Compatibility Practice and Applications* in June 2022 and was authored in order by Benson Yang, Chih-Hung Chen, and Simon J. Graham.
4. I reviewed the current MRI safety standards and assessed their suitability for DBS applications. I conducted preliminary experiments that demonstrated the benefits of using advanced heterogeneous phantoms in DBS safety studies. I designed, fabricated, and tested a new anthropomorphic heterogeneous phantom for advanced DBS safety investigations. This work was published in *Medical Physics* in August 2020 and was authored in order by Benson Yang, Fred Tam, Benjamin Davidson, Pei-Shan Wei,

Clement Hamani, Nir Lipsman, Chih-Hung Chen, and Simon J Graham. Fred assisted with the fine features of the CAD model, Pei-Shan assisted with the preparations of the gel solutions that filled the phantom, and Benjamin, a resident neurosurgeon from the University of Toronto, and his supervisors, Clement and Nir from Sunnybrook Health Science Centre assisted with the DBS implantation. All authors reviewed and edited the manuscript.

1.8 Thesis Organization

This thesis is divided into six chapters. Chapter 1 briefly introduces DBS and MRI physics and discusses the MRI safety risks associated with imaging DBS patients, primarily the risk of RF power coupling onto the implanted device, causing localized hot spots capable of damaging adjacent tissue. It also introduces the concept of an emerging technology known as parallel RF transmission (or pTx) and the basic theory of a novel pTx MRI method that enables a safe mode of imaging that may potentially address this DBS safety concern. The chapter concludes with the research contributions and organization of this thesis.

Based on the theory of pTx MRI described in Chapter 1, Chapter 2 utilizes my previously developed pTx MRI research platform that enables experimental studies. It presents the hardware complexities of the pTx MRI platform and the importance of studying the practical limitations of hardware devices. It also discusses the hardware impact on the generation of the presented pTx MRI safe mode and the safety implications it may have on DBS patient imaging. It evaluates the DBS implant heating effects for system uncertainty based on the technical specifications of the presented pTx MRI research platform. In addition, it presents the study of a worst-case imaging scenario and the effect of system channel failure.

After understanding the limitation and uncertainties of the hardware, Chapter 3 investigates the effect of system channel counts on DBS implant safety for an 8- and 16-channel pTx configuration. Due to the very high cost of enabling pTx technology on MRI systems, it is crucial to determine the optimal system configuration capable of effectively minimizing the MRI safety risks and the concerns associated with system uncertainty while maintaining economic feasibility and system design simplicity. The chapter concludes with the design, fabrication, and characterization of a prototype 8-channel head coil for pTx MRI experiments.

After we obtained an optimum system configuration, Chapter 4 turns our attention to the implications of patient motion on image reconstruction in MRI. Since safe mode pTx MRI is derived for a subject from a fixed position in space, consequently, any displacement from this reference position will alter the electromagnetic distribution and may alter the system parameters required for safe mode. More importantly, it may result in the generation of an unsafe imaging condition, particularly for DBS patients that suffer from motor-related symptoms. Therefore, it is crucial to study patient motion effects. Chapter 4 investigates the DBS implant heating in proof-of-concept in 4-channel pTx MRI safe mode for typical DBS patient head movements and rotations. Simulation and experiment are conducted to assess the robustness of the presented pTx safe mode technique.

To better replicate the actual lead trajectories of DBS patients, Chapter 5 presents the design and development of an anthropomorphic phantom. It starts with a simple experiment using a conventional method to evaluate and compare the DBS implant heating effects. It also compares the use of copper wire as a DBS lead substitute in two lead geometries. These simple experiments served as an initial step in assessing the need for improved phantom structures in DBS safety studies and demonstrated the advantage of using real DBS devices. It is then followed by a detailed description of the design and development of a novel anthropomorphic heterogeneous phantom with MRI experiments to evaluate its utility. The preliminary results suggest that advanced phantoms with improved realism are advisable for DBS MRI safety experiments.

Finally, Chapter 6 concludes this thesis and discusses future study topics relevant to the main results presented in each chapter. It is then followed by general recommendations relevant to the presented pTx MRI safe mode technique and DBS patient safety.

Chapter 2

Parallel RF Transmission (pTx): System Uncertainty

This chapter describes a novel parallel RF transmission integration onto an existing MRI system used to study several DBS pTx MRI topics presented in this thesis [48]. The major hardware components and preliminary experimental results demonstrating the utility and effectiveness of the proposed pTx safe mode technique are presented and reviewed. This is followed by a preliminary pTx system characterization and system uncertainty study using electromagnetic simulations. An initial channel-to-channel variation study was conducted to quantify possible system channel variations due to instrumentation imperfections. The results of this study demonstrated pTx system limitations, which motivated subsequent studies on system uncertainty. Furthermore, it provided a sample data set demonstrating the appropriate system channel corrections necessary to improve experimental accuracy for a specific MRI pulse sequence configuration and helped identify necessary future system improvements. This led to a simulation study investigating the impact of hardware uncertainties during 4-channel safe mode pTx MRI. The chapter concludes with a discussion of the results. The work contained in this chapter has been published in or was presented in a part of at,

- B. Yang, C.-H. Chen, and S. Graham, "Technical Note: System Uncertainty on Four- and Eight-Channel Parallel RF Transmission for Safe MRI of Deep Brain Stimulation," *Med. Phys.* 50(9):3745-3751, 2023.
- B. Yang, C.-H. Chen, and S. J. Graham, "Safety of 4-channel parallel radiofrequency transmission MRI at 3 T: Effects of system uncertainty and system failure pertinent to deep brain stimulation," *Proc. 30th scientific meeting, Intl. Soc. Mag. Reson. Med.*, London UK, 2022, p. 2813.
- B. Yang, C.-H. Chen, and S. J. Graham, "Signal-to-noise measurement of a 4-channel parallel radiofrequency transmission system for MRI at 3 T", *Proc. 28th scientific meeting, Intl. Soc. Mag. Reson. Med.*, Virtual, 2020, p. 4035.

2.1 pTx MRI Research Platform Review

Currently, the commercial options for pTx MRI systems are limited, expensive, and primarily for research purposes. Once built and installed, MRI system hardware components are difficult to substitute or modify for specific clinical applications. Thus, investigators have relied on in-house pTx system development, typically assembled as add-on systems that integrate onto existing commercial MRI systems. The basic concept is utilizing the commercial system's main magnet, gradients and software and replacing the RF pathway with the add-on pTx system while bypassing system safety procedures that would prevent the MRI system from operating in "pTx mode". There are several methods to achieve pTx MRI capabilities, and implementation typically depends on the manufacturer and model of the scanner. One of the possible integration procedures is described here.

Yang *et al.* designed and integrated an expandable 4-channel pTx MRI platform used in this thesis [48]. The system overview and basic concept are shown in Fig. 2-1. Fig. 2-1 (a) outlines the basic RF signal flow of the add-on pTx system and (b) displays photographs of the hardware components used, which is a combination of commercial and custom-designed devices. To integrate the add-on 4-channel pTx system onto a 3 T Siemens MRI system (Magnetom Prisma, Siemens Healthineers, Erlangen, DEU), a custom 4-channel adaptor module was designed and assembled in collaboration with a preferred Siemens vendor (Stark Contrast, Erlangen, DEU), equipped with a Tim4G plug, a Siemens proprietary connector that connects the MRI system via the patient table. This provided the necessary access to the MRI system's existing transmit and receive pathways. With the connection of a pTx MRI coil, RF signals can then be transmitted from the pTx system and received by the MRI system for image reconstruction by the console. The RF transmit source signal used by the pTx system is replicated from the MRI system via the adaptor module and is connected to a 40 dB directional coupler (C11082-13, Werlatone, Patterson, NY, USA); the original RF signal is dissipated through a load, enabling regular system operation and system safety bypass and the attenuated signal is further attenuated to a desired power level (using HAT-10+, Mini-Circuits, Brooklyn, NY, USA) before being inputted into the RF modulator (CGP-128-4C, CPC, Hauppauge, NY, USA). The RF modulator splits the input into four independent signals with adjustable amplitude and phase via a web interface that each connects to a separate 60 dB RF power amplifier (BT01000-AlphaSA, Tomco Technologies, Stepney, AUS). The

modulated and amplified signals are then fed back into the adaptor module for RF signal delivery by the custom pTx MRI coil. To ensure proper signal timing between the add-on pTx system and the MRI system, the RF blank signal of the MRI system is duplicated across each RF power amplifier for signal triggering.

The two hardware components designed and fabricated internally were the 4-channel adaptor module and the 4-channel pTx MRI coil. The purpose of the adaptor module was to: (1) act as a transmit and receive switch, (2) provide the pTx small-signal RF source, a direct feed from the MRI system to the adaptor that enabled full utilization of the MRI system and library of imaging protocols and (3) the pTx RF pathway to the MRI system's receiver chain. Because present MRI systems can receive multiple signals for image reconstruction, integrating the add-on pTx system into the MRI system via the adaptor module equipped with the Tim4G plug was reasonably straightforward.

The primary function of the switch is to enable distinct and isolated transmission and receive signal pathways. The basic design principle is shown in Fig. 2-2. The p-type intrinsic n-type (or PIN) diode and the quarter-wavelength transmission line are the central components controlling the operation of the switch. For a specific operating frequency (i.e., the Lamor frequency of 123 MHz for hydrogen on the Siemens MRI system), the quarter-wavelength transmission line exhibits a unique electrical characteristic that can present a high and low impedance on opposite ends of the transmission line. It can be constructed by either lumped elements or looped coaxial cable cut at the appropriate length, based on the relationship, wavelength (or λ) = wave speed/frequency. Under the forward bias condition (or on), the diode has the characteristics of a "short-circuit" and a high impedance at the antenna terminal (due to the "direct" to ground connection on the opposite end of the quarter-wavelength transmission line). This isolates the receive pathway, and according to Fig. 2-2, this activates the transmit pathway and when in the reverse bias condition (or off), the diode has the characteristic of an "open-circuit", activating the receive pathway. Low noise amplifiers are commonly added to boost signal quality at the receiver end, thus, completing the design of a typical switch for MRI applications.

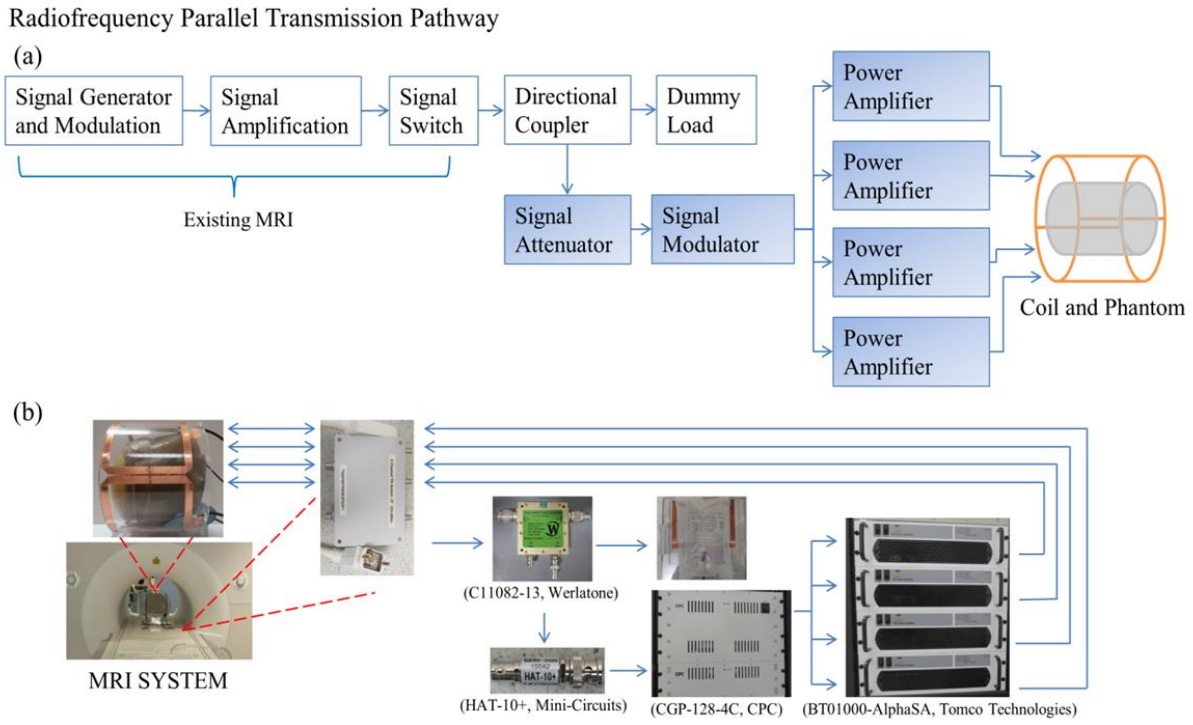

Fig. 2-1: (a) Block diagram showing the custom 4-channel pTx system RF transmission signal pathway. Shaded blocks represent hardware components in the equipment room, and unshaded blocks represent the equipment in the magnet room. (b) A graphic diagram of the corresponding hardware devices.

Specifically, the primary imaging volume of interest for DBS patients is the human brain. Therefore, the pTx MRI coil design for this work was required to meet this essential criterion and was constructed with dimensions to fit the average human head. It was also designed as a transmit and receive (or transceiver) coil. There are several types of coils, but for pTx MRI, a collection of basic-shaped (i.e., rectangular) phased-array elements, sized accordingly to be capable of imaging to the depths of the human head were hypothesized to be the most logical and simplistic option. The basic coil design principles will be discussed here and in the next section. A specific pTx MRI coil design, its fabrication and benchtop characterization will be discussed in Chapter 3.

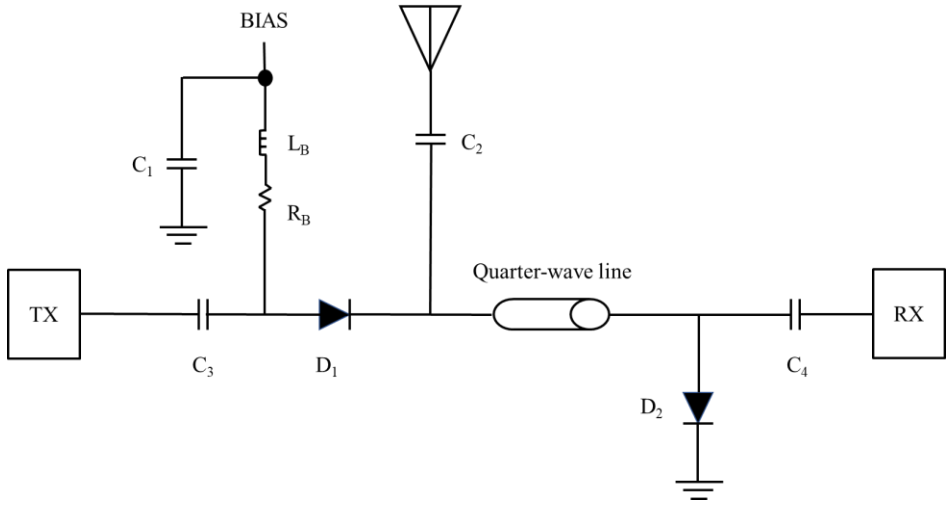

Fig. 2-2: A basic transmit and receive switch schematic for magnetic resonance imaging applications. TX = transmit; $C_1 = C_2 = C_3 = C_4$ = capacitors; L_B = bias inductor; R_B = bias resistor; $D_1 = D_2$ = p-type intrinsic n-type diodes.

The basic theory of an MRI coil revolves around the concept of resonance, and the operating frequency is governed by the imaging nuclei of interest (i.e., hydrogen in the standard scenario). A typical MRI coil comprises of lumped elements: inductors, capacitors and resistors. Theoretically, at resonance, the electrical characteristics of the coil are purely resistive, and the relation between the angular resonance frequency and the lumped elements can be given by [49],

$$\omega = \frac{1}{\sqrt{LC}} \tag{2-1}$$

where L is the total inductance, and C is the total capacitance. In general, coil performance can be characterized by its quality factor (or Q), which is given by [49],

$$Q = \frac{\text{maximum energy stored}}{\text{average energy dissipated per cycle}} = \frac{\omega L}{R} \tag{2-2}$$

Typically, for most phased-array type coils, the geometry of the array is the dominant source of inductance, and capacitors are distributed to tune the coil to the desired frequency and the greater the quality factor, the higher performing resonant circuit. The remaining hardware components are commercially available and will not be reviewed as part of this thesis.

Patient safety was another critical consideration in developing the pTx MRI system. To integrate the two systems, the safety procedures on the existing MRI system were bypassed, and

the RF power was dumped into a load. As a result, an independent safety monitoring system required development to ensure patient safety. The major considerations are developing and implementing a SAR estimation algorithm and a real-time monitoring system to ensure safe pTx operation. Currently, the design of a real-time monitoring system has been prioritized over implementing a SAR estimation method as research studies have been thus far limited to phantom structures.

Yang *et al*. designed a LabVIEW (National Instruments, Austin, TX, USA) based system that monitors the operational and fault statuses of the RF amplifier units. An automatic system shutdown is activated when a fault condition is detected, ending the imaging session until the faults are reset and cleared [50]. Fig. 2-3 displays the prototype of the front panel of the safety monitoring system for the 4-channel pTx system. The software program is implemented on a dedicated computer console and can be further expanded to monitor other hardware devices or intercept RF signals at desired locations.

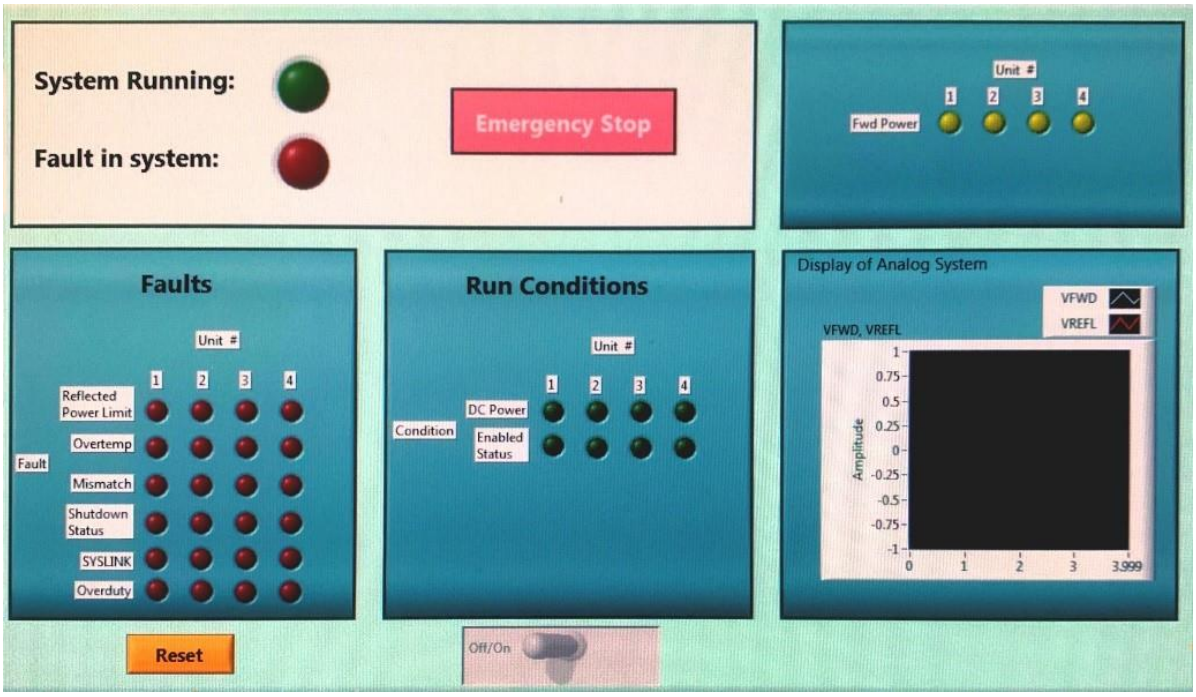

Fig. 2-3: A photo of the LabVIEW-based 4-channel pTx system safety monitoring front panel. Analog and digital lines on the radiofrequency power amplifiers are monitored in real-time, and normal and fault conditions are set with the appropriate colour indicator. An emergency stop button is also available for operator control [50].

2.1.1 Safe Mode 4-channel pTx MRI Setup

To evaluate the pTx MRI system and the associated pTx safe mode technique for DBS applications, presented in Chapter 1, RF heating phantom experiments were conducted. First, an electromagnetic head model and MRI coil design were constructed in FEKO (Altair Engineering Inc., Troy, MI, USA), as shown in Fig. 2-4 (a). The head model formed with an acrylic shell (conductivity of 0.00017 S/m, relative permittivity of 2.5 and loss tangent of 0.01) contained an insulated (conductivity of 0 and relative permittivity of 2.4) ideal copper wire with an exposed tip that mimicked a realistic DBS lead trajectory and was implanted into a homogeneous solution filling the shell with electromagnetic properties resembling human grey matter (conductivity of 0.69 S/m, relative permittivity of 67 and loss tangent of 1.5). A 4-channel phased array-based RF coil tuned and matched to 123.25 MHz (the resonant frequency of hydrogen on the Siemens MRI system) surrounded the head model. The length (axial direction) of each array was 15 centimeters with equal width fitting a 25-centimeter diameter circle around the head. Tune and match capacitors (determined by simulation) were spread around at the mid-point of each array element with two equally spaced capacitors used for coil-to-coil channel isolation and de-coupling. The complete meshed model contained 26260 mesh triangles and 56 mesh wire segments covering a total head volume of 5.2 $x10^{-3}$ m^3. These model parameters and elements were used for all electromagnetic simulations unless otherwise specified. MRI system predicted SAR levels was used to define the simulated electromagnetic solution space that normalized the simulation and experimental results. The specific SAR details are defined in each simulation study.

To validate the electromagnetic simulation results and optimize experiments, the head model was 3-D printed, and the RF coil was fabricated according to the above dimensions. Fig. 2-1 (b) and 2-5 display photographs of the constructed pTx MRI coil and head phantom, respectively. Benchtop scattering parameter measurements for the 4-channel coil recorded a minimum of -12 dB for the reflection coefficient (i.e., S_{11}) and a minimum of -14 dB for isolation between next neighboring channels (i.e., S_{12}). They overall represent less than 10 % power loss. As shown in Fig. 2-5, an insulated copper wire with an exposed tip on one end was implanted into the phantom structure in the best attempt to replicate the orientation of the lead model used in the simulation (which was derived from a real DBS patient computed-tomography image). Simulation parameters, such as capacitor values, were then updated to match the actual values used in coil

construction for consistency. An optimization procedure using FEKO (Altair Engineering Inc., Troy, MI, USA) and MATLAB (MathWorks Inc., Naticks, MA, USA) implemented the cost function presented in Chapter 1. It calculated the necessary amplitudes and phases for each system channel to generate the pTx safe-mode imaging. The safe mode parameters (uncalibrated) used throughout this thesis were: channel 1, 0 dB / 62º; channel 2, -4.0 dB / 347º; channel 3, 0 dB / 290º; and channel 4, -1.5 dB / 310º.

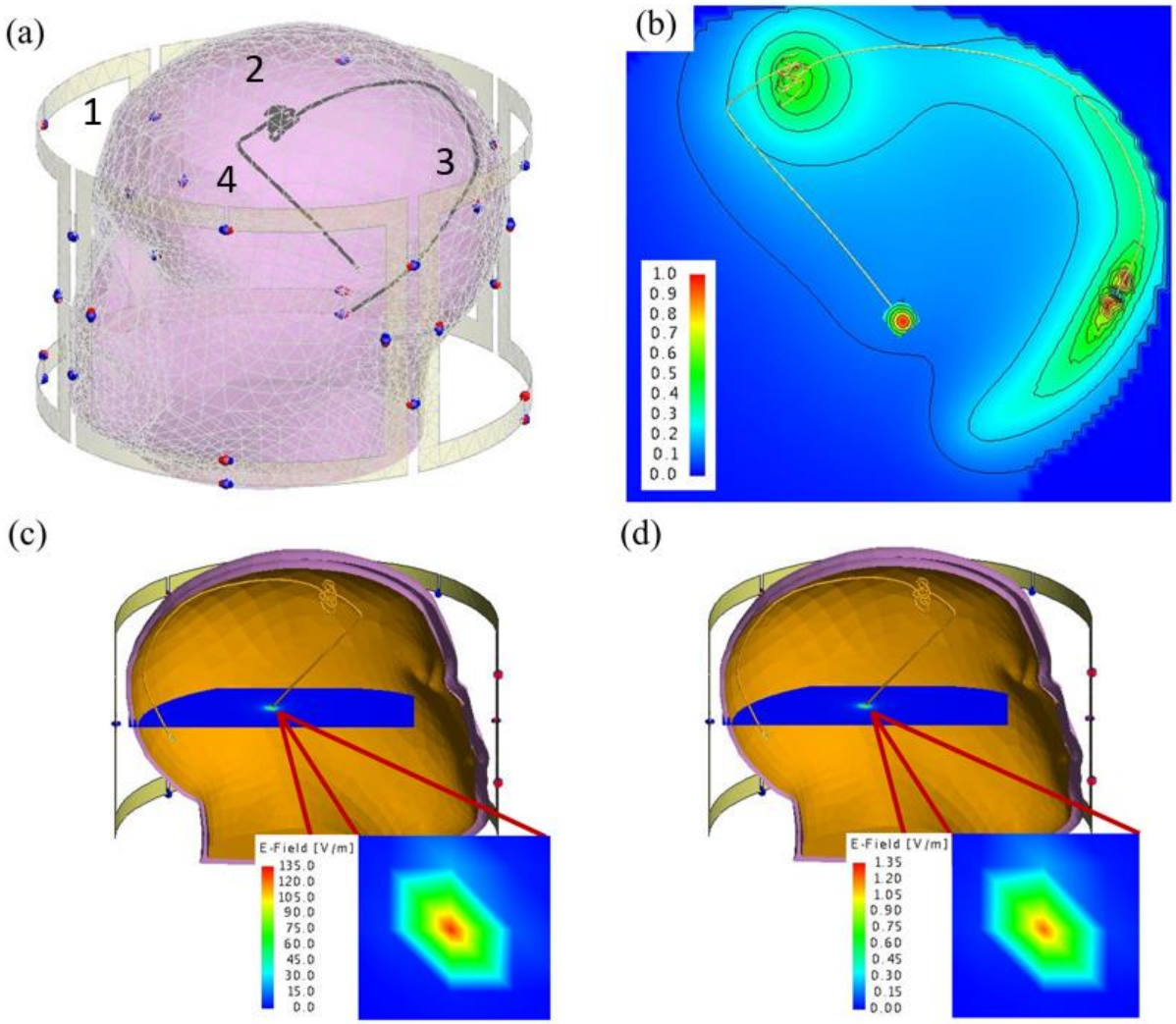

Fig. 2-4: (a) The 4-channel MRI coil design (as labeled) and homogeneous head model with implanted insulated copper wire used in electromagnetic simulation, (b) the normalized simulation results of the electric field strength along the implanted copper wire, (c) simulated electric field results at the tip of the wire in pTx MRI quadrature mode and (d) simulated electric field results at the tip of the wire for pTx MRI safe mode. A significant reduction in electric field strength at the wire tip can be observed for the safe mode scenario.

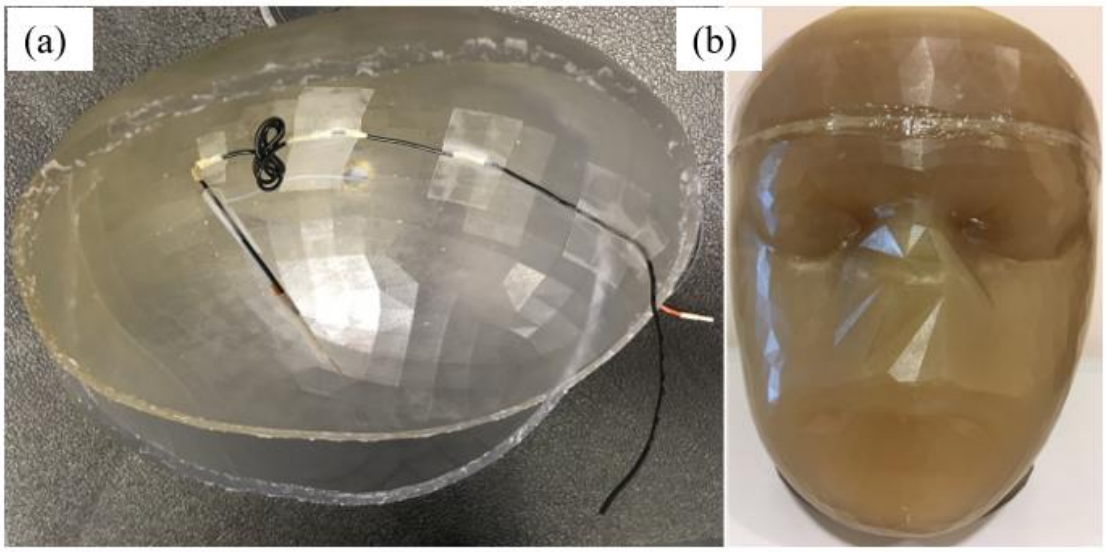

Fig. 2-5: A photograph of the constructed phantom, (a) displays the copper wire trajectory and attached fibre-optic temperature sensor used in the experiment and (b) the fully assembled and filled phantom [51].

2.1.2 Safe Mode 4-channel pTx MRI Results

The electromagnetic simulation results are shown in Fig. 2-4 (b) to (d). Fig. 2-4 (b) displays the normalized electric field contour plot for a region of interest encompassing the head model and insulated copper wire implant. As expected, the exposed wire tip had the highest concentration of electric field strength. The opposite end also displayed a significant electric field. However, in DBS patients, this end would be connected to the neurostimulator and, as a result, would experience a different level of charge accumulation known to be much less of a concern than the wire tip. Fig. 2-4 (c) and (d) display the simulation results for RF signal transmission under quadrature mode, whereby a constant amplitude with 90º phase shift between neighboring channels is applied and safe mode, whereby the simulation determined amplitude and phases are applied, respectively. A ten-fold difference can be observed between the two modes; thus, a significant reduction in localized SAR can be expected. Next, these simulation results were verified in imaging experiments.

The initial MRI experiments demonstrated that the 4-channel pTx MRI setup could be used for DBS safety applications [48]. Table 2-I shows the preliminary MRI RF heating experimental results in two pTx configurations: quadrature mode, representing a scenario of high RF heating and safe mode, representing a scenario of low RF heating. These temperature results were

compared to a conventional MRI setup for brain imaging, whereby a standard birdcage (i.e., for circular polarization) head coil is used. The temperature changes were recorded at the exposed tip of the implanted wire with an attached fibre-optic temperature sensor (OTG-MPK5, Opsens Inc., Quebec City, QC; ± 0.3 °C accuracy) for an MRI imaging protocol that was configured for significant RF heating and was based on a spin-echo pulse sequence (turbo spin-echo: acquisition matrix = 256 × 205, in-plane resolution = 0.5 mm × 0.5 mm, repetition time = 516 ms, echo time = 6.7 ms, refocusing flip angle = 150°, echo train length = 2, slice thickness = 2 mm, averages = 3, acquisition time = 3.45 minutes). This initially demonstrated the proposed add-on pTx system and the associated pTx safe mode technique. It also supported the preliminary electromagnetic simulation results.

Based on the experimental results, it can be observed that the pTx MRI system can produce a scenario of excessive RF heating at the wire tip and, when in safe mode, produce a scenario of minimized RF heating at the wire tip that is well-below DBS imaging guidelines described in Chapter 1. Furthermore, the safety risks were not limited to only pTx MRI configurations but also standard imaging with commercial head coils, such as the birdcage coil, which showed an absolute temperature change that exceeded the recommended safety threshold of +1.0 °C for MRI at 1.5 T, as presented in Chapter 1. However, human biological effects are not accounted for in phantom studies, which will dampen the level of RF heating experienced in DBS patients. In addition, the imaging parameters used in this experiment were primarily for proof-of-concept of the add-on pTx system and its associated safe mode technique and are not an accurate representation of a routine brain MRI protocol used in clinical settings. Nonetheless, the MRI experiments demonstrated the potential of pTx at addressing DBS patient safety and identified that exploration in clinical imaging routines would be beneficial and is, therefore, a topic of study in Chapter 4.

As observed from Fig. 2-1, integrating the 4-channel pTx system introduced several new hardware components, adding to the complexity of the existing MRI RF pathway. System characterization and optimization have become an important topic with pTx MRI operation bypassing existing MRI system safety procedures. This chapter builds on the preliminary results presented thus far and investigates the implications of system uncertainty on DBS imaging safety and the proposed pTx safe mode technique.

Table 2-I: A summary of the MRI RF heating experimental results [48].

	Initial temp. (°C)	Final temp. (°C)	Temp. change (°C)	Temp. uncertainty (°C)
pTx mode: quadrature	22.5	29.4	6.9	± 0.3
	21.6	26.7	5.1	± 0.3
pTx mode: suppression	22.9	22.9	0	± 0.3
	22.0	22.0	0	± 0.3
Siemens birdcage head coil	20.9	23.2	2.3	± 0.3
	20.7	23.4	2.7	± 0.3

2.2 pTx MRI System Characterization: Channel-to-channel Variation

Parallel radiofrequency transmission system (or pTx) implementations have grown steadily in the last decade [48, 52-53]. Currently, some commercial systems are available for research; however, in-house designs remain a relevant alternative not only from a cost perspective but also because optimal channel counts and pTx methods for different clinical applications are still under investigation. Often, in-house pTx systems are assembled with commercial and in-house designed components that can require additional measurements to determine certain system characteristics. Although most measurements can be performed "on the bench," it is advantageous to conduct measurements during imaging for better accuracy and insight into the actual system behaviour. Some MRI applications (i.e., reduced field-of-view imaging) are more sensitive to pTx system uncertainties. In particular, system calibration and optimization require many measurements to be conducted in real-time to maximize overall system performance and deliver accurate RF signals for generating the proposed pTx safe mode. This work uses a simple multi-purpose method to conduct real-time measurements of a 4-channel pTx system integrated onto an existing 3 T MRI system.

2.2.1 Experimental Method

To perform the various measurements on the 4-channel pTx system integrated onto an existing 3T MRI system (Magnetom Prisma, Siemens Healthineers, Erlangen, DEU), RF directional couplers (C5497-13 / C7008-102, Werlatone, Patterson, NY, USA) were inserted into

the RF transmission pathway as shown in Fig. 2-6. Normal operation of the MRI system is possible because of the insertion of the dummy load inside the magnet room, enabling RF excitation using the pTx system, as described in an earlier section. For example, using a spectrum analyzer (N9010A, Keysight Technologies, Santa Rosa, CA, USA), signal and noise power measurements can be made at various reference points of interest, enabling a better understanding of the pTx system and identification of potential system improvements. Furthermore, the spectrum analyzer can be interchanged for other measurement devices, such as an oscilloscope, to gain insight into the MRI signal envelope and timing between system channels. This can be important information for automated system calibration development.

Preliminary measurements were conducted in this work using a spectrum analyzer to investigate signal power during gradient-echo imaging (repetition time = 2000 ms, echo time = 2.46 ms, flip angle = 60°, slice thickness = 5 mm, field-of-view = 220 mm) of a uniform poly-acrylic acid phantom (conductivity of approximately 0.47 S/m and relative permittivity of approximately 80), using 4-channel pTx in quadrature mode (constant amplitude and 90º phase offset between RF pulses submitted on successive channels).

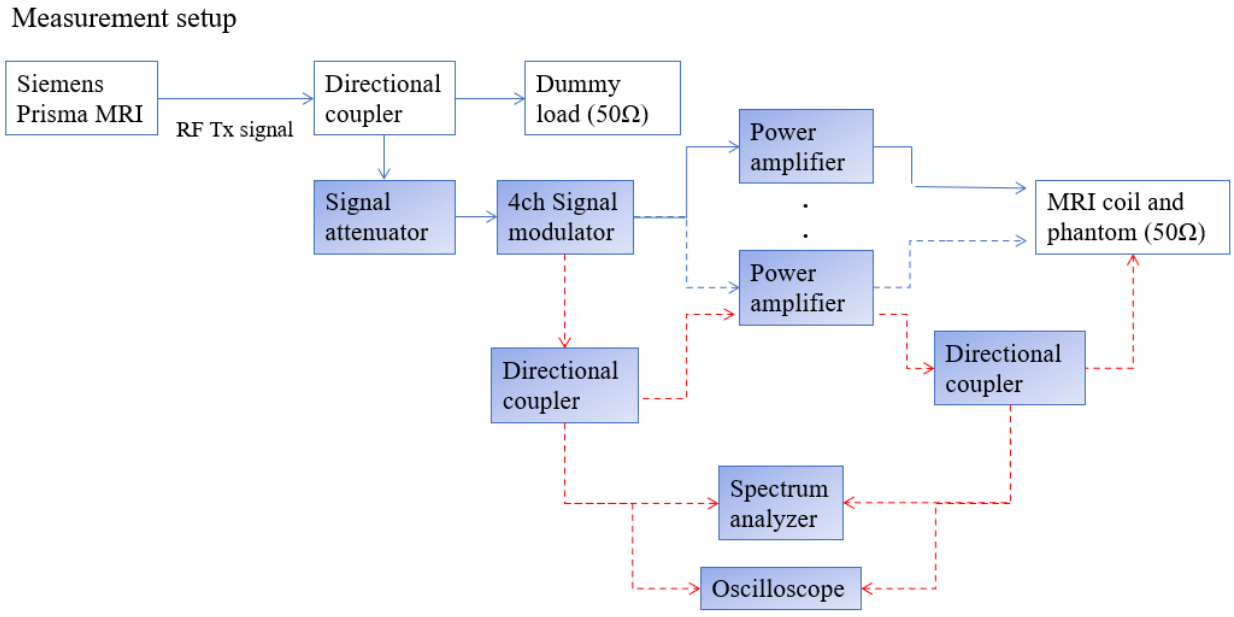

Fig. 2-6: MRI measurement setup for one pTx channel. Shaded boxes represent components inside the equipment room, and unshaded boxes represent components inside the magnet room. Dashed blue arrows are replaced with dashed red arrows when in measurement mode. Signals are independently measured and repeatable for every system channel. Hardware devices can be interchanged for different measurement capabilities.

2.2.2 Experimental Results

The experimental results using a spectrum analyzer for signal power measurements at the input of the RF modulator and output of each RF amplifier according to Fig. 2-6 are shown in Fig. 2-7 and 2-8, respectively. It can be observed that the MRI transmission signal had a good signal-to-noise ratio (SNR) at the resonance frequency of the MRI system at both measurement locations. Furthermore, the noise power at the output of the RF amplifiers was relatively stable across the bandwidth of the RF amplifiers.

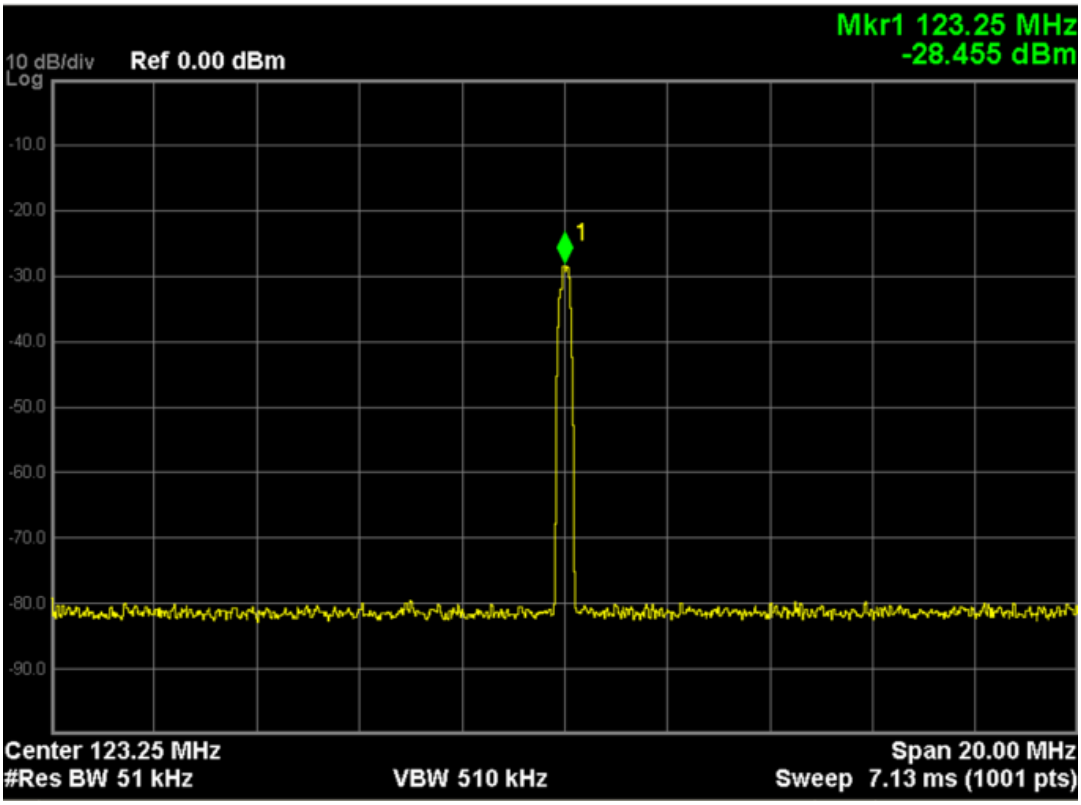

Fig. 2-7: Spectrum analyzer screen capture for gradient-echo imaging (repetition time = 2000 ms, echo time = 2.46 ms, flip angle = 60°, slice thickness = 5 mm, field-of-view = 220 mm) at the input of the signal modulator.

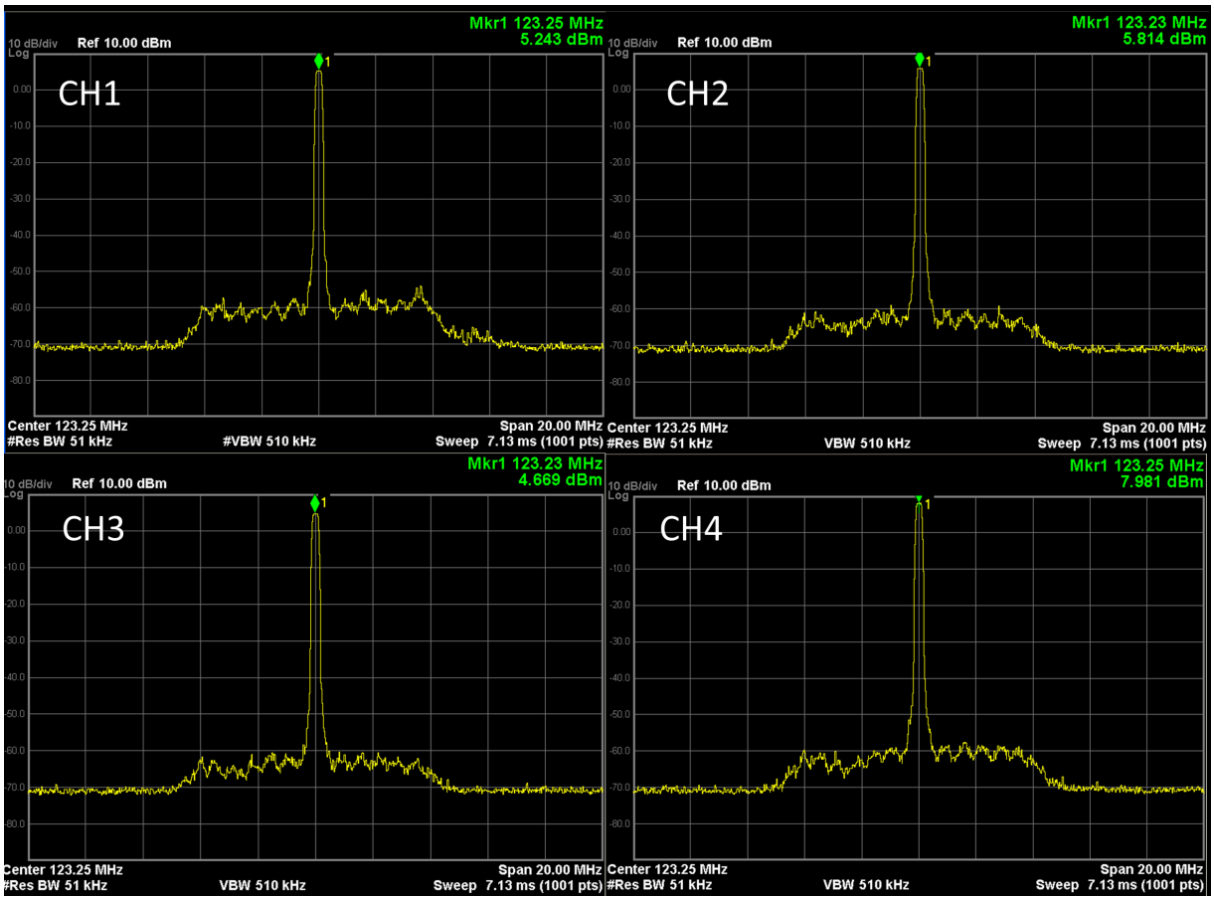

Fig. 2-8: Spectrum analyzer screen capture for gradient-echo imaging (repetition time = 2000 ms, echo time = 2.46 ms, flip angle = 60°, slice thickness = 5 mm, field-of-view = 220 mm) at the output of each RF power amplifier. Channel-to-channel variation in signal power level can be observed, providing useful insight for system optimization development efforts.

2.2.3 Discussion and Conclusion

Fig. 2-7 and 2-8 provided several useful observations; stable signal and SNR at the resonance frequency were observed. However, the measured peak power varied between system channels. This was expected that instrumentation uncertainty would be present between channels and that a calibration process would be necessary to mitigate these effects, as the described pTx safe mode method requires accuracy to produce the correct electromagnetic conditions for DBS device heating minimization. This channel-to-channel system behaviour will likely change for different pTx MRI imaging conditions, which is challenging for benchtop procedures to replicate. Therefore, this measurement setup offers many advantages. For example, a real-time calibration procedure can be implemented to adjust output signals (e.g., for undesired channel-to-channel variation) for different pTx MRI conditions for optimal imaging, like pre-scan routines on

commercial systems, a necessary procedure to optimize system performance. Other important considerations include real-time power and specific absorption rate (or SAR) monitoring.

In conclusion, a useful multi-purpose measurement setup was used to characterize our 4-channel pTx MRI system further. The results suggested further exploration of the pTx safe mode method limitations and the effects of system uncertainty is advisable to ensure safe MRI of DBS patients and is the topic of study in the next section.

2.3 Safe Mode pTx MRI: System Uncertainty

Deep brain stimulation (or DBS) is a highly effective treatment option for patients with certain neurological disorders such as Parkinson's disease and essential tremor [54]. Safe MRI of DBS patients remains a challenge at 3 T because of the increased risks of induced RF heating along the implanted device. At present, DBS patient studies involving 3 T MRI have been limited to low RF power pulse sequences that minimize the risks, which typically are at the expense of image quality [55]. Thus, a 3 T MRI is highly desirable without this limitation.

Parallel RF transmission (or pTx) has recently shown promise in addressing these safety concerns. By utilizing electromagnetic simulation, an optimized set of RF signals can generate an implant-friendly "safe mode" of imaging surrounding targeted regions that contain the conductive implants and, as a result, reduce the risks of induced RF heating effects [56]. With the limited pTx MRI options available commercially, many researchers have explored custom additions to existing MRI systems to demonstrate the benefits of the technology [48]. In practice, accurate replication of the optimized RF signals can be challenging, as instrumentation uncertainty can cause signal deviations, and in the worst case, the safe mode could potentially be compromised. This issue requires careful investigation. The present work thus evaluates system uncertainty (RF transmission error) and failure (complete channel loss) effects in a 4-channel pTx platform for 3 T MRI proposed by Yang *et al.* [48], using electromagnetic simulations of localized specific absorption rate (SAR) and temperature elevation.

2.3.1 Simulation Setup

Electromagnetic simulations were conducted in FEKO (Altair Engineering Inc., Troy, MI, USA) on a homogeneous head model with an implanted insulated copper wire and an exposed tip configured in a patient-derived lead trajectory [51], as shown in Fig. 2-4. The head model material properties include an acrylic shell, grey matter tissue, wire insulation and a perfect copper wire conductor with electromagnetic properties as specified in section 2.1.1. Thermal simulations (the thermal analysis macro in FEKO) were conducted using Penne's bioheat equation, excluding blood perfusion and metabolic effects [57]. The 4-channel pTx MRI safe-mode parameters used in this work were previously derived according to McElcheran *et al.* [56]. These safe mode parameters were then scaled to produce a head SAR average of 1.79 W/kg, which is within the low-end range for high SAR MRI at 3 T reported by MRI scanners (1.48 to 2.5 W/kg) [58]. Initially, a series of local SAR simulations for a spatial position near the exposed wire tip were executed for pTx system errors in transmitted RF phase and amplitude involving a single channel. The investigation was bounded by the manufacturer datasheet specifications for the actual pTx system hardware used (approximately phase: ± 10º and amplitude: ± 0.5 dB) [48]. Next, a worst-case scenario optimization was set to determine the maximum local SAR for any pTx system channel error combination in phase and amplitude within a 1 cm cubic volume encompassing the wire tip and its resultant temperature elevation. The effect of pTx system channel failure was then studied by powering off each channel independently during 4-channel pTx safe mode imaging and evaluating the effect on temperature. Lastly, the effect on magnetic field homogeneity (or B_1) was evaluated.

2.3.2 Simulation Results

Fig. 2-9 shows the electromagnetic simulation result, the percent change in local SAR for errors in phase and amplitude of RF transmission from one channel, with all other channels operating correctly in pTx safe mode. The SAR levels were most sensitive to pTx system errors in channels 2 and 3, with a maximum change (from the safe mode baseline SAR) of approximately 300 % for both channels. Fig. 2-10 shows the simulated temperature rise for the worst-case pTx system error combination in phase and amplitude. A maximum temperature rise of +1.48 ºC was found, exceeding the current +1.0 ºC safety threshold for MRI at 1.5 T [59]. Fig. 2-11 shows the simulated temperature change for pTx system channel failure. RF signal failure in pTx system

channels 2 and 3 resulted in a maximum temperature rise of approximately +7.5 and 8.5 ºC, respectively, a result that greatly compromised the prescribed safe mode. Consistent with the data shown in Fig. 2-9, failure of channel 2 or 3 produced the worst local SAR increases. Fig. 2-12 displays the sum of absolute differences to B_1 homogeneity for the same channel-to-channel deviations. Similar to the SAR result, B_1 homogeneity was most sensitive to channel 2 and 3 changes.

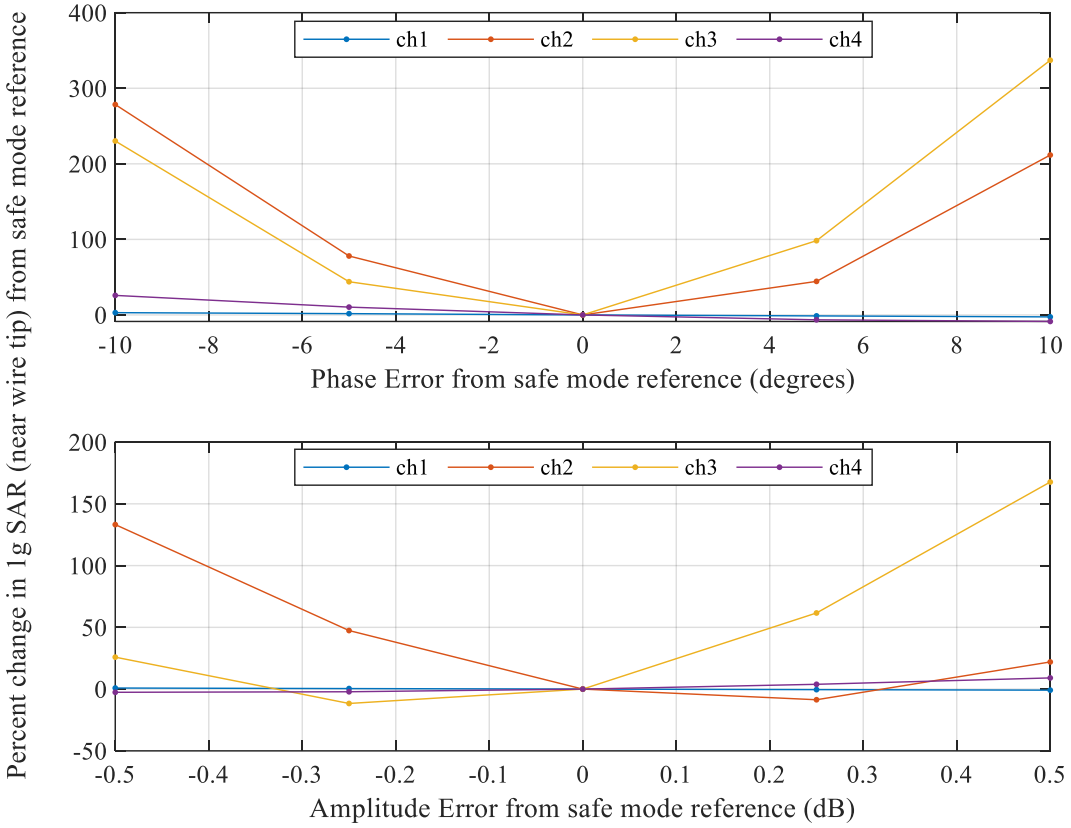

Fig 2-9: The percentage change in local specific absorption rate (near the exposed wire tip) for system deviations from the prescribed safe mode reference in phase (top) and amplitude (bottom). Data are shown for deviations in a single transmission channel (ch1, ch2, ch3, ch4), with all other channels transmitting safe mode values accurately. System uncertainty was bounded by the combined instrument error provided by the manufacturer used to implement the actual parallel radiofrequency transmission system.

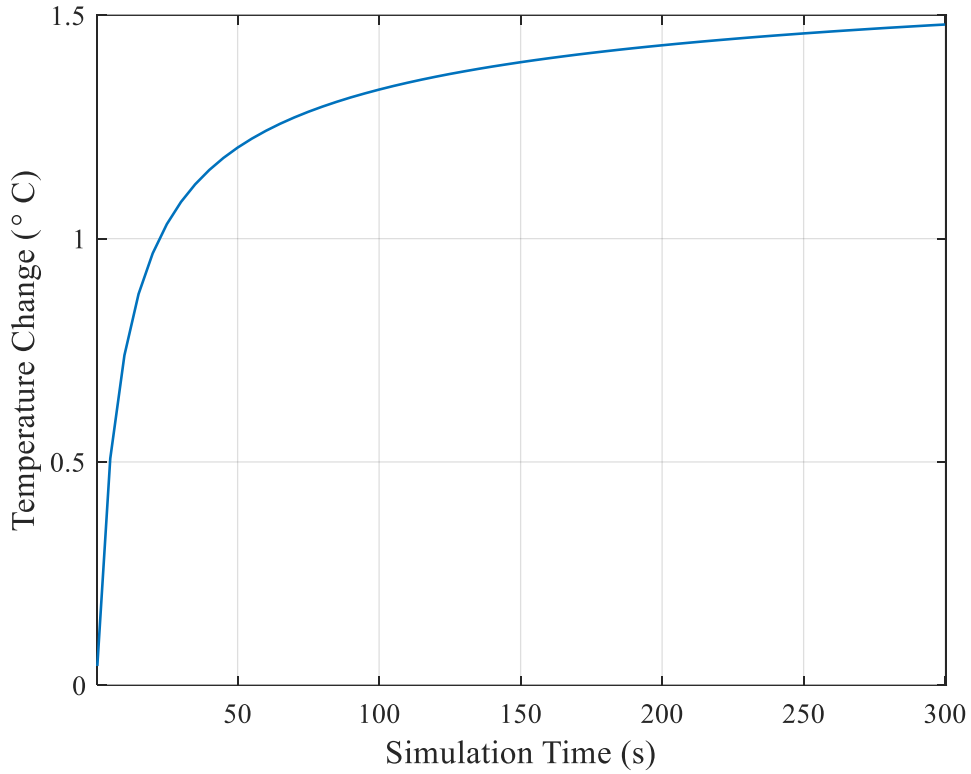

Fig 2-10: Simulated temperature change for the worst-case 4-channel parallel radiofrequency transmission system uncertainty combination in phase and amplitude (channel 1: +3º / 0 dB, channel 2: -10º / -0.2 dB, channel 3: +10º / +0.4 dB, channel 4: +9º / +0.35 dB).

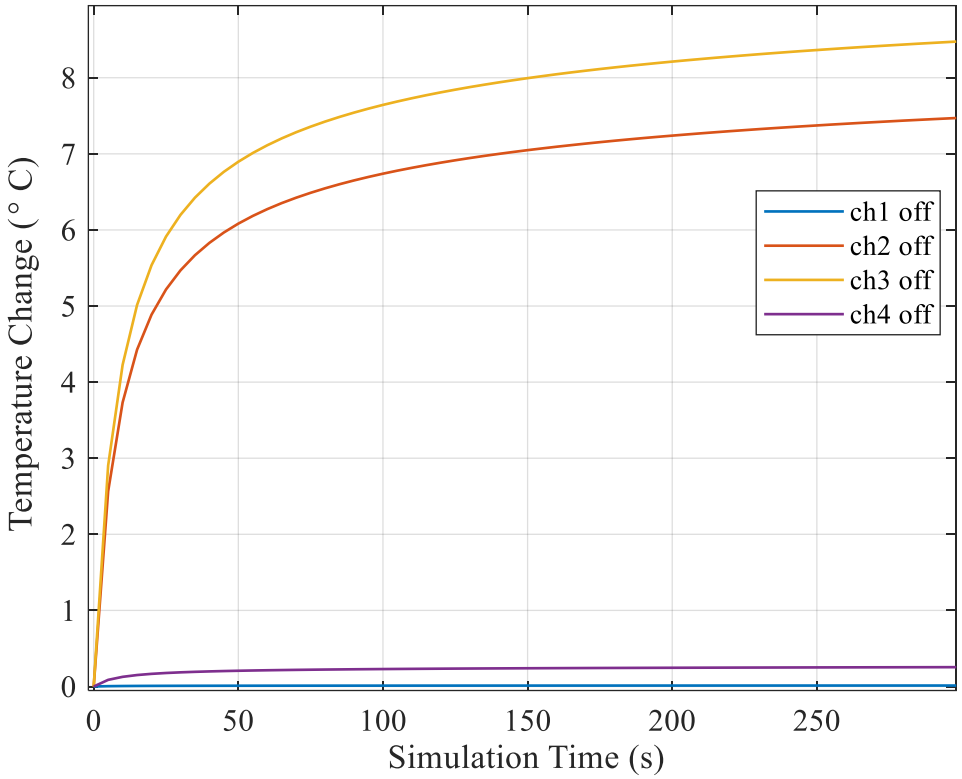

Fig 2-11: Simulated temperature change for the failure of a single channel in the 4-channel parallel radiofrequency transmission system while all other channels continue operating with the corresponding safe mode parameters.

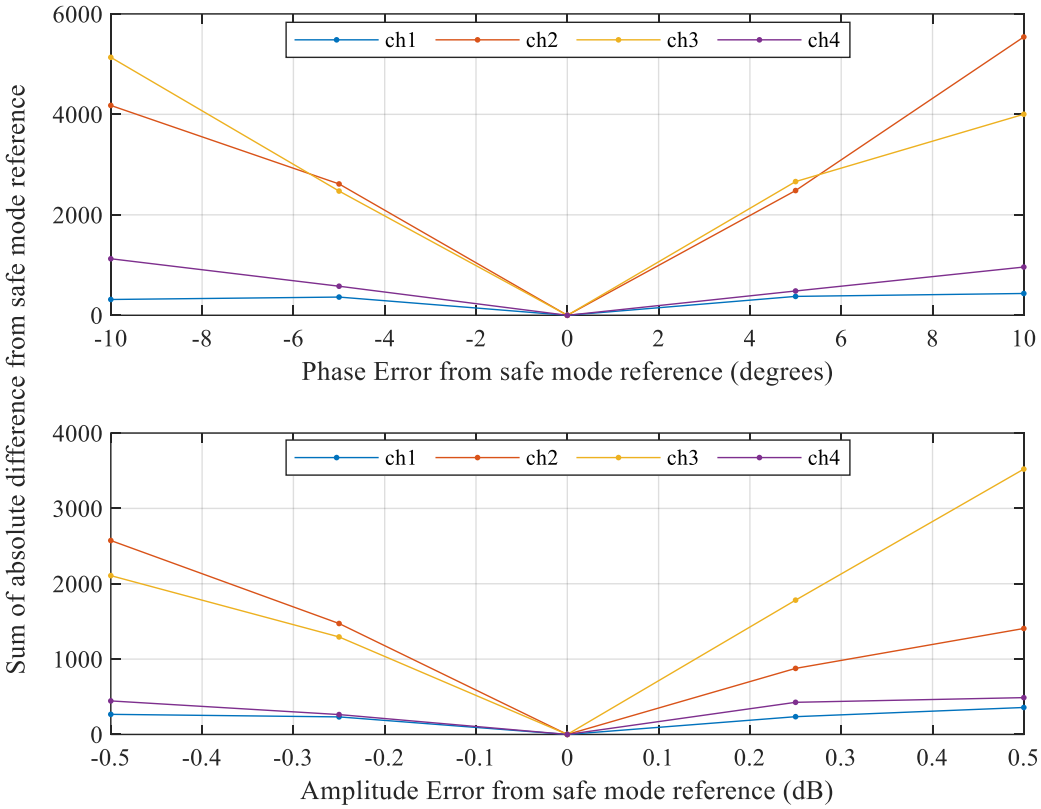

Fig. 2-12: The sum of absolute difference within the whole phantom volume for system deviations from the prescribed safe mode reference in phase (top) and amplitude (bottom). Data are shown for deviations in a single transmission channel (ch1, ch2, ch3, ch4), with all other channels transmitting safe mode values accurately. System uncertainty was bounded by the combined instrument error provided by the manufacturer used to implement the actual parallel radiofrequency transmission system.

2.3.3 Discussion and Conclusion

The simulation showed that temperature elevations were most likely to arise from RF coil elements nearest to the wire tip, as expected, with RF intensity decreasing with distance. In addition, it was evident that two of the four pTx channels made major contributions to pTx MRI safe mode and thus were most sensitive to transmission errors and failure, as shown in Fig. 2-9 and 2-11. It is well documented that RF shimming capabilities improve with a higher system channel count. While two channels were dominant in resolving safety effects and were thus very sensitive to error, it can be hypothesized, from Fig. 2-12, that the other two channels were important for optimizing B_1 homogeneity to counteract some of the negative effects from electric field minimization. This result is consistent with the literature in that significant B_1 homogeneity improvements can be obtained from increasing channel counts on RF receiver coil systems [60].

Lastly, the simulated temperature results indicated that in a worst-case scenario, system uncertainty and channel failure produced concerning temperature increases that exceed the present guidelines for imaging [59]. Additional simulations should thus be conducted to investigate the safety impact of different pTx system configurations, including those with higher channel counts, and this is the topic of study in Chapter 3.

Chapter 3

Parallel RF Transmission (pTx): Effect of System Channel Count

This chapter briefly introduces the history and benefits of multi-channel coil sub-systems in MRI. This is followed by an electromagnetic simulation study, a continuation of the study presented in Chapter 2, investigating the RF heating effects of increasing system channel count on DBS patient safety. The method and results show the potential benefits achievable with higher channel count systems, and the section concludes with a discussion on a possible optimal pTx MRI system configuration. The chapter concludes with a review of a new pTx MRI system design and the fabrication and characterization of a compatible pTx transceiver coil. Part of the work contained in this chapter has been published in,

- B. Yang, C.-H. Chen, and S. Graham, "Technical Note: System Uncertainty on Four- and Eight-Channel Parallel RF Transmission for Safe MRI of Deep Brain Stimulation," *Med. Phys.* 50(9):3745-3751, 2023.

3.1 Multi-Channel MRI Background

MRI is widely used in clinics to diagnose diseases and is increasingly used for functional assessments [61]. However, when compared to other clinically used imaging modalities such as ultrasound or computed tomography, one major disadvantage of MRI is the time required for data acquisition to reconstruct images. This leads to several challenges for patients and overall healthcare management. Longer scan times commonly lead to patient discomfort and cause patient motion, which disrupts the data acquisition process and produces artifacts in the reconstructed image. As a result, causing repeat scans places long-term pressures on the healthcare system as costs and patient wait times rise. A recent study reported in the literature states that the issue of re-scanning originating from patient motion alone is estimated to cost hospitals up to $364,242 annually per scanner [62]. Thus, reducing scan time can significantly improve patient healthcare management. It has become a topic of interest amongst the research community and is particularly

important for DBS patients, as the majority suffer from motor-related disorders such as Parkinson's disease.

In the late 1990s, Sodickson *et al.* proposed and demonstrated the first parallel imaging technique called the simultaneous acquisition of spatial harmonics (or SMASH) to accelerate data acquisition time in MRI [63]. First, the total acquisition time (T_A) of a scan (for a 2-dimensional dataset) can be expressed as [61]

$$T_A = T_R \times N_{pe} \tag{3-1}$$

where T_R is the repetition time (time to acquire one horizontal line in k-space), and N_{pe} is the number of phase-encoding steps (or vertical lines in k-space). T_R affects the contrast in the image, while N_{pe} affects the image resolution. Due to the fast-switching gradients required, there are serious physiological implications with reducing the repetition time, potentially causing unwanted peripheral nerve stimulation in patients. Furthermore, reducing the amount of data collected or the number of k-space lines without implementing other corrective measures will result in poor reconstructed images. Aliasing and blurring in the resultant image are the major consequences of under-sampling k-space. Fig. 3-1 demonstrates this concept for MRI of a human brain, and the effects of k-space under-sampling in two scenarios are shown. As a result, data processing methods were studied and developed to resolve the image artifacts associated with k-space under-sampling (i.e., reducing N_{pe} or the number of k-space lines collected) and were known in MRI as parallel imaging.

The basic concept of parallel imaging techniques is the process of populating k-space utilizing the data collected from multiple receiver coils in parallel. Each receiver coil represents a partially filled k-space due to under-sampling. However, with knowledge of the coil sensitivity profiles, spatial localization of the received information can be organized and combined such that a full k-space data set is populated, essentially the missing lines in k-space required to reconstruct full resolution and field-of-view images without aliasing or blurring artifacts are filled. This concept is illustrated in Fig. 3-2. According to equation (3-1), the scan time reduction is directly proportional to the number of phase-encoding steps; thus, significant time savings can be achieved, and parallel imaging techniques have since then been widely used and become standard practice in clinics. Several newer techniques, such as sensitivity encoding (or SENSE) and generalized

auto-calibrating partial parallel acquisition (or GRAPPA), have been developed and are available as a part of current clinical MRI systems.

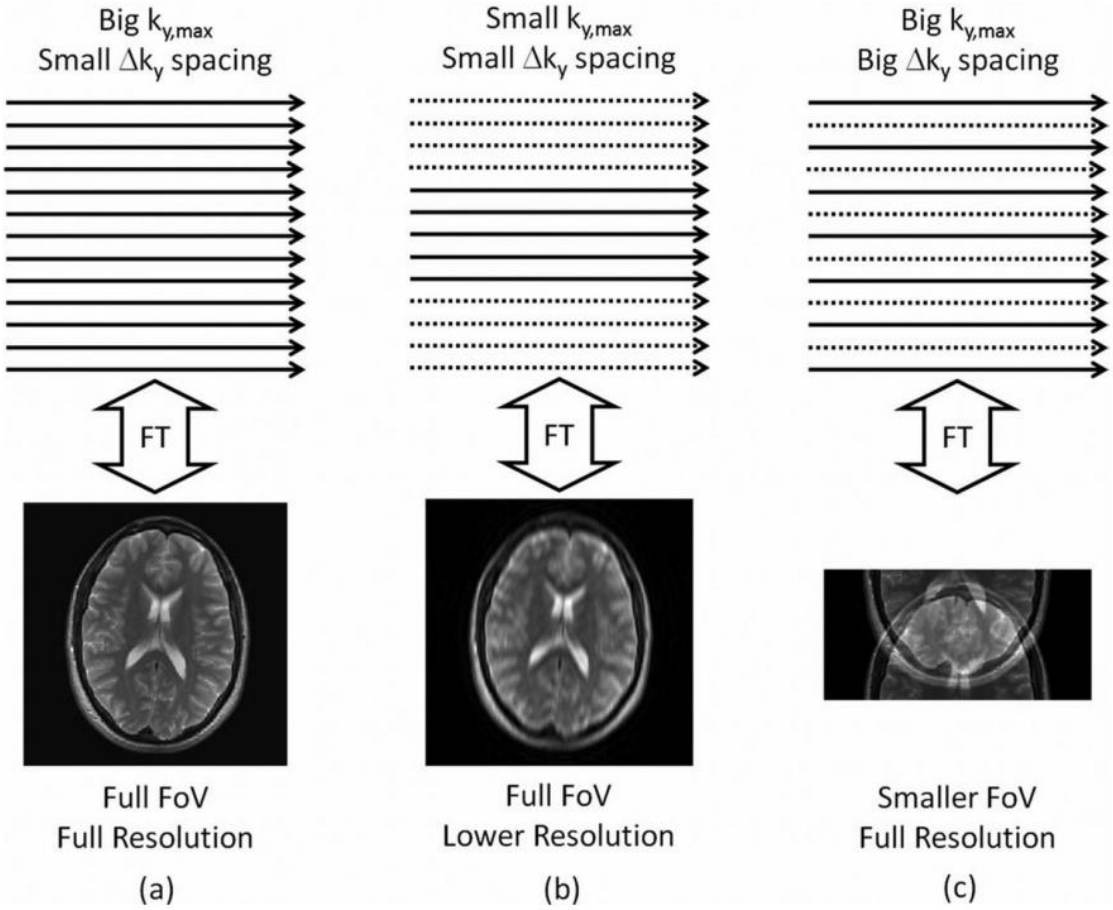

Fig. 3-1. An illustration of the effects of k-space under-sampling in the phase-encoding direction (k_y for 2-dimensional imaging dataset). The solid line represents the data sampled in k-space for image reconstruction. Figure (a) illustrates the scenario of a full k-space data acquisition and displays the effect on a reconstructed human brain image, (b) illustrates the scenario of k-space under-sampling for a small k_y max and spacing and displays the effect on a reconstructed human brain image and (c) illustrates the scenario for k-space under-sampling for a big k_y max and spacing and displays the effects on a reconstructed human brain image [61]. FoV = field-of-view; FT = Fourier transform.

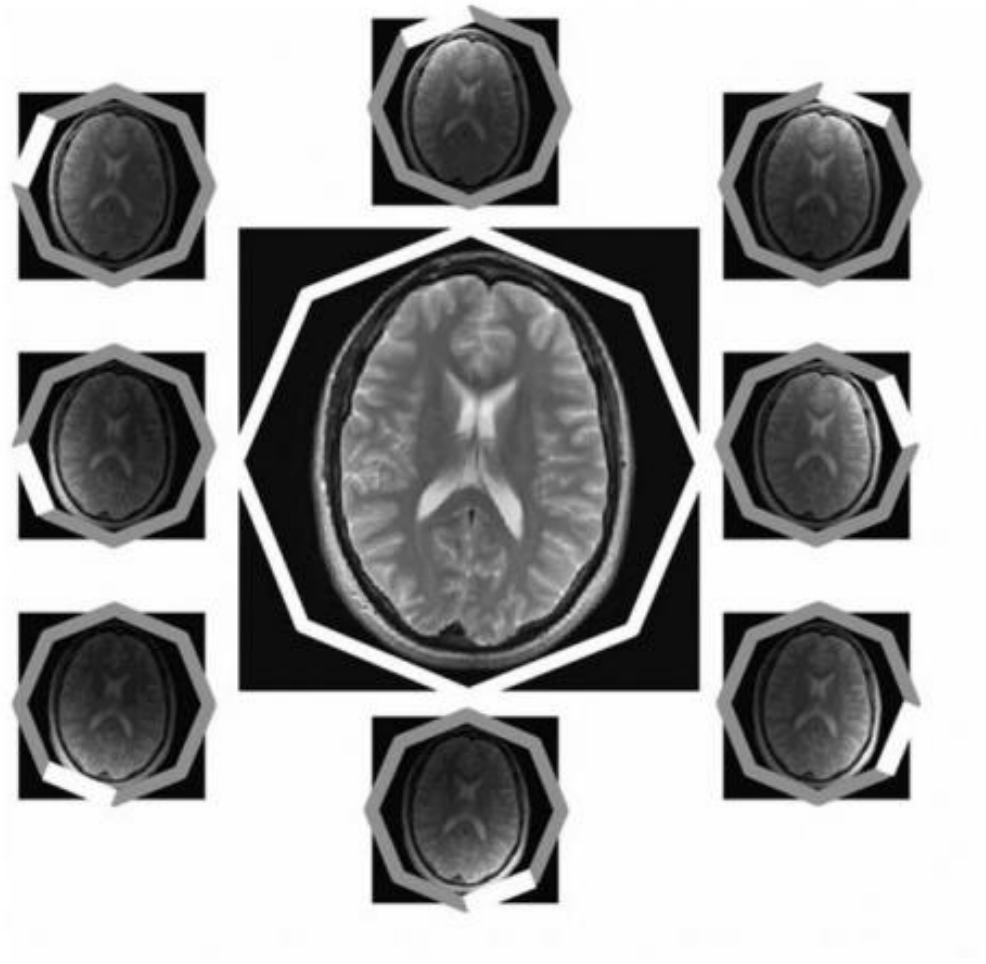

Fig. 3-2. An illustration of the basic concept of parallel imaging. The sublet images highlight the active field of view of each contributing system receiver channel. The centre image is the fully reconstructed image representing the summation of all receiver channel datasets with the appropriate coil sensitivity weightings [61].

Shortly after, in the early 2000s, the same principles were applied to the MRI RF transmission pathway and became known as parallel radiofrequency transmission (or pTx). It was also originally demonstrated for accelerated imaging applications, as described in Chapter 1. The applications for pTx have evolved tremendously since its introduction and have proven to be instrumental in addressing the challenges of ultra-field MRI systems, such as increased RF power deposition, worsening susceptibility artifacts in images, and B_1 inhomogeneities [64]. Parallel transmission techniques such as reduced field-of-view (r-FoV), whereby a targeted region-of-interest is imaged to reduce image distortion, has been demonstrated to improve prostate and spinal

cord imaging [65] and simultaneous multi-slice (SMS), whereby data acquisition of multiple slices is collected in parallel can significantly reduce imaging time [66]. Both r-FoV and SMS are the two major MRI techniques now offered on newer clinical scanners.

With parallel imaging and pTx, the general trend that can be expected is that imaging benefits scale directly with the number of system channels available. This has been the case, particularly for parallel imaging applications, as designs for receiver coil sub-systems of up to 128 channels have been reported in the literature and demonstrated to improve image quality and signal-to-noise ratio [67]. However, for pTx, although a similar trend is expected, optimal pTx system configurations remain unclear and require study.

Currently, only dual-channel pTx MRI systems are available commercially at 3 T magnetic field strengths and 8- or 16-channel systems at 7 T magnetic field strengths. Increasing system transmission channels is a non-trivial endeavor. High hardware costs are associated with any type of pTx system build-out, and system channel modifications after installation are not advisable. Therefore, researchers continue to develop add-on pTx systems for flexibility and determining an optimal system configuration that can address a wide range of clinical challenges is thus an important topic. Chapter 2 presented results demonstrating system uncertainty effects for a 4-channel pTx setup. The following section expands on this study to explore the impact of higher system channel counts and the associated pTx safe mode technique for DBS patient safety at 3 T.

3.2 Safe Mode pTx MRI: Effect of System Channel Count

Parallel radiofrequency transmission (or pTx) is a promising method to address some technical challenges - such as RF magnetic field (B_1) inhomogeneities and localized power deposition – encountered when conducting MRI at higher static magnetic field strengths. The pTx method relies on the combined effects of multiple dedicated RF input signals and transmission channels to generate a desired imaging electromagnetic profile. There are two main pTx approaches: (1) "RF-shimming", which enables the amplitude or phase of a single common RF source to be adjusted on each channel; and (2) "full-pTx", which utilizes fully independent RF waveforms across all channels. The choice of which approach to adopt depends on the system hardware available and the MRI application of interest. In particular, both approaches show promise for reducing MRI safety concerns at higher static magnetic field strengths (i.e., ≥ 3 T). As

the magnetic field increases, patient safety challenges become more of a concern because of the increasing electric field component of the overall electromagnetic field and the potential for constructive or destructive interference of RF waves within the imaging volume. This can generate local hotspots within the human body capable of causing severe tissue damage [68]. This effect is particularly concerning for patients with implanted DBS devices. At present, there are over 150,000 patients with DBS implants worldwide, a number that is likely to grow significantly [69]. However, MRI of this patient group is currently restricted to clinically approved conditional imaging protocols (typically, low-power RF pulse sequences involving specific RF coil hardware) that can limit the medical diagnostic capability of MRI [70, 71]. In many centers, MRI of DBS patients is not adopted at all due to the perceived risks, yet it has been reported that the majority of DBS patients are likely to require MRI within a 5-10 year period as a result of their pre-existing condition or other comorbidities [72]. Presently (at the time of this writing), the Medtronic Percept DBS system is the only regulatory-approved neurostimulator with MRI conditional labeling that allows for 1.5 and 3 T full-body MRI, increasing the need to ensure DBS patient safety at 3 T and above in the immediate future [73].

Commercially available pTx MRI systems can be very costly. As a consequence, researchers often rely on custom add-on hardware integrated into existing MRI systems to conduct technical development and demonstrate pTx efficacy. For example, Yang *et al*. recently developed a scalable 4-channel pTx MRI platform and demonstrated a pTx safe mode technique for addressing DBS MRI safety concerns at 3 T, which was used throughout this thesis for experimental validation of results [74]. The benefits of safe mode pTx MRI require accurate RF signal generation to produce a desired electromagnetic imaging scenario [75]. In practice, however, system uncertainty (or instrumentation error) is likely to impact the accuracy of the pTx MRI system to deliver the required RF signals, potentially introducing a safety concern to DBS patients during imaging. Some of the effects can be observed in the simulation results presented in Chapter 2. Thus, system uncertainty is an important topic to investigate further. It is hypothesized that increasing the system channel count may offer some additional safety benefits to mitigate these concerns.

The present work studies the system uncertainty of an 8- and 16-channel system configuration that is based on the research pTx MRI platform presented in Chapter 2 [74] and the

associated implications for DBS patient safety at 3 T. Electromagnetic and thermal simulations are conducted for instrumentation errors according to the manufacturer's technical specifications. A worst-case scenario is determined for each pTx setup.

3.2.1 Simulation Setup

Electromagnetic and thermal simulations were executed in FEKO (Altair Engineering Inc., Troy, USA). The system uncertainty analysis was bounded by the maximum combined manufacturer's specified errors for the 4-channel RF modulator (CGP-128-4C, CPC, Hauppauge, USA) and the RFPAs (BT01000-AlphaSA, Tomco Technologies, Stepney, AUS). The resultant amplitude and phase error were approximately ± 0.5 dB and ± 10°, respectively. The remaining hardware components of the pTx MRI platform are passive devices with minimal error contribution [74]. For example, coaxial cables were carefully cut to minimize phase delay variations between system channels. Fig. 3-3 (a) and (b) display a FEKO model of the potential 8- and 16-channel transceiver RF coil, respectively, that can be adapted onto the existing pTx platform. The coil design is a possible option that may address some limitations of the 4-channel pTx setup, primarily the temperature elevations under the worst-case system error and channel failure scenarios presented in Chapter 2. Furthermore, RF heating effects caused by patient motion may also be reduced, a topic discussed in Chapter 4 [76]. Fig. 3-3 (c) displays the homogeneous head-shaped phantom (as specified in Chapter 2) and the patient-derived DBS lead trajectory (modelled as insulated copper wire) that was used in the simulation. The simulation results are expected not precisely to depict actual DBS patient imaging. However, the simplified model is sufficient for initial exploration to determine the effects of increasing system channel count, and the heat transfer characteristics of DBS leads remain reasonably represented by copper wire for this purpose [77].

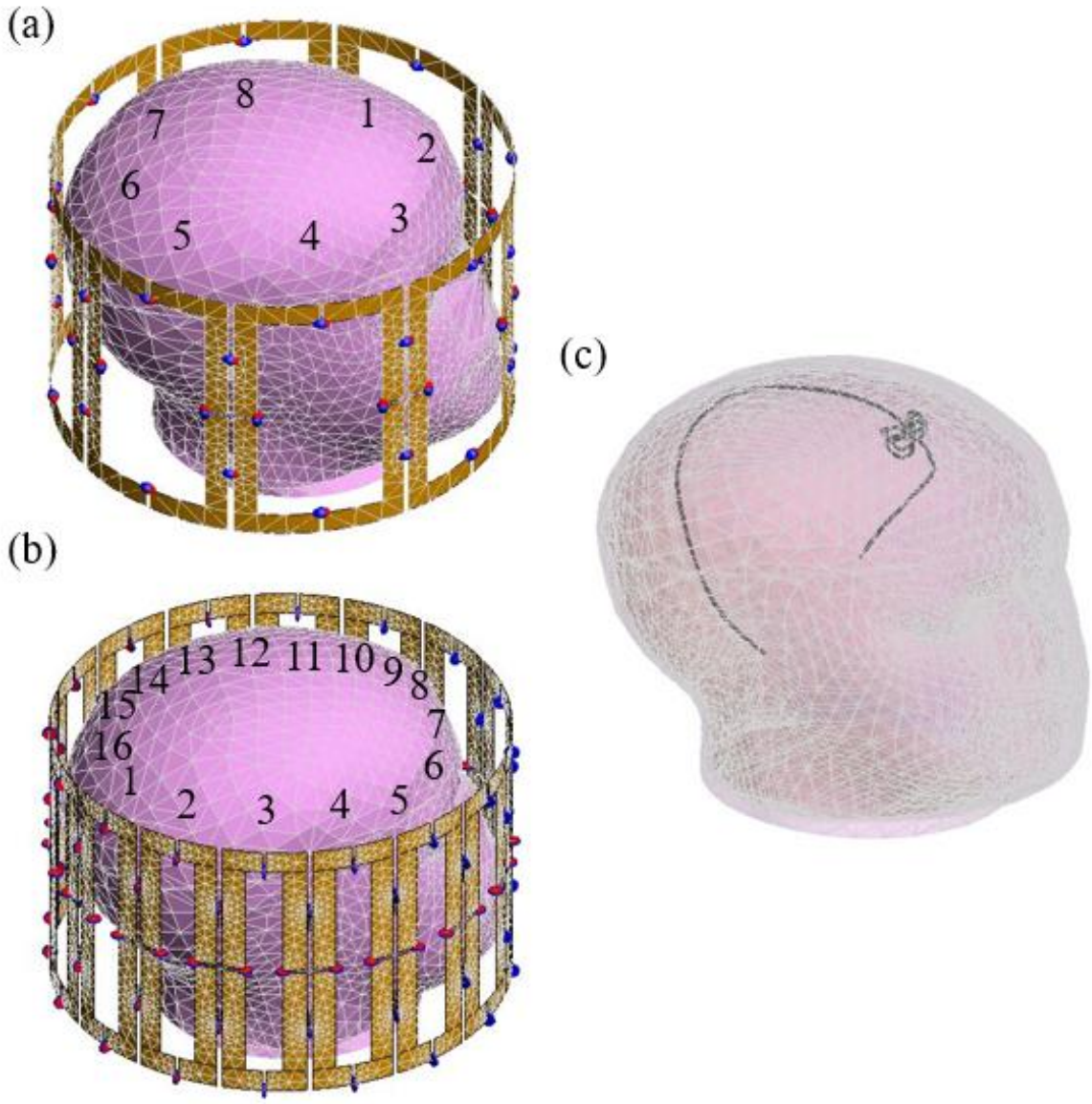

Fig. 3-3: (a) 8-channel and (b) 16-channel radiofrequency transceiver coils (as labelled) and head model used in the electromagnetic simulation. (c) Head model and patient-derived deep brain stimulation lead trajectory used to evaluate localized radiofrequency heating effects.

To generate the respective pTx MRI safe modes (based on optimization in a region surrounding the lead tip), the channel-specific RF inputs (amplitude/phase) used for the 8-channel setup were approximate: channel 1, -3.5 dB / 34.1º; channel 2, -5.0 dB / 69.3º; channel 3, -3.7 dB / 40.1º; channel 4, -4.0 dB / 169.8º; channel 5, -2.5 dB / 237.3º; channel 6, -2.0 dB / 201.6º; channel 7, -4.0 dB / 272.5º; and channel 8, -3.5 dB / 243.9º. Similarly, for the 16-channel setup, the inputs were: channel 1, -2.8 dB / 19.4º; channel 2, -2.5 dB / 51.8º; channel 3, -2.8 dB / 103.8º; channel 4,

-3.0 dB / 136.8º; channel 5, -2.8 dB / 183.9º; channel 6, -2.1 dB / 238.7º; channel 7, -3.0 dB / 279.6º; channel 8, -2.1 dB / 330.3º; channel 9, -2.5 dB / 40.3º; channel 10, -2.9 dB / 59.8º; channel 11, -2.9 dB / 108.9º; channel 12, -3.0 dB / 141.4º; channel 13, -3.2 dB / 142.6º; channel 14, -3.2 dB / 272.0º; channel 15, -2.8 dB / 322.2º; channel 16, -3.0 dB / 320.0º. Penne's bioheat equation, simplified by removing the metabolic and perfusion effects, was utilized to predict the temperature elevations and evaluate RF heating effects at the lead tip location [78].

First, an electromagnetic simulation was set up to verify that the proposed pTx safe mode technique can reduce the RF heating effects at the lead tip for the proposed 8- and 16-channel pTx setups. The simulation was executed for RF excitation in quadrature mode (a scenario that can produce more significant RF heating effects, whereby each system channel has a constant amplitude and phase offset of 45º and 22.5º in the 8- and 16-channel pTx setup, respectively) and in safe mode (whereby each system channel was set to the respective values described above). A thermal analysis followed (using the simplified Penne's bioheat equation as described in Chapter 2), predicting the temperature change over a prescribed period. The results were expected to be consistent with previous work [74, 75]. For easy comparison between previous 4-channel results and the 8- and 16-channel pTx configurations, the RF input power was scaled such that a simulated whole head volume specific-absorption-rate (SAR) of approximately 1.79 W/kg was estimated - a SAR level for spin-echo-based MRI pulse sequences that is within in the range reported by 3 T scanners (1.48 to 2.5 W/kg) [79].

This was followed by, first, the "worst-case analysis" study by using electromagnetic simulation optimization (bounded by the amplitude/phase error range above) to determine the channel-specific combination of system error in both pTx setups that produced the most significant temperature elevation at the lead tip. Second, similarly, the system channel failure scenario was studied to assess the safety implications that could arise in the event of intermittent or complete failure of a single pTx channel. For this scenario, the RF voltage for each channel was set to zero sequentially (and separately), with the remaining pTx channels set to their respective ideal pTx safe mode parameters. Lastly, a B_1^+ homogeneity comparison over the whole head volume was conducted that compared the different pTx system safe mode B_1^+ data to evaluate potential image quality benefits that may be achievable. This involved equating the mean of each B_1^+ dataset and then calculating the standard deviation for comparison.

3.2.2 Simulation Results

As expected, the proposed pTx safe mode RF shim technique performed well, and the simulated temperature elevation at the lead tip was suppressed by over 99 % (when compared to analogous pTx results in quadrature mode) – producing a maximum temperature increase of just +0.16 ºC across both pTx setups, consistent with previous simulation and experimental work at 4-channels [74, 75]. The simulated temperature change results are shown in Fig. 3-4.

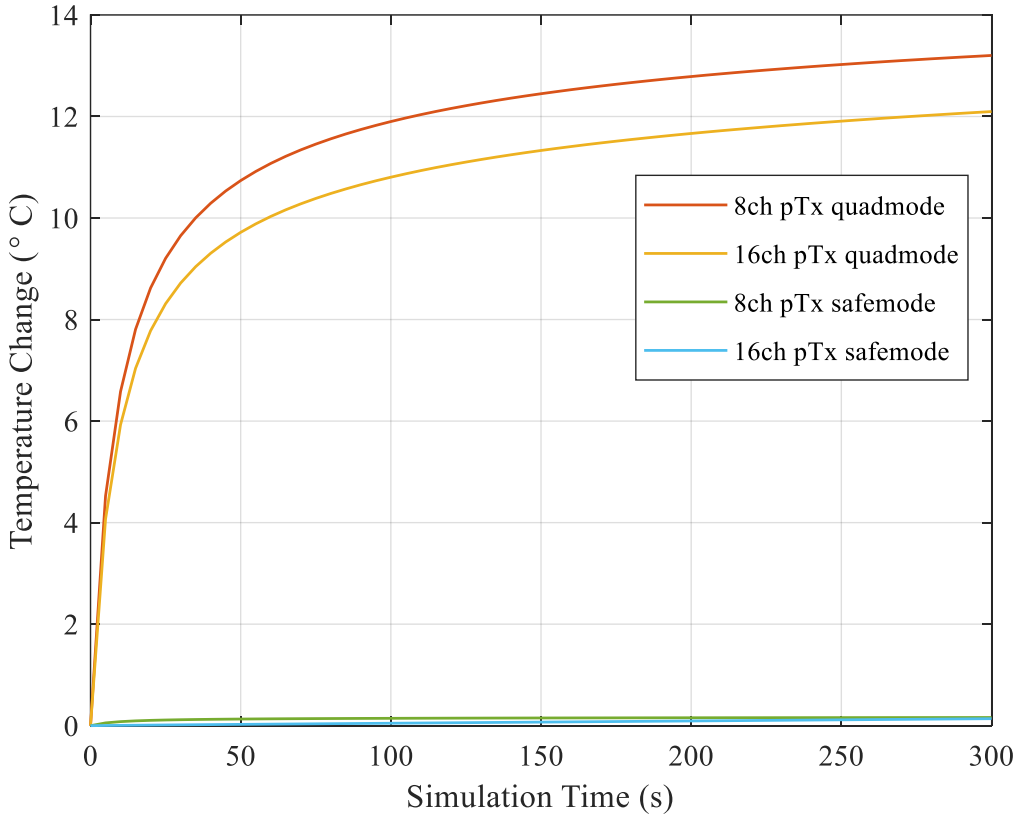

Fig. 3-4: 8- and 16-channel parallel radiofrequency transmission temperature change results at the lead tip for system operation in (a) quadrature mode (constant amplitude and next neighbour system channel phase offset of 45º and 22.5º for 8- and 16-channel setups, respectively and (b) safe mode (8-channel setup: channel 1, -3.5 dB / 34.1º; channel 2, -5.0 dB / 69.3º; channel 3, -3.7 dB / 40.1º; channel 4, -4.0 dB / 169.8º; channel 5, -2.5 dB / 237.3º; channel 6, -2.0 dB / 201.6º; channel 7, -4.0 dB / 272.5º; and channel 8, -3.5 dB / 243.9º and 16-channel setup: channel 1, -2.8 dB / 19.4º; channel 2, -2.5 dB / 51.8º; channel 3, -2.8 dB / 103.8º; channel 4, -3.0 dB / 136.8º; channel 5, -2.8 dB / 183.9º; channel 6, -2.1 dB / 238.7º; channel 7, -3.0 dB / 279.6º; channel 8, -2.1 dB / 330.3º; channel 9, -2.5 dB / 40.3º; channel 10, -2.9 dB / 59.8º; channel 11, -2.9 dB / 108.9º; channel 12, -3.0 dB / 141.4º; channel 13, -3.2 dB / 142.6º; channel 14, -3.2 dB / 272.0º; channel 15, -2.8 dB / 322.2º; channel 16, -3.0 dB / 320.0º). Quadrature mode recorded temperature of elevations of +13.2 ºC for the 8-channel setup and +12.1ºC for the 16-channel setup, and safe mode recorded temperature elevations of +0.16 ºC and +0.13 ºC, respectively.

Fig. 3-5 plots the temperature results that predicted the worst-case 8- and 16-channel pTx RF input error combination (as determined by FEKO, 8ch: channel 1, -4.0 dB / 39.5º; channel 2, -

5.0 dB / 68.4º; channel 3, -3.5 dB / 35.7º; channel 4, -3.5 dB / 178.3º; channel 5, -2.0 dB / 241.6º; channel 6, -2.0 dB / 192.1º; channel 7, -4.5 dB / 282.0º; and channel 8, -4.0 dB / 233.9º and 16ch: channel 1, -2.8 dB / 14.9º; channel 2, -2.1 dB / 52.6º; channel 3, -3.0 dB / 111.1º; channel 4, -2.8 dB / 133.9º; channel 5, -3.0 dB / 177.8º; channel 6, -2.1 dB / 229.4º; channel 7, -3.2 dB / 270.3º; channel 8, -2.5 dB / 320.1º, channel 9, -3.0 dB / 49.9º; channel 10, -3.2 dB / 68.8º; channel 11, -2.1 dB / 118.9º; channel 12, -2.5 dB / 150.8º; channel 13, -3.0 dB / 151.8º; channel 14, -3.2 dB / 262.0º; channel 15, -3.1 dB / 313.0º; and channel 16, -2.1 dB / 324.1º). The 4-channel result is also plotted for reference. The resultant maximum temperature elevations for the 8 and 16-channel pTx conditions were +0.85 and +2.09 °C, respectively. These simulation results indicate that in a worst-case system uncertainty scenario, it is very possible for specific pTx system configurations to exceed the present MRI safety limit of +1.0 °C (for MRI at 1.5 T) during whole head pTx imaging.

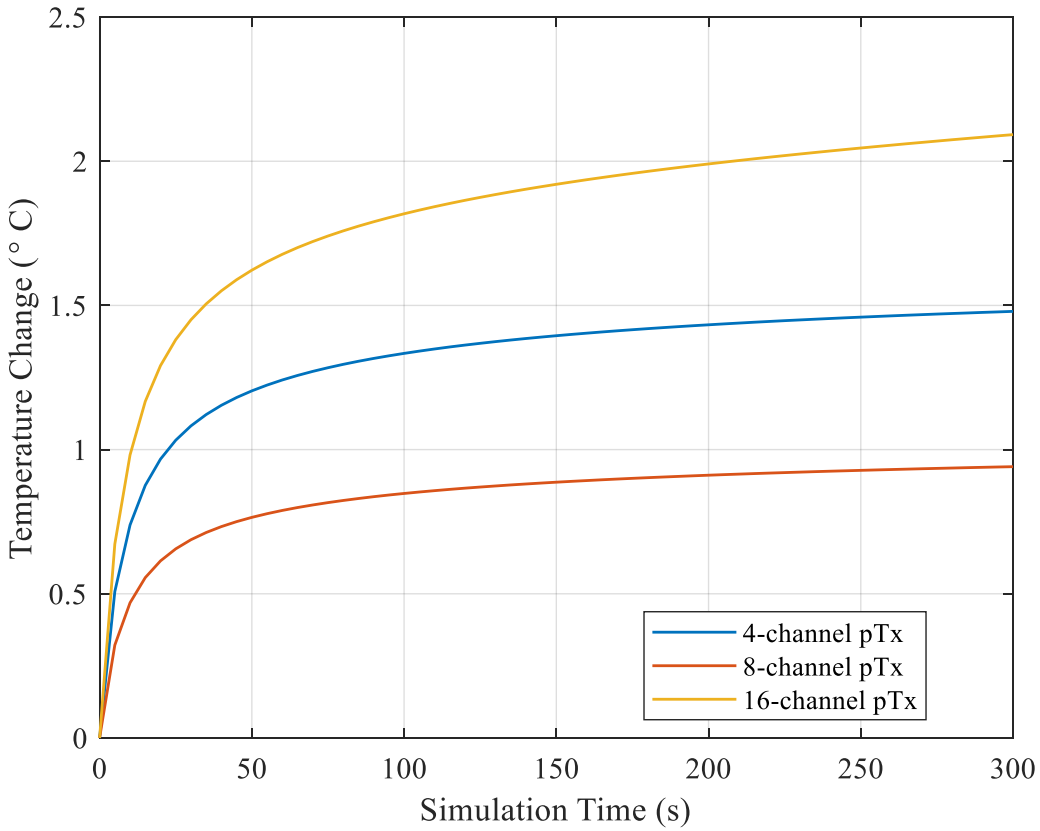

Fig. 3-5: 4-, 8-channel and 16-channel pTx MRI simulated temperature elevation at the lead tip for the worst-case system uncertainty combination (determined by electromagnetic simulation and constrained by system error). Maximum temperature elevations of +1.48, +0.85 and +2.09 ºC were found for the 4-, 8- and 16-channel pTx setups, respectively.

Based on the results observed in Fig. 3-5, it strongly suggested that for the three pTx setups studied, the 8-channel pTx setup offered the strongest advantages compared to the 4- and 16-channel setups. For this reason, the 8-channel pTx setup became the primary focus for the subsequent studies. For the B_1^+ analysis, it showed that an increase in the system channel count from 4 to 8 produced an approximate 60 % improvement in overall B_1^+ homogeneity when in pTx safe mode – a result that was expected and consistent with previous work [80]. Further inspection under the worst-case scenario showed that the overall B_1^+ homogeneity for the whole head volume was also negatively impacted by approximately 150 and 60 % compared to their ideal 4- and 8-channel pTx safe mode results. Fig 3-6 displays the temperature elevations for pTx system single channel failure in the 8-channel pTx condition. The results showed that specific pTx channel failures could lead to elevated levels of RF heating that risk exceeding present safety guidelines. The maximum temperature increase of 4.3 °C in the 8-channel pTx setup was substantially lower than the 8.4 °C in the 4-channel pTx setup. These results demonstrated that improved DBS patient safety and image quality benefits appear achievable with an 8-channel pTx setup.

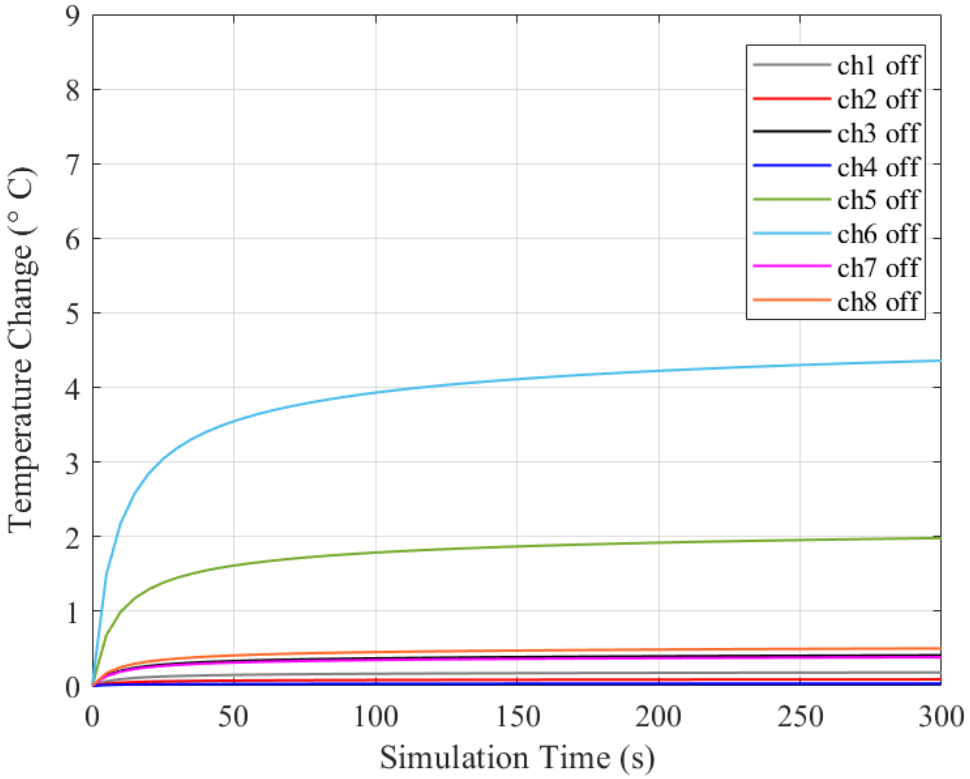

Fig. 3-6: Simulated temperature change for the failure of a single channel in the 8-channel pTx system while all other channels continue operating according to safe mode. A maximum temperature of +4.3 °C was predicted for the failure of channel 6.

3.2.3 Discussion and Conclusion

With the future goal of imaging DBS patients at 3 T, studying pTx system uncertainty effects is essential to ensure patient safety and to investigate the potential limitations of the pTx safe mode. The present work evaluated the potential impact of system uncertainty in an 8 and 16-channel pTx system setup based on the technical specifications of a novel research pTx platform [74]. The overall results showed that the proposed pTx safe mode method was sensitive to system errors, and the initial findings suggest that some of the 4-channel system limitations can be improved using an 8-channel system.

Several important findings merit discussion. First, the lead tip was most sensitive to RF transmission from the nearest coil elements. This is a logical result as RF intensity attenuates with distance. Second, the proposed RF shim technique continued to show promise, as RF heating effects reductions of 99 % were achieved in the 8-channel and 16-channel pTx setups. It is important to note that the pTx implant-friendly safe mode technique is not limited to a specific pTx configuration, and continued research will be required to determine the configuration that is most practical for clinical implementations. Third, the worst-case pTx system uncertainty analysis estimated a potential +0.85 and 2.09 ºC temperature elevation (at the lead tip) for the 8- and 16-channel pTx setups, respectively. Compared to the +1.48 ºC temperature elevation in the 4-channel pTx setup, a strong advantage is observed at 8 channels. The 16-channel system uncertainty result exceeded both the current MRI safety guideline and the 4-channel result suggesting that there may be a practical system limitation to increasing system transmission channels and that the added RF signal modulation flexibility gained from higher system channels can potentially compromise the proposed implant-friendly safe mode — an important safety concern and a result that led to a focused effort on the 8-channel pTx setup. Furthermore, a significant cost advantage would also be expected with developing an 8-channel system versus a 16-channel version.

The B_1^+ results showed that a 60 % gain in magnetic field homogeneity is possible with the proposed 8-channel pTx configuration compared to the 4-channel pTx configuration, and consequently, an associated gain in image quality is expected. This is a promising result and an option to explore in addressing the 4-channel pTx safe mode trade-off in suppressing localized heating at the expense of B_1^+ homogeneity, as reported in one of our recent studies [76]. A lower

temperature elevation with greater B_1^+ homogeneity was shown for the worst-case scenario in the 8-channel pTx setup, and the peak 1g SAR was also reduced by up to 25 % when comparing the 4-channel case in Fig. 2-9, further suggesting that a pTx system at this channel count may be advisable for the present application.

Last, the system channel failure analysis provided further evidence that the nearest coil elements most impacted the RF heating at the lead tip. Moreover, the safe mode effect was most sensitive to failures of two channels, like in the 4-channel case (see Fig. 2-11). This suggests that the generation of the pTx safe mode critically depended on these corresponding pTx channels; and that the remaining pTx channels aided in resolving B_1^+ inhomogeneities. Once more, better results (i.e., less heating) were observed for the 8-channel pTx configuration. As a result of this work, there is a solid rationale to increase the pTx system channel count to 8 channels for DBS applications at 3 T involving safe mode. In addition to system uncertainty, patient motion and mispositioning may also affect pTx safe mode capability, and their combined effect as a function of channel count should be carefully studied in the future [76].

The limitations of this work also require discussion. First, promising results have been demonstrated but remain preliminary and cannot be considered entirely conclusive. The simulations were based on a specific head model and geometry (with an implanted copper wire), DBS lead trajectory and technical specifications of a particular set of hardware devices. Although the simulation results provided valuable insight into the heating behavior of an actual DBS lead, the absolute temperature elevations may differ from those obtained in actual MRI experiments with real DBS devices. However, the benefits of the 8-channel pTx MRI system are evident compared to 4- and 16-channel pTx. Second, it is common for DBS patients to receive bilateral implants, and the management of excess DBS lead length varies across patients. The results presented in this work represent just one of the possible DBS lead trajectories and do not consider the bilateral implant scenario. Lastly, the SAR level used may not represent a clinical pTx TSE sequence. However, it is an appropriate metric to demonstrate potential safety benefits for research purposes. Furthermore, it was expected that the 8-channel setup would offer some improvements in system power efficiency and imaging flexibility over the 4-channel setup [81].

In conclusion, the present work suggests that the implant-friendly pTx safe mode is sensitive to system uncertainties, and in a worst-case scenario, the DBS lead tip may experience significant temperature elevations. When comparing the 4-, 8-, and 16-channel pTx configurations, the 8-channel pTx setup is less sensitive to system uncertainties and should be investigated more in the future for 3 T MRI applications involving DBS patients. Although the presented results are promising and support 8-channel system development, RF heating effects in DBS devices are complex, with dependencies across multiple variables, each requiring in-depth study. Future work includes the expansion of the research pTx MRI platform to 8 channels and further experimental verification using a commercial DBS device and a novel anthropomorphic phantom capable of replicating realistic lead trajectories [82].

3.3 An Optimal pTx MRI System Configuration

The system uncertainty study provided significant insight into the limitations of the present 4-channel pTx system. The electromagnetic simulation studies strongly suggested that a higher channel count system would offer additional flexibility to improve DBS patient safety at 3 T. The results also indicated that the benefits of moving to a higher channel count system appear to saturate, and as shown for the worst-case scenario study, a compromised "safe mode" may be possible at 16 channels. The 8-channel pTx setup shows promising results for DBS applications and, from a practical and economic standpoint, would be a worthwhile upgrade from the current 4-channel pTx setup. This section briefly introduces the new pTx system capable of full pTx mode designed by Yang *et al.* that follows the same integration procedure presented in Chapter 2 [83] and presents the construction of a custom 8-channel pTx transceiver coil.

Fig. 3-7 displays the system overview of the new 8-channel pTx MRI system. The major advantage of the new system is its ability to deliver custom RF waveforms. The previous RF modulator is replaced by integrating two 4-channel software-defined radio modules. This enables complete arbitrary RF waveforms to be generated across the eight system channels, and with a dedicated computer console, system hardware control for safety monitoring features can be implemented, an expansion to the LabVIEW front panel in Fig. 2-3.

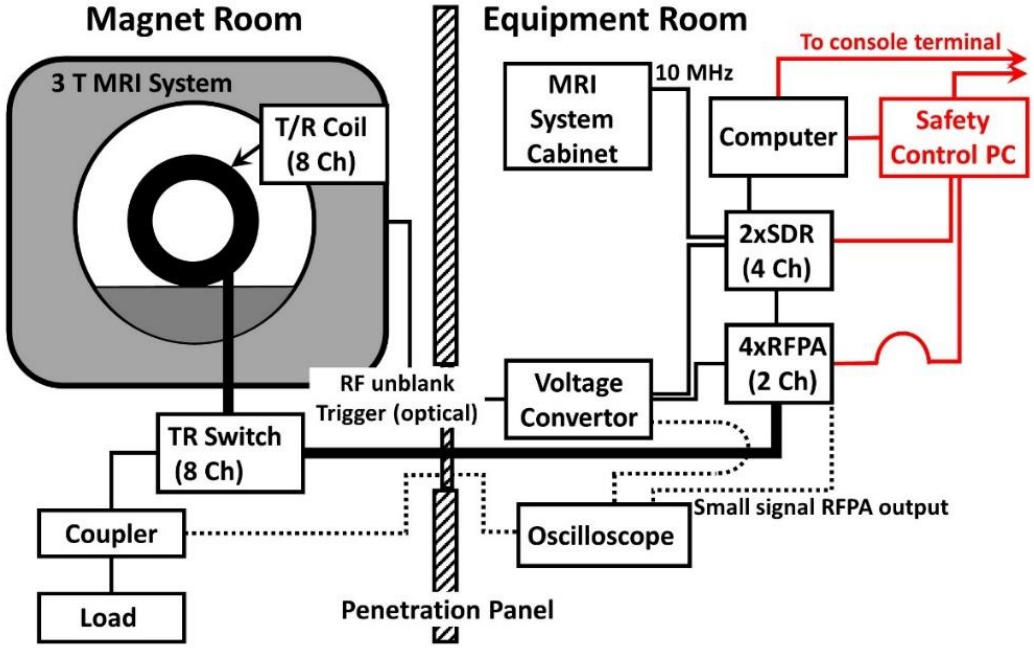

Fig. 3-7: System overview of the new parallel radiofrequency transmission system with software-defined ratio technology for arbitrary waveform generation [83]. Solid line connections are mandatory for regular pTx MRI system operation and configuring. Dashed lines are optional for system characterization and testing. TR = transmit and receive; SDR = software-defined ratio; RFPA = radiofrequency power amplifier; PC = personal computer.

3.3.1 8-channel pTx MRI Coil

The MRI RF coil (or antenna) is governed by electromagnetic principles, in particular Maxwell's equation with MRI operation in the near-field radiation zone of the coil. Its main purpose is to transmit and receive radiated energy into and from the human body. As presented in Chapter 2, the operating frequency revolves around resonance theory and the imaging nuclei of interest. Currently, phased array-based coil designs are popular amongst researchers and used clinically for anatomy-specific imaging. Typically, it is a collection of loop-style elements, sized and orientated near or on the anatomy of interest. This section describes the fabrication and presents the benchtop characterization results of the 8-channel pTx coil to be used with the new pTx system.

3.3.1.1 Design and Fabrication

For neuroimaging applications, it is common in MRI to use a dedicated transceiver birdcage coil. A birdcage coil configured for circular polarization mode can generate a superior homogeneous transmit RF magnetic field, a desirable imaging scenario that produces high-quality images. Fig. 3-8 (a) displays the internal coil design of a typical birdcage coil that consists of 2 circular rings and 16 rungs, and (b) is a photograph of a commercial MRI coil for clinical use.

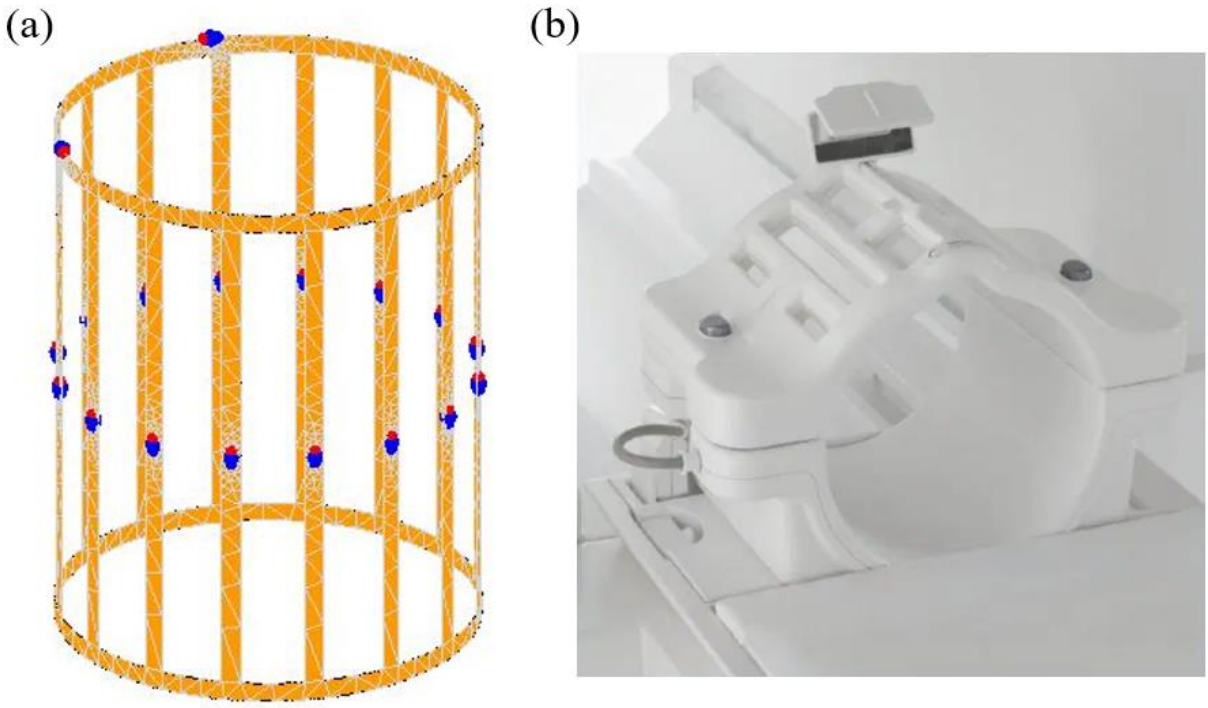

Fig. 3-8: (a) An electromagnetic simulation model of a typical birdcage coil consisting of 2 circular rings and 16 rungs and (b) a photograph of a commercial birdcage coil. (Photo from: https://www.siemens-healthineers.com/magnetic-resonance-imaging/options-and-upgrades/coils/tx-rx-cp-head-coil)

The 8-channel pTx transceiver coil follows a similar construction procedure as the 4-channel presented in Chapter 2. The main objective for this design was to maintain coil symmetry and the ability to produce an appropriate circular polarized-like field when driven with the appropriate amplitudes and phases. A transparent acrylic shell with an inner diameter of approximately 20 cm and a 0.6 cm wall thickness was used as the coil substrate. The half-inch-width copper tape was used to construct the phased-array design. Each array element has a width and length of approximately 9 and 15 cm, respectively, to fit and surround the entire inner diameter

of the acrylic shell. A small gap between each coil element was reserved for de-coupling capacitors to assist with coil channel isolation. Tune and match capacitors were spread around each array element to produce resonance at 123.25 MHz (the Lamour frequency of hydrogen on Siemens Healthineers MRI systems). Electromagnetic simulation calculated the appropriate capacitance for each array element. This process will be discussed in the next section. Soldering a coaxial cable completed the coil and provided the connection interface to the adaptor module. Essentially, each array element of the 4-channel pTx coil was halved to create the 8-channel design. Fig. 3-9 (a) displays the simulation model of the 8-channel pTx coil, and (b) is a photograph of the constructed 8-channel pTx coil.

This type of coil design is susceptible to the common-mode current flowing on the outer shield of the coaxial cable and is a major source of RF signal degradation. This is because the outer shield of the coaxial cable shares a common electrical signal ground with the phased-array element, causing unwanted current loss. RF baluns were integrated into each coaxial cable to suppress this effect, as shown in Fig. 3-9 (b). The RF baluns present a high impedance resonant circuit (at approximately 123 MHz), which suppresses the current flow along the outer shield of the coaxial cable and improves the overall efficiency of the coil.

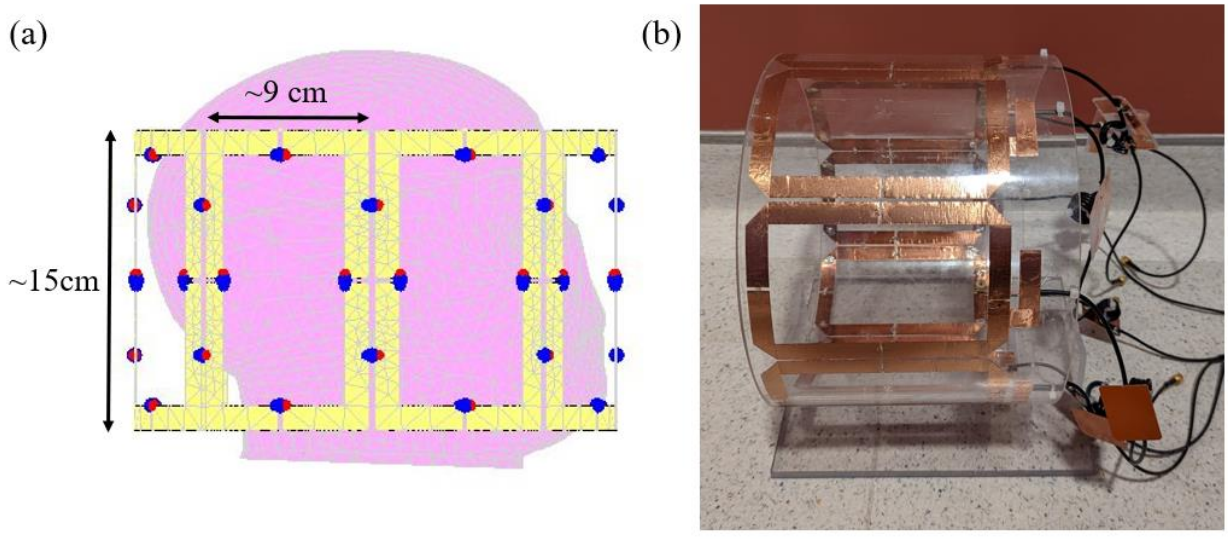

Fig. 3-9: (a) The electromagnetic simulation coil model with dimensions, as labelled and (b) a photograph of the constructed 8-channel parallel radiofrequency transmission coil with radiofrequency baluns.

3.3.1.2 Benchtop Characterization

Scattering (or s-) parameter measurements were taken to evaluate and optimize the performance of the pTx RF coil. S-parameter measurements are used to characterize the electrical behaviour of a linear electrical network matched to a characteristic impedance (e.g., 50 Ω in the standard case). The s-parameter measurements can provide electrical network properties such as gain, return loss, voltage standing wave ratio and reflection coefficient, which are essential system performance characteristics.

To verify and fine-tune the RF coil, as determined by simulation, s-parameter measurements were measured on a vector network analyzer (4395A, Keysight Technologies, Santa Rosa, CA, USA). The reflection coefficient (or S_{11}) is a measurement of signal loss due to reflection at the input of the RF coil and was recorded for each array element with the phantom loaded, as shown in Fig. 3-9 (a). The capacitance was adjusted iteratively to match the input coil impedance at 123.25 MHz (the Lamor frequency of hydrogen on Siemens MRI systems) to the characteristic impedance (e.g., the centre of the Smith chart, 50 Ω). Fig. 3-10 (b) displays a sample S_{11} measurement. The process was repeated for all eight coil elements until the performance benchmark of a minimum S_{11} magnitude of -12 dB (representing an approximate 90 % efficiency rate) was achieved. Because the coil elements are in very close proximity and are intended to be independent signal transmitters, isolation measurements (or S_{12}, a measurement of signal transmission from one coil element to another) were also required. If necessary, the de-coupling capacitances were adjusted until the performance benchmark of a minimum S_{12} magnitude of near -8 dB was achieved. The isolation measurements represent the respective next neighbour coil elements. Table 3-I summarizes the reflection coefficient, isolation and quality (or Q-) factor results for the 8-channel pTx coil. As presented in Chapter 2, the Q-factor is a key performance indicator that measures how well the resonant circuit is tuned to a desired frequency. In practice, it can be measured by a vector network analyzer as the ratio of the frequency of interest to the bandwidth frequency between the 3 dB points. For example, in Fig. 3-10, marker 0 is set to the frequency of interest (or 123.25 MHz) and markers 2 and 3 are set to the two 3 dB points from this reference frequency. It can be observed that the higher the Q-factor, the lower the 3 dB bandwidth will be and the sharper and steeper the dip will be. Although this may be desirable in subject-specific studies, it is not as suitable for clinical applications as patient sizes vary and will cause the

peak resonance frequency to shift. Therefore, a reasonably wide bandwidth or lower Q-factor is more suitable for this purpose.

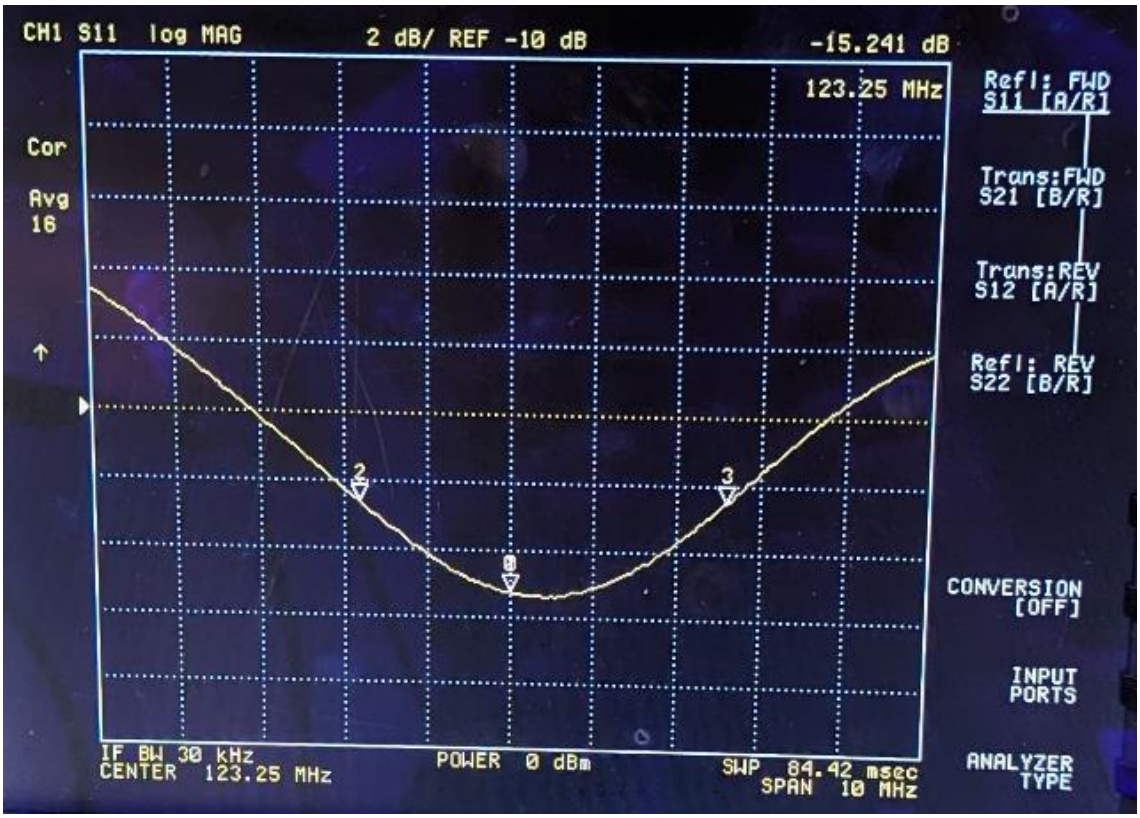

Fig. 3-10: A sample S_{11} measurement of the 8-channel parallel radiofrequency coil with markers set for a quality factor calculation.

Table 3-I S-parameter Measurement Results from the 8-channel pTx coil

System Channel	Reflection Coefficient (dB)	Isolation (dB)	Q-factor
1	-13.3	-7.8	22
2	-12.0	-8.2	18
3	-12.7	-7.9	21
4	-13.7	-8.4	22
5	-12.4	-8.5	20
6	-15.7	-9.1	27
7	-15.7	-9.0	28
8	-12.2	-8.1	18

3.3.2 Discussion and Conclusion

The custom RF coil was fabricated, characterized, and is ready for MRI testing. Fabrication of the 8-channel pTx coil presented several minor challenges. Channel-to-channel coupling between coil elements limited the achievable quality factor and reflection coefficient compared to the 4-channel coil. Using capacitors to reduce coupling effects was effective but only helped resolve the next neighbour effects and not the coupling effects from other coil elements, which were found to have some impact on the sensitivity of the coil element under test. Furthermore, with the phantom loaded, the implanted copper wire also contributed to the level of RF coupling experienced, particularly the nearest coil elements. As a result, the performance benchmarks for the 8-channel pTx coil were lower than what was achieved with the 4-channel version used in this thesis. However, the impact on image quality remains unknown and additional adjustments can be made according to future imaging results.

In general, B_1 homogeneity is expected to improve with 8-channel capabilities and should translate to improved image quality. As demonstrated in electromagnetic simulations, DBS patient safety benefits may also be achievable on an 8-channel pTx MRI system. While the results presented thus far are promising, the pTx safe mode relies on a fixed subject in space, but in a clinical setting, this is difficult to achieve as patient motion is a significant concern in MRI. Chapter 4 studies the effects of patient positioning and motion in proof-of-concept for 4-channel safe mode pTx MRI.

Chapter 4

Patient Motion, MRI Pulse Sequence Parameters and DBS Implant Heating

This chapter reviews the topic of patient motion in MRI, the challenge of imaging DBS patients, and its impact on image reconstruction. DBS patient motion is investigated by electromagnetic simulation with complimentary MRI experiments to assess its impact on 4-channel safe mode pTx MRI. The methods and results are presented, and the section concludes with a discussion on the effects of common head movements associated with DBS patients with motor-related disorders on localized RF heating effects along implanted DBS devices. Thus far, in this thesis, the RF heating experiments have mainly focused on high-heating scenarios and have not included many studies on routine MRI in a clinical setting. This chapter concludes with 4-channel safe mode pTx MRI experiments studying the effects of changes to prominent imaging parameters affecting SAR for more clinically relevant imaging protocols. The temperature and reconstructed phantom results are presented and compared to standard birdcage imaging. A part of the work contained in this chapter has been published in,

- B. Yang, C.-H. Chen, and S. J. Graham, "RF heating dependence of head model positioning using 4-channel parallel transmission MRI and a deep brain stimulation construct," *IEEE Letters on Electromagnetic Compatibility Practice and Applications*, vol. 4, no. 3, pp. 83-87, 2022. Doi: 10.1109/LEMCPA.2022.3180974

4.1 MRI Patient Motion and Image Reconstruction

MRI is a powerful diagnostic tool for disease detection as well as for studying human body function. However, since clinical adoption, image artifacts have reduced the quality of reconstructed images and the ability of clinicians to identify anatomical features for treatment decision-making precisely. MRI systems are complex, and imaging can often lead to patient discomfort. Typical bore sizes are small and can cause patient anxiety and claustrophobia as scan times average between 30 to 40 minutes. Furthermore, the loudness of MRI systems during

imaging can reach up to 130 decibels, causing noise discomfort and, consequently, leading to frequent patient motion during imaging.

Patient motion is a major challenge in MRI, and while most young, healthy adults are capable of controlling head and body motion, it remains a difficult task for children and patients with certain impairments. In many situations, pillows, pads, and earplugs often help but cannot resolve the more severe cases. For example, patients suffering involuntary body movements and/or cognitive impairments caused by Parkinson's disease. As a result, imaging DBS patients can be challenging. Fig. 4-1 highlights some of the typical motor symptoms associated with Parkinson's disease, many of which DBS treatment can improve. DBS patients experience a wide range of motion that is rhythmic and oscillatory, with amplitudes ranging from a few millimeters to tens of centimeters [84]. In addition, it is a common practice for hospitals and clinics to request DBS patients to reframe from taking medications and shut down DBS devices prior to MRI as a safety precaution, leaving DBS patients without symptom relief during imaging [85, 86].

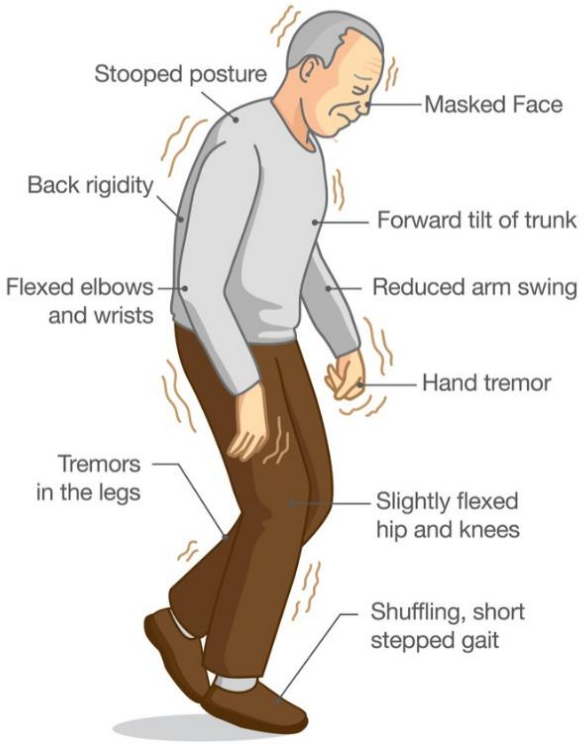

Fig. 4-1: Summary of motor-related symptoms associated with Parkinson's disease. (Photo from: https://wiki.mcmaster.ca/LIFESCI_4M03/group_3_presentation_1_-_parkinsons)

Patient motion creates an issue in MRI because of how image data is acquired. Gradients are used for spatial encoding of the received MRI signal; this process is slow and sequential. When the raw data is acquired, it resides in the Fourier domain or commonly known as "k-space" in MRI. It is a data matrix containing the spatial frequency information of the object being imaged. Each point in k-space represents a specific frequency, phase, and intensity. The centre of k-space consists of the low spatial frequency data that contains most of the general features of the object being imaged, and moving outward from the centre contains the higher spatial frequency data, contributing to finer features of the reconstructed object. Fig. 4-2 displays an example k-space data grid and the contribution of low and high spatial data on image reconstruction of a human brain. As shown in the figure, the majority of the image data resides at the centre of the k-space.

Populating k-space is a sequential process requiring multiple RF excitation cycles. For example, Fig. 4-3 illustrates a basic spin-echo pulse sequence, a fundamental protocol commonly used in MRI. As shown in the figure, the acquired data translates into a line in k-space for each RF excitation sequence. As a result, filling k-space to reconstruct high-quality images takes several iterations, leading to long scan times.

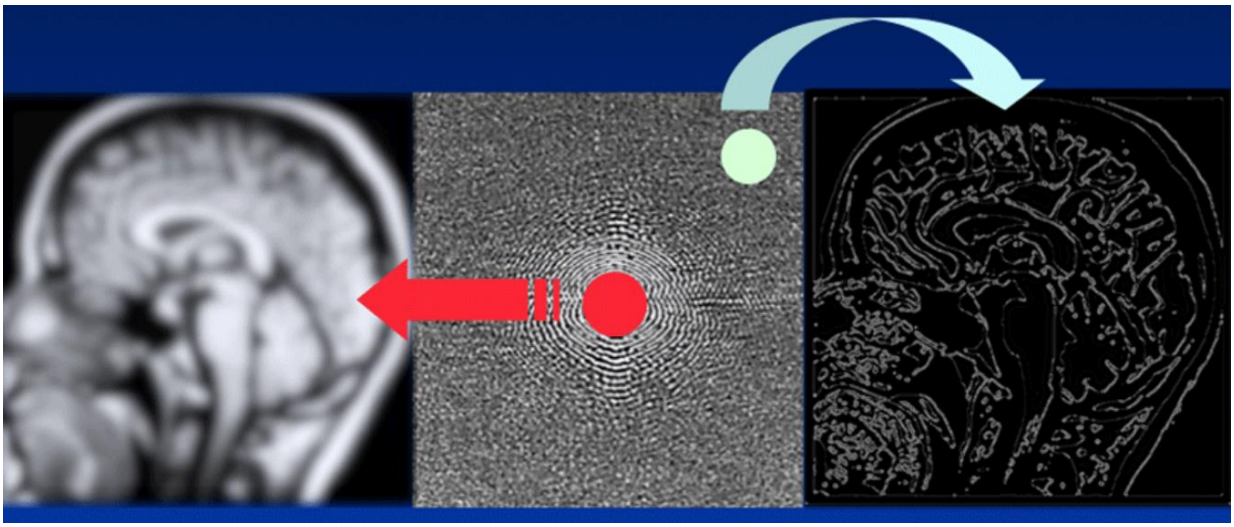

Fig. 4-2: Example k-space data organization and image contribution to a human brain. (Photo from: https://mriquestions.com/locations-in-k-space.html)

The problem associated with patient motion during scanning is with data translation in k-space. In Fig. 4-3, each RF sequence represents a single line in k-space (the yellow and orange lines). If subsequent patient motion occurs (i.e., a head tilt), it translates into phase misalignment

in k-space, as shown in Fig. 4-4 inset by the green line. The result is image distortion (i.e., blurring or ringing artifact) in the final reconstructed image. Fig. 4-4 illustrates the resultant effect of patient head motion on an MRI image of the human brain.

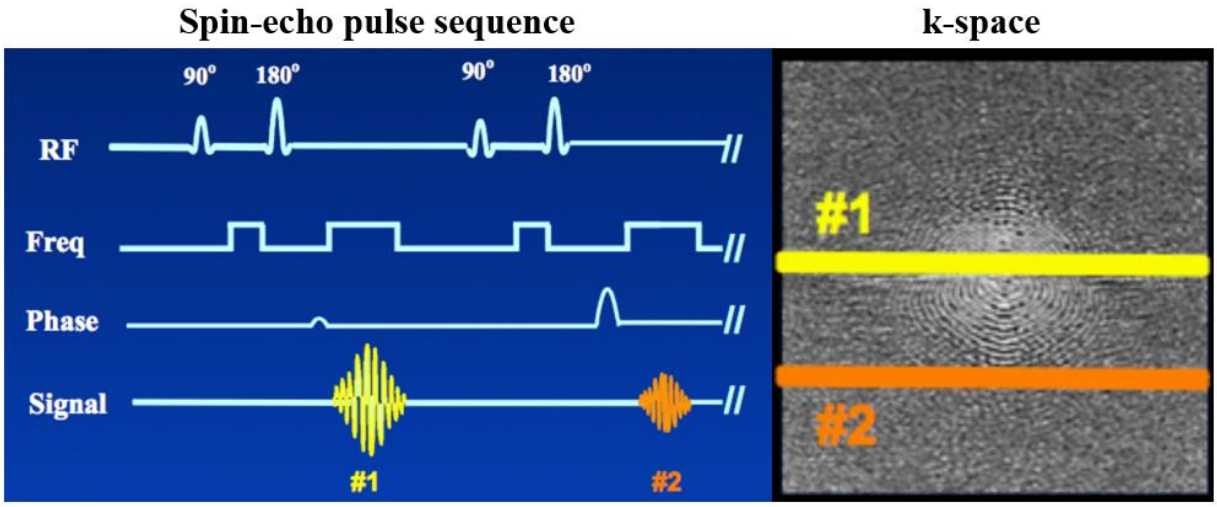

Fig. 4-3: Basic spin-echo pulse sequence diagram and corresponding k-space data representation. (Photo from: https://mriquestions.com/what-is-fsetse.html)

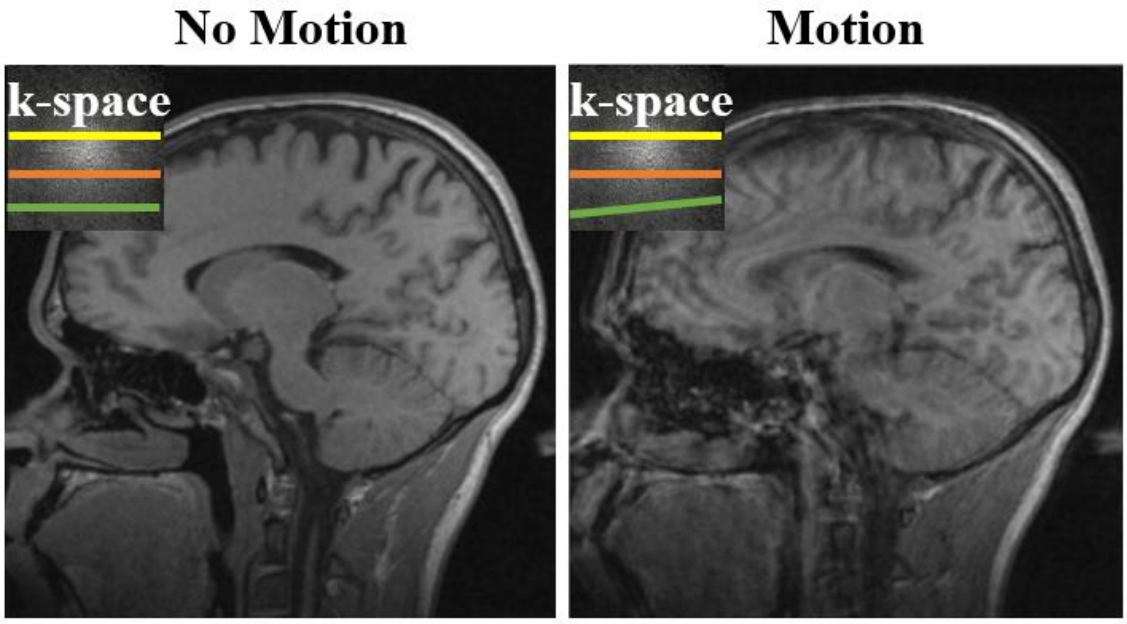

Fig. 4-4: Sample reconstructed MRI image illustrating the effect of patient motion on k-space translation and overall image quality [87].

Patient motion has a similar effect on the proposed pTx MRI safe mode presented in this thesis. The safe mode technique derives the safe mode pTx input parameters (i.e., the amplitudes and phases) based on a fixed position in space. Thus, patient motion during safe mode imaging will disrupt the initial electromagnetic distribution required for pTx MRI safe mode generation. Because DBS patients often suffer from movement disorders, unsafe imaging conditions may arise during safe mode pTx MRI and its effect should be studied. The proceeding sections will discuss the importance of this topic and the effect of typical DBS patient motion on 4-channel safe mode pTx MRI in proof-of-concept. The study is then expanded to include the implications of changing prominent scan parameters for more routine clinical imaging protocols.

4.2 MRI of DBS Patient Motion

DBS is a well-established treatment option to improve the quality of life for those with neurological disorders, with over 150,000 patients worldwide estimated to have opted for this treatment - a number that promises to grow substantially [88]. MRI is an indispensable tool in widespread radiological applications, and there is a strong need to provide MRI exams for DBS patients both before and after device implantation. However, DBS patients who undergo MRI are potentially at risk of electrical charge accumulation along the DBS device during RF excitation, which has the potential to cause heating and tissue injury. Due to this safety concern, regulatory bodies have placed strict limitations on how MRI exams can be performed on patients with implanted DBS devices. Presently, the Medtronic Percept DBS system is the only regulatory-approved neurostimulator with MRI-conditional labeling that allows for limited 1.5 and 3 T full-body MRI [88, 89]. Research sites continue cautiously exploring "off-label" imaging with these and older MRI-conditional DBS systems [90, 91], attempting to improve the image quality and image capabilities for this patient population.

As the impetus grows to examine DBS patients using 3 T MRI (and potentially using ultra-high field systems operating at 7 T and above), additional strategies are required to ensure patient safety. Although new implant lead designs are being developed specifically to offer greater RF coupling protection [92], one important general MRI method to consider in this context is known as parallel RF transmission or pTx, which provides additional flexibility and control by generating an RF excitation that is the combined effect from multiple carefully driven transmitters. Several different methods have been proposed in the literature using electromagnetic simulation or

specialized transmit-receive coils that determine implant-friendly "safe modes". For example, McElcheran *et al*. [93] developed a pTx RF shimming optimization method to create a safe mode of imaging that shows potential in suppressing RF heating in targeted regions of implanted wires at 3 T, which is implemented in this work. The pTx safe mode relies on accurate DBS lead spatial coordinates (with respect to the MRI system) to produce a specific electromagnetic condition. In practice, mispositioning caused by patient setup and/or patient motion could have a negative impact on the simulation-derived pTx safe mode. Furthermore, present MRI guidelines recommend that implanted DBS devices are powered off prior to imaging [94], which could lead to increased motion effects in DBS patients with movement disorders (i.e., Parkinson's disease). This chapter section investigates the sensitivity of the pTx safe mode to phantom misposition and motion in a proof-of-concept, using electromagnetic and thermal simulations as well as complementary MRI experiments using the novel 4-channel pTx research platform presented in Chapter 2 [95].

4.2.1 Safe Mode pTx MRI and DBS Implant Heating

The safe mode is generated by an RF shimming optimization procedure that determines the optimal amplitude and phase weightings to each coil array element (or pTx channel) to suppress RF heating effects. More specifically, the amplitudes A_n and phases φ_n of the common RF input signal are adjusted for each pTx channel to achieve a minimized electric field strength at the tip of the implanted wire (creating an implant-friendly "safe mode" of RF excitation). A trade-off cost function concurrently minimizes (a) the RF power deposition in a fixed, targeted region of minimization (ROM) surrounding the lead tip, which contains the exposed DBS electrodes, and (b) inhomogeneity of the B_1^+ field within a volume of interest (VOI), as given by:

$$min_{A_n,\varphi_n}\left[\left(\frac{\sigma_{VOI}(|B_{1,tot}^{+}|)}{\mu_{VOI}(|B_{1,tot}^{+}|)}\right)+\lambda\cdot\mu_{ROM}\left(\frac{(|E_{tot}|^2)}{(|E_{quad}|^2)}\right)\right], \tag{4-1}$$

where $\sigma_{VOI}()$ is the standard deviation of the total B_1^+-field over the VOI; $\mu_{VOI}()$ is the mean of the total B_1^+-field over the VOI; $B_1^+{}_{tot}$ is the net excitation magnetic-field produced by all coil elements; λ is a weighting factor; E_{quad} is the electric field in the pTx quadrature (quad) mode (i.e., $A_n = 1$ and $\varphi_n = ((\pi(n\text{-}1))/2))$, a circularly-polarized field; and $\mu_{ROM}()$ is the mean of the ratio of total electric field E_{tot} and E_{quad} over the ROM [93].

4.2.2 Simulation and Experimental Methods

To evaluate the sensitivity of pTx safe mode to phantom misposition and motion, we conducted a series of electromagnetic and thermal simulations in FEKO (Altair Engineering Inc., Troy, USA) for different phantom configurations, along with MRI experiments on a custom 4-channel pTx research platform built onto an existing 3 T MRI system (Magnetom Prisma, Siemens Healthineers, Erlangen, DEU) [95]. The inset in Fig. 4-5 (a) shows the 4-channel transceiver coil and homogeneous head-shaped phantom with an implanted insulated copper wire oriented in a patient-derived DBS lead trajectory (as specified in Chapter 2) used in the electromagnetic simulation. Figs. 4-5 (b) and (c) show the head rotation range studied in the roll and yaw directions according to the coordinate system shown in Fig. 4-2. Penne's bioheat equation, simplified by removing the metabolic and perfusion effects, was utilized to predict the temperature elevations and evaluate RF heating [96].

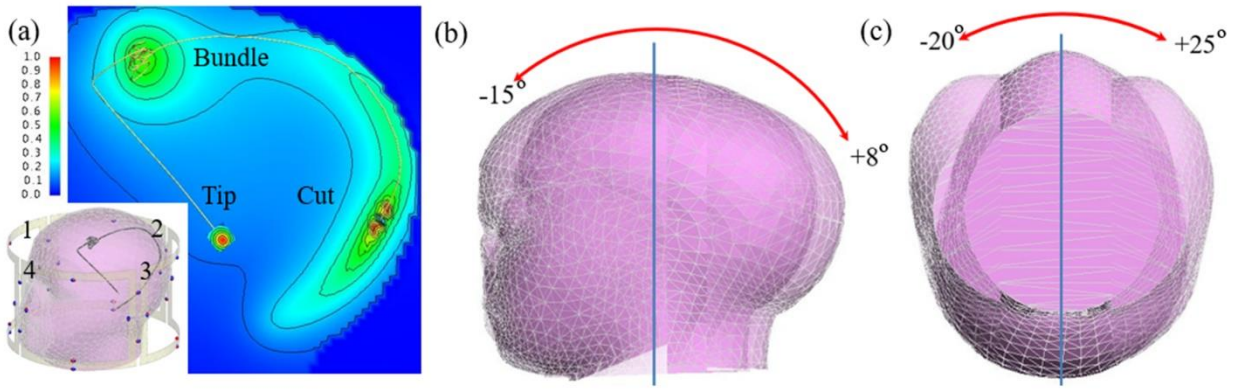

Fig. 4-5. (a) Electromagnetic simulation model of the 4-channel transceiver coil and head-shaped phantom (inset). Preliminary normalized electric field results along the implanted wire trajectory (Tip = wire tip, Bundle = excess wire bundle, and Cut = wire end region); (b) head rotation range studied along the x-axis (roll); and (c) head rotation range studied along the z-axis (yaw).

The electromagnetic and thermal simulations were first executed to verify that pTx safe mode efficacy remained consistent with previous studies [93, 95]. The actual channel-specific pTx inputs (amplitude/phase) used to generate 4-channel pTx safe mode in the experiment after full system calibration were: channel 1, -4.0 dB / 251.0°; channel 2, -1.9 dB / 0°; channel 3, 0 dB / 126.6°; and channel 4, -1.3 dB / 112.2°. In the electromagnetic simulation, the input RF voltage for the 4-channel pTx safe mode was then scaled to approximate the RF voltage delivered to the 4-channel RF coil in the experiment [95]. An RF magnetic field (i.e., B_1^+) homogeneity

comparison was then conducted between 4-channel pTx safe mode and quad mode over the whole head volume to assess the trade-off in generating pTx safe mode according to (4-1). This involved scaling the pTx safe mode B_1^+ data to a mean value equal to that of the pTx quad mode (i.e., equating the average flip angles). The standard deviations were then calculated for comparison.

Subsequent simulations encompassed a series of phantom rotations that assessed the robustness of the 4-channel pTx safe mode to patient misposition (or setup errors). The specific phantom rotations studied mimicked typical DBS patient head motion amplitudes (i.e., head tremor amplitude = 2 – 3 cm) that enabled preliminary evaluation of DBS patient motion effects. For verification, a 4-channel pTx MRI safe mode experiment was conducted using a phantom structure with DBS lead geometry that reasonably approximated the simulated model. A pulse sequence that was shown in previous studies to produce high RF power deposition (Turbo spin-echo, TSE: repetition time (TR) = 516 ms, echo time (TE) = 6.7 ms, flip angle = 150°, and duration = 3:45 mins) was used. The phantom was placed according to the positions and rotations listed in Fig. 4-6 [97]. Each position or rotation represented the maximum displacement available (from the reference position) within the RF transceiver coil used. The temperature change was recorded at the wire tip throughout by a fiber-optic probe (OTG-MPK5, Opsens Inc., Quebec City, QC; ±0.3°C accuracy).

4.2.3 Simulation and Experimental Results

Fig. 4-5 (a) shows normalized electromagnetic simulation results and highlights three elevated electric field zones: the wire tip, excess wire bundle, and near the wire end (labeled as the tip, bundle, and cut), respectively. The wire tip had the highest electric field strength and presented the greatest local specific absorption rate (SAR) risk. As expected, thermal simulations for 4-channel pTx safe mode showed negligible heating in all three zones, resulting in temperature elevations that were consistent with previous studies in the lab and that were below current MRI guidelines (approximately +1.0°C bodily temperature increase) [93, 95]. An approximate 60% reduction in B_1^+ homogeneity was shown over the whole head volume for 4-channel pTx safe mode when compared to 4-channel pTx quad mode, such that flip angle variance was reasonably traded for MRI safety.

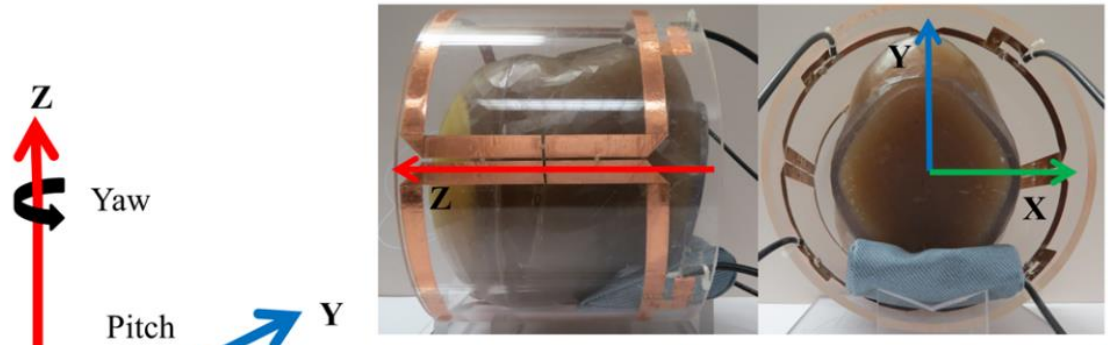

Motion plane	Shift from reference
X-direction	-3.5 ± 0.2 , 3.5 ± 0.2 cm
Y-direction	1.5 ± 0.2 cm
Z-direction (B_0)	-1.3 ± 0.2 cm
Yaw	-20 ± 5º , 25 ± 5º
Roll	-15 ± 5º , 8 ± 5º
Pitch	-50 ± 5º , 40 ± 5º

Fig. 4-6. Four-channel parallel radiofrequency transmission (pTx) transceiver coil and head phantom, and tabulated list of positional and rotational shifts of the phantom from the reference position, used for the mispositioning experiments with pTx safe mode [97].

Fig. 4-7 plots the simulated temperature elevations in safe mode for rotation values outlined in Fig. 4-5 (b) and (c), which depict typical extents of DBS patient head motion. The head rotations resulted in minor temperature increases of approximately 0, 0.2, 0.2 and 0.3 °C at the wire tip that remained below the present safety limits. Table 4-I summarizes the MRI experiment results for the phantom misposition parameters studied, as outlined in Fig. 4-6. Good agreement was observed between simulation and experiment with the corresponding measured temperatures of 0.2, 0, 0.5 and 0.2 ± 0.3 °C, respectively. The 4-channel pTx TSE imaging in safe mode at the reference position was able to suppress RF heating effects by over 90%. The phantom mispositioning experiment showed encouraging results, as the ten tested safe mode imaging scenarios recorded temperature elevations under the current imaging safety limits (Table 4-I). This validated the observed behavior in simulation and provided further evidence of the benefits of 4-channel pTx MRI and the proposed safe mode method for addressing DBS patient safety concerns.

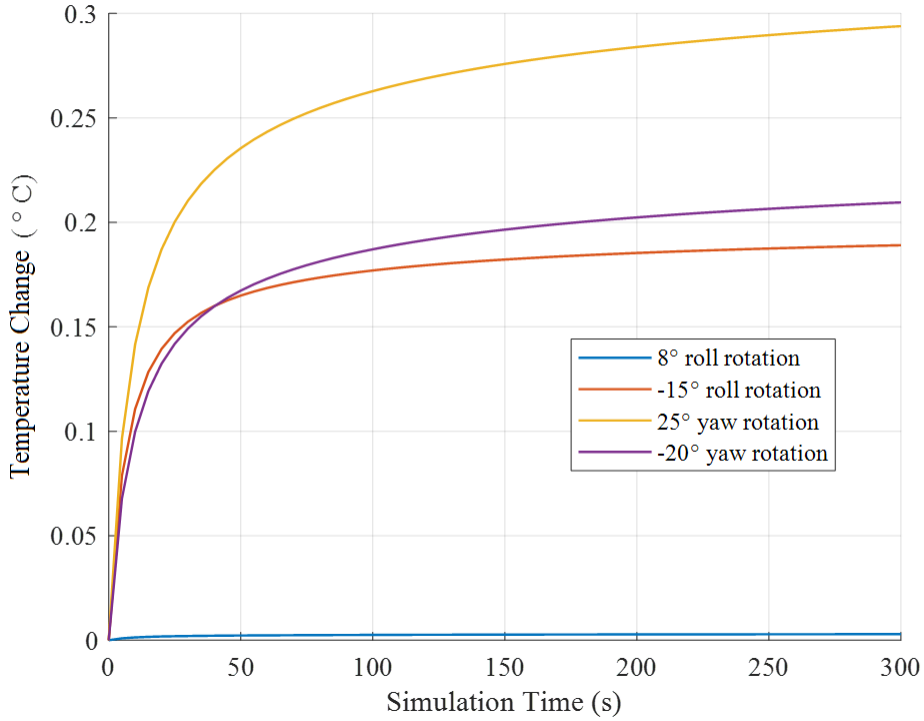

Fig. 4-7. Simulated temperature rise at the wire tip in 4-channel parallel radiofrequency transmission safe mode for head rotations set out in Fig. 4-5 (b) and (c). Typical deep brain stimulation patient head movements were observed to have some impact on overall temperature change, but all tested scenarios remained below current imaging guidelines.

Table 4-I: RF heating results from mispositioning of the phantom in different pTx MRI modes, positions, and rotations

pTx mode	Initial Temp. (ºC)	Final Temp. (ºC)	Change (ºC)
Quadrature Mode	23.0	25.6	2.6
Safe Mode	23.1	23.3	0.2
X-direction:(-3.5cm)	23.2	23.5	0.3
X-direction: (3.5cm)	23.2	23.5	0.3
Y-direction:(1.5cm)	23.0	23.3	0.3
Z-direction:(-1.3cm)	23.3	23.6	0.3
Yaw: (-20º)	23.2	23.7	0.5
Yaw: (25º)	23.2	23.4	0.2
Roll: (-15º)	23.1	23.1	0
Roll: (8º)	23.2	23.4	0.2
Pitch: (-50º)	23.2	24.0	0.8
Pitch: (40º)	23.2	23.3	0.1

4.2.4 Discussion and Conclusion

The safe mode of 4-channel pTx has undergone initial evaluations for MRI at 3 T [93, 95]. With the intent to image DBS patients in the future using the available pTx platform [95], patient setup errors and motion effects require investigation. The present work thus evaluated the potential impact of phantom misposition in experiments and simulations to assess patient motion effects in proof-of-concept. Overall, the results suggested that the pTx safe mode method was robust to a wide range of head movements, including those commonly observed in DBS patients.

Several aspects of this work merit discussion. First, the results support the use of pTx technology to improve MRI safety at 3 T - particularly by reducing the RF heating risks associated with imaging DBS patients. As expected and consistent with previous work [93, 95], the results from the 4-channel pTx safe mode strongly suppressed the localized RF heating effects along the wire trajectory for the prescribed configuration when compared to the 4-channel quad mode. At the same time, B_1^+ homogeneity over the whole head volume was reduced by approximately 60% when compared to the 4-channel pTx quad mode. This latter result is not surprising as quad mode maximizes constructive interference between pTx channels, whereas safe mode is an optimized balance between electric field minimization and B_1^+ homogeneity. There are several options to improve on the present result. Although the weighting factor, λ in (4-1), can be adjusted to prioritize B_1^+ homogeneity, this may have an impact on patient safety in a patient-specific manner. Alternatively, pTx MRI has enabled specialized techniques, such as reduced field of view (r-FOV) imaging, which utilizes optimized RF signals to excite a targeted region of interest. For example, with pTx and r-FOV, prioritized brain regions (i.e., the DBS lead tip and trajectory in the brain) can likely be better visualized, mitigating some of the B_1^+ homogeneity concerns [98, 99]. Increasing the pTx system channel count is also possible to improve B_1^+ homogeneity. Detailed investigations of both options would be very useful in the future.

Second, the simulations supported that the 4-channel pTx safe mode remained robust to mispositioning. However, different (albeit small) temperature rises were observed (Fig. 4-7). These differences likely arose from the movement of the wire tip into different electric field zones within the ROM. Further simulations would be useful to explore the interaction between motion sensitivity and ROM size - and how such effects influence B_1^+ homogeneity.

Third, although the experimental and simulation results show quite robust tolerance to mispositioning with 4-channel pTx, one experimental manipulation - a significant pitch rotation - led to a temperature increase of 0.8 ± 0.3°C (Table 4-I). By extension, it is important to emphasize that the present experiments are not exhaustive. Certain motion or mispositioning conditions in DBS applications may still pose some safety risk of exceeding the +1.0°C patient safety threshold using the current pTx methods. Nevertheless, it is speculated that improvement on the possible worst-case scenarios will be possible - thus providing additional risk reduction – either by using higher system channel counts or more sophisticated RF pulse designs or by combining these two approaches. As undertaken here, such pTx work should be undertaken with carefully selected experimental conditions that can be supported and validated by numerical simulations. Supplementary simulations can then be employed for full exploration of the complex parameter space.

Limitations of the study also require discussion. First, some mismatch between simulation and experiment was inevitable and was observed. Multiple factors are likely responsible for the discrepancy. The simulation results were based on continuous-wave excitation, whereas the MRI used pulsed-wave excitation; this was expected only to produce minor discrepancy, as the turbo spin-echo pulse sequence used short echo-spacing for maximum SAR. The MRI experiments were conducted on a custom pTx research platform that bypassed the safety procedures on the existing MRI system; thus, the simulation parameters used in Fig. 4-7 were only an approximation of the actual pTx setup – as reasonable for proof-of-concept. Due to instrumental error and coil loading effects, the pTx platform also required careful calibration to resolve channel-to-channel variation. The calibration considerably reduced the impact of these effects on pTx safe mode but likely did not eliminate them entirely. In addition, the DBS lead trajectory and positioning within the phantom was the best attempt to match the simulation model (a patient-derived geometry from a computed tomography image). These system uncertainties and phantom differences likely were the dominant sources of mismatch error. Taken with the present results, however, these practical limitations suggest the robustness of the 4-channel pTx safe mode to small RF amplitude/phase error.

Second, the experimental results, although promising, were limited to static phantom displacements and thus did not fully capture real-world behavior. Patient motion is much more

fluid and complex than portrayed in this study. In particular, tremor is anticipated in DBS patients with Parkinson's disease, as powering off DBS devices is the current practice at our institution [90]. It is reasonable to suggest that such oscillatory motion would result in time-averaged heating effects in safe mode that are even less than those presented here.

Lastly, although the phantom used in the present study is consistent with MRI safety literature, it is a simplistic representation of human head anatomy [91]. The use of an anthropomorphic heterogeneous phantom may prove beneficial in a future study, as significant differences in RF heating effects for homogeneous and heterogeneous phantoms have been reported [100].

In conclusion, the present work suggests the robustness of pTx safe mode to patient mispositioning and motion, although the work remains preliminary and cannot be considered entirely conclusive. For example, it is common for DBS patients to receive bilateral implants, and the management of excess lead length varies across the patient population. The results presented in this work represent just one of the many possible DBS lead trajectories and do not consider the bilateral implant scenario. A recent study reported inadvertent brain stimulation during MRI of DBS patients, which may cause unpredictable patient behavior [90]. Nonetheless, pTx MRI remains a strong option to address DBS patient safety concerns at 3 T.

4.3 Effects of RF Pulse Sequence Parameters on DBS Implant Heating

MRI is a powerful imaging modality and is routinely used in clinics for diagnostic imaging of neurological diseases. Human brain images are reconstructed with excellent soft tissue contrast and resolution capable of capturing anatomical features deep within brain structures. MRI systems are complex and consist of several hardware components, which are programmed, controlled and timed to create a specific electromagnetic condition for imaging. In MRI, this process is known as a pulse sequence. Commercial MRI systems are equipped with a library of pre-programmed pulse sequences with several imaging parameters available that are modifiable by the MRI technologist. For example, the image orientation, pixel size and slice thickness. However, in terms of DBS patient safety, the effect of more prominent pulse sequence parameters affecting RF power is of greater interest and is the topic of study in this section. Phantom MRI experiments are performed

on our 4-channel pTx MRI system and were compared with standard birdcage imaging when varying two prominent routine RF pulse sequence parameters to study its effects on the proposed safe mode technique. This is followed by a simple and straightforward image quality comparison of the reconstructed phantom for both setups.

4.3.1 Background

The specific absorption rate or SAR is the primary safety measure used in MRI and is commonly expressed based on the magnitude of an electric field [101],

$$SAR_{\Delta v}(t) = \int \frac{\sigma(r)|E(r,t)|^2}{\rho(r)} dv, \tag{4-2}$$

where r is the position, σ is the conductivity of tissue, ρ is the mass density, $E(r,t)$ is the total electric field vector at position r as a function of time, dv is the differential volume element, and Δv is the volume over which the integral is calculated, as described in Chapter 1. However, it can also be expressed as [101],

$$SAR = \frac{\sigma A^2 \omega^2 B_1^2 D}{2\rho}, \tag{4-3}$$

where σ is the conductivity of tissue, A is the cross-sectional area, ω is the Lamor frequency, B_1 is the RF magnetic field (the mean amplitude of the RF-pulse), D is the duty cycle, the percent time in an RF pulse sequence, and ρ is the mass density. Thus, according to equation (4-3), several operator-defined variables can affect SAR, more specifically, for turbo spin-echo, or TSE imaging, that delivers successive RF pulses to refocus spins for improved signal quality, the selected refocusing flip angle of these additional pulses will affect the RF pulse amplitude or B_1. Furthermore, increasing the number of slices (or the number of RF pulses transmitted) will affect the overall duty cycle or D.

Overall, image quality is dependent on the signal-to-noise ratio, or SNR. There are several methods to estimate the SNR from a reconstructed image. This work uses the single acquisition method to compare image quality. The method involves a standard MRI image (with the magnitude of the MRI signal represented at each volume element or voxel). By this approach, the SNR is calculated by [102],

$$SNR = 0.655 \cdot \frac{\text{signal amplitude}}{SD}, \tag{4-4}$$

where *SD* is the standard deviation of the noise and applies a correction factor that compensates for the change in the statistical noise distribution when reporting the MR signal magnitude (rather than the real and imaginary components). This method is applied to determine the voxel-wise SNR maps (see Fig. 4-10) by using the signal intensity at each voxel and defining *SD* as a region of interest within the image background.

4.3.2 Experimental Method

To investigate the implications of pulse sequence parameters on DBS patient safety and our proposed safe mode technique, a series of MRI experiments using our 4-channel pTx system integrated onto a 3 T MRI system (Magnetom Prisma, Siemens Healthineers, Erlangen, DEU) were conducted changing the refocusing flip angle and the number of slices. During the spin relaxation process, the spins begin to de-phase, and at the refocusing flip angle, a separate RF pulse is sent (for standard spin-echo-based pulse sequences) to assist with phase re-alignment that improves the overall MRI signal. The larger the flip angle (up to 180º), the higher the RF amplitude required. The number of slices refers to the total number of images to be reconstructed within a particular imaging volume of interest. The greater number of slices, the greater number of RF pulses delivered. Both of these parameters directly relate to the RF power level delivered to a subject and are commonly recommended by the MRI system to lower the estimated SAR level when a defined pulse sequence fails the initial pre-scan SAR safety check.

To evaluate DBS patient safety, the same homogeneous head-shaped phantom with an implanted wire was used for a TSE sequence weighted for T2 imaging, the transverse relaxation time of the tissue. T2 imaging is commonly one of several routine anatomical brain imaging protocols used in clinics. This is achieved, typically, by setting the repetition time or TR, between 2000 – 6000 ms and echo time or TE, between 100 – 150 ms. Temperature elevations were recorded at the wire tip for 4-channel pTx MRI in safe mode using TSE imaging for different RF power depositions by varying the number of image slices (from 8 to 38) acquired at a large flip angle (TR / TE = 6000 ms / 103 ms, flip angle = 165º, duration = 1:38 mins) and by varying the flip angle (from 60º to 180º) at a fixed number of slices (TR / TE = 6000 ms / 103 ms, number of

slices = 28, duration = 1:38 mins). A total of ten experimental conditions were tested. For comparison, analogous imaging and temperature measurements were made for birdcage MRI. RF heating measurements were recorded using a fiber-optic temperature sensor (OTG-MPK5, Opsens Inc., Quebec City, QC) affixed to the wire tip. A separate fiber-optic temperature sensor was inserted near the top of the phantom to confirm temperature elevations were localized during 4-channel pTx and birdcage MRI and was measured to be at ambient temperature for the entire experimental study. SNR was then calculated based on equation (4-4) for a set of reconstructed images at similar slice locations to compare image quality between both setups.

4.3.3 Experimental Results

Fig. 4-8 displays the temperature change results for the 4-channel safe mode pTx MRI and birdcage MRI setups for a different number of slices. The measured temperature elevations for 8, 18, 28 and 38 slices during T2-TSE imaging were 0.1, 0.1, 0.1 and 0.2 ± 0.3 ºC for 4-channel safe mode pTx MRI and 0.3, 0.7, 1.2 and 1.7 ± 0.3 ºC for birdcage MRI, respectively. As expected, an increasing trend is observed with conventional birdcage imaging, while for 4-channel safe mode pTx MRI, negligible temperature changes were recorded. Similar results can also be observed for changes in another prominent MRI scan parameter, the flip angle for the same pulse sequence setup, with temperature results shown in Fig. 4-9. The measured temperature elevations for flip angles of 60º, 90º, 115º, 140º, 165º and 180º during T2-TSE imaging were 0.1, 0.1, 0.1, 0.1, 0.1 and 0.1 ± 0.3 ºC for 4-channel safe mode pTx MRI and 0.4, 0.5, 0.6, 0.7, 1.0 and 1.1 ± 0.3 ºC for birdcage MRI, respectively. Again, 4-channel safe mode pTx MRI results showed good resilience to increasing RF power conditions, while birdcage imaging showed increasing temperatures. Fig. 4-10 shows the SNR maps of the phantom at similar slice locations. The red dashed lines in Fig. 4-10 (a) approximated the field-of-view of the 4-channel pTx MRI coil. The phantom extended beyond the physical dimensions of the constructed phased array, and as expected, the affected regions near the top and bottom of the phantom experienced low signal strength.

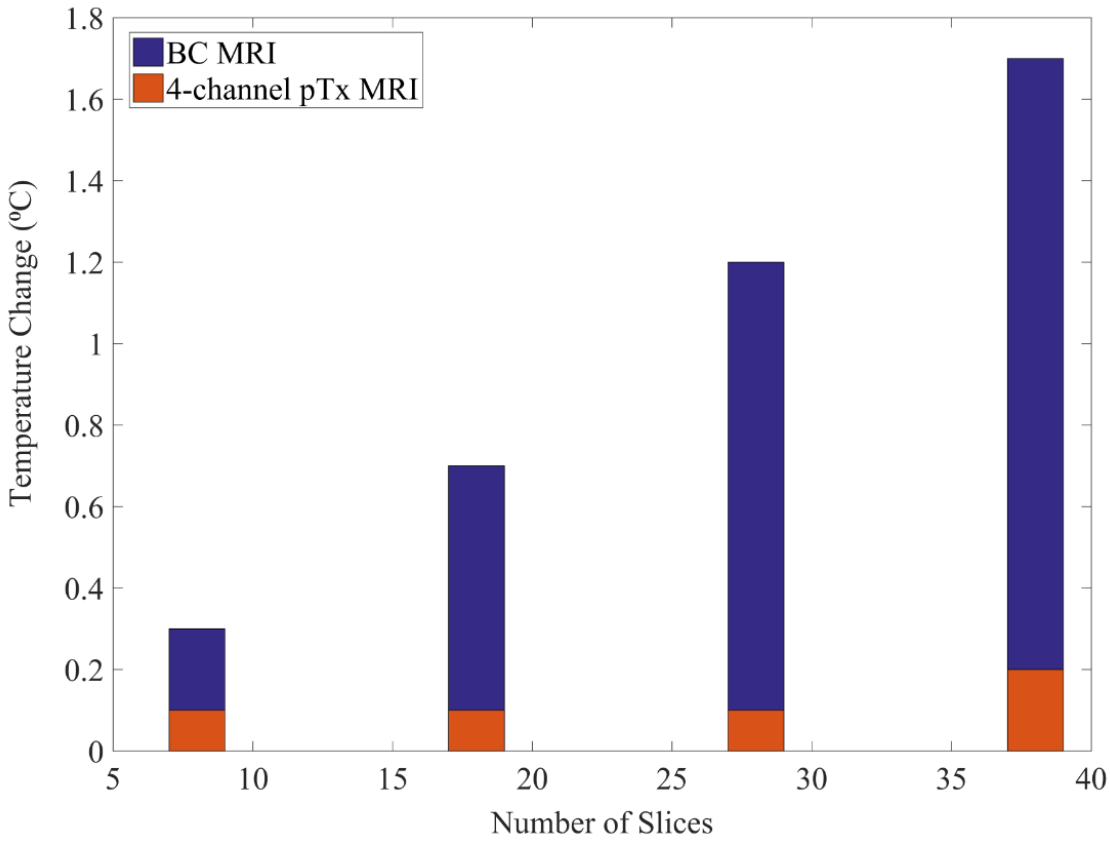

Fig. 4-8: Experimental temperature change results from 4-channel safe mode parallel radiofrequency transmission (pTx) magnetic resonance imaging (MRI) and the birdcage (BC) MRI for a transverse relaxation (T2) weighted turbo spin-echo pulse sequence (TR / TE = 6000 ms / 103 ms, number of slices = 28, duration = 1:38 mins) when varying the number of slices. The measured temperature elevations for 8, 18, 28 and 38 slices during T2-TSE imaging were 0.1, 0.1, 0.1 and 0.2 ± 0.3 ºC for 4-channel safe mode pTx MRI and 0.3, 0.7, 1.2 and 1.7 ± 0.3 ºC for birdcage MRI, respectively. TR = repetition time; TE = echo time.

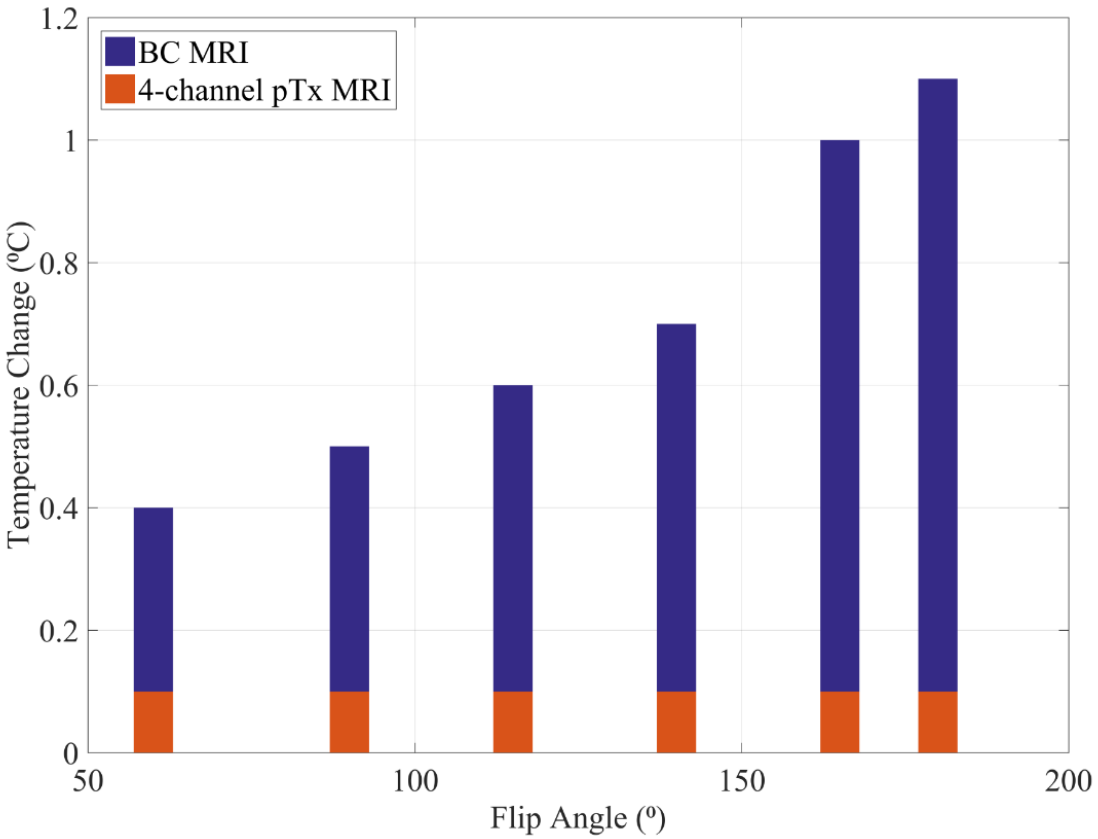

Fig. 4-9: Experimental temperature change results from 4-channel safe mode parallel radiofrequency transmission (pTx) magnetic resonance imaging (MRI) and the birdcage (BC) MRI for a transverse relaxation (T2) weighted turbo spin-echo pulse sequence (TR / TE = 6000 ms / 103 ms, number of slices = 28, duration = 1:38 mins) when varying flip angle. The measured temperature elevations for flip angles of 60º, 90º, 115º, 140º, 165º and 180º during T2-TSE imaging were 0.1, 0.1, 0.1, 0.1, 0.1 and 0.1 ± 0.3 ºC for 4-channel safe mode pTx MRI and 0.4, 0.5, 0.6, 0.7, 1.0 and 1.1 ± 0.3 ºC for birdcage MRI, respectively. TR = repetition time; TE = echo time.

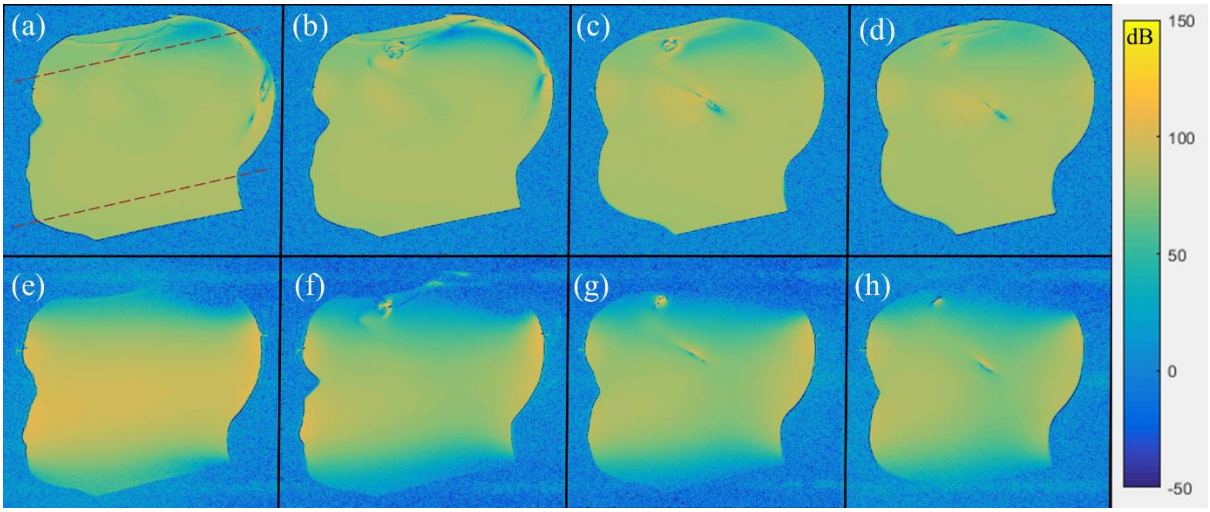

Fig. 4-10: Turbo spin-echo images of the homogenous head phantom were obtained at similar slice positions for standard birdcage (BC) and safe mode 4-channel parallel radiofrequency transmission (pTx) imaging. (a)-(d) displays the BC signal-to-noise ratio (SNR) results calculated using (3) and (4) per voxel; marked in red is the approximate field-of-view of the 4-channel pTx coil. (e)-(h) displays the analogous SNR results for safe mode 4-channel pTx. Comparable SNR was observed throughout, indicating that a good SNR performance is maintained in pTx safe mode.

4.3.4 Discussion and Conclusion

The temperature results provided several useful observations and demonstrated pTx MRI utility for a more clinically relevant pulse sequence. It was expected that increasing temperatures would be observed with increasing RF power, and the linear trend from increasing number of slices and the quadratic trend from increasing flip angle was also expected for birdcage MRI, as predicted by equation (4-3). 4-channel safe mode pTx MRI was able to suppress temperature changes to minimum levels for all tested scenarios and was quite resilient to increasing RF power conditions. The temperature increases remained constant (within the error margins of the temperature sensor). The result showed the capability of the safe mode technique to minimize the electric field and demonstrated good robustness to changing pulse sequence parameters. It was hypothesized that electric field strength would trend with RF power, and the effect would be independent of pTx or birdcage MRI; while this may still be the case for pTx MRI, the increase may not have resulted in a measurable temperature change. This relationship should be studied in simulation further to determine the limits of the proposed safe mode technique.

With respect to DBS patient safety, three of the ten tested scenarios resulted in birdcage imaging temperature elevations that were above the present safety guidelines of +1.0 ºC and one other with a marginal result. While there are imaging strategies to mitigate the safety risks of imaging DBS patients without the use of pTx or other methods, the most accepted practice, at present, is imaging cautiously with lower SAR pulse sequences. The present results agree with the practice established for MRI-conditional DBS devices: imaging with negligible heating can be achieved with low flip angles (although at the expense of reduced signal quality). The signal quality can then be recovered by extending the acquisition time and performing signal averaging, which is not an economical long-term solution. Furthermore, approximately 40 slices (at 3 mm resolution) are required for an average human head for complete brain coverage. This might not be achievable in a single session with standard birdcage MRI; extending scan time, if a full image set is necessary, is not economical. The present results suggest that, in comparison, the 4-channel pTx setup provided substantially more "headroom" to image with good image results in a time-efficient manner. Note that the experimental design included separate temperature measurements near the top of the phantom to ensure that localized heating was not suppressed at the expense of global temperature elevation. Temperatures at this location held steady at the ambient temperature during all pTx and birdcage MRI sessions.

Fig. 4-10 shows that the 4-channel pTx system produced good SNR, comparable to a conventional birdcage coil setup, suppressing the RF heating effects surrounding the wire tip (the region of minimization). In addition, the image quality can be further improved through the weighting factor in equation (4-1), provided the MRI safety guidelines are not exceeded. The RF coupling along the wire was non-zero, consistent with the simulated results in Fig. 4-5 (a). Fig. 4-10 (e) to (h) shows a slight increase in SNR along the surfaces of the phantom compared to birdcage results and a slow decrease in SNR with depth. This is expected, analogous to how multi-channel receiver coils have reduced depth sensitivity, especially when the channel count is relatively low [103]. It was evident from the MRI experimental results in Fig. 4-10 that some residual RF coupling remained in safe mode. This is likely due to choosing safe mode parameters by minimizing the electric field just at the wire tip and not at other elevated locations such as the top of the head and also due to experimental imperfections in implementing safe mode precisely based on numerical simulation. Notwithstanding the safe mode as implemented, the residual RF coupling remained effective at suppressing localized heating, as shown in Fig. 4-8 and 4-9.

In conclusion, while the additional phantom experiments continued to support the potential use of pTx MRI technology and the associated safe mode technique to suppress RF heating effects that may occur when imaging DBS patients, the results are not entirely conclusive, and more simulation and phantom experiments are necessary to ensure DBS patient safety when using pTx.

Chapter 5

A New Anthropomorphic Heterogeneous Phantom

This chapter reviews the current practice for MRI safety verification experiments with a particular focus on the challenges it presents for DBS MRI safety investigations. This is followed by a discussion of a preliminary experimental study that compares the DBS implant heating effects of two simple lead geometries relevant to DBS patients with complementary MRI experiments to demonstrate the potential need to utilize more sophisticated phantom structures in the experiment. This chapter concludes with a detailed description of a novel anthropomorphic heterogeneous phantom structure that addresses some of the limitations of current practices. Preliminary experimental results support the use of complex phantoms, particularly in DBS MRI safety applications. In conclusion, using advanced phantoms with improved realism appears advisable for DBS safety experiments, with additional work required to confirm improved human body electromagnetic characteristic accuracy. The work presented in this chapter has been published in or presented in a part of at,

- B. Yang, F. Tam, B. Davidson, P. S. Wei, C. Hamani, N. Lipsman, C.-H. Chen, and S. J. Graham, "Technical note: An anthropomorphic phantom with implanted neurostimulator for investigation of MRI safety," *Med. Phys*., 47(8):3745-3751, 2020.
- B. Yang, F. Tam, B. Davidson, C. Hamani, N. Lipsman, C.-H. Chen, and S. J. Graham, "An anthropomorphic phantom for deep brain stimulation MRI safety investigations," *Proc. 29th scientific meeting, Intl. Soc. Mag. Reson. Med.*, Virtual, 2021, p. 2297.
- B. Yang, F. Tam, B. Davidson, C. Hamani, N. Lipsman, C.-H. Chen, and S. J. Graham, "MRI safety of deep brain stimulation devices: Radiofrequency heating of a commercial lead and an insulated copper wire," *Proc. 28th scientific meeting, Intl. Soc. Mag. Reson. Med.*, Virtual, 2020, p. 4182

5.1 MRI Safety: Standard Phantom Construction

MRI safety studies rely heavily on the use of phantoms, which are typically open-faced rectangular-shaped containers filled with a single gel solution mimicking the electromagnetic properties of human tissue. ASTM International Standard phantom and gel solution recipe is widely used in MRI experiments [104]. Fig. 5-1 (a) displays the recommended phantom structure and dimensions representing the human head and torso, and (b) is a sample photograph of a constructed ASTM phantom. These phantom structures are especially important for patient safety investigations and are often the only safety measure prior to real patient imaging. This becomes very important when imaging patients with implanted DBS devices due to the risk of implant heating.

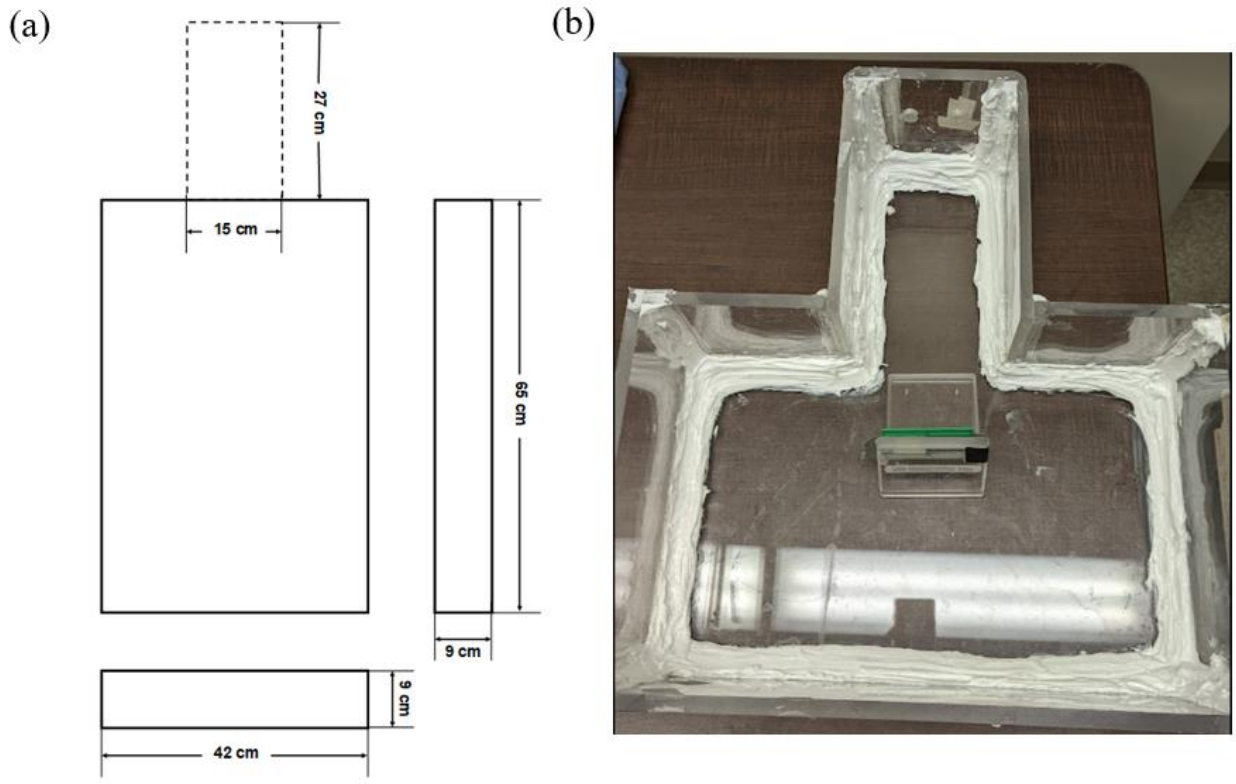

Fig. 5-1: The ASTM International Standard for magnetic resonance imaging safety experiments with phantoms, (a) illustrates the typical dimension of the phantom to simulate the human head and torso [104] and (b) a sample photograph of a constructed phantom (Photo courtesy of University Health Network, Canada).

5.1.1 DBS Safety Experimental Review

At present, the typical phantom setup for general patient safety studies involving conductive implants can commonly consist of a homogeneous ASTM phantom containing a gel solution with electromagnetic characteristics (i.e., electrical conductivity and permittivity) of a single tissue of interest or the human body average and copper wire inserts with temperature sensors attached for real-time temperature measurements. Fig. 5-2 displays two examples of MRI experimental setups, (a) studied the effectiveness of using RF shields surrounding the implanted copper wires to reduce localized RF heating effects along the wires [105] and (b) studied the effectiveness of using magnetic resonance thermometry, a non-invasive imaging method that estimates temperature changes within the imaging volume during an MRI scan [106].

For DBS patient safety studies, in particular, several experimental setups have been reported in the literature. Two examples of DBS setups are a head-only homogeneous gel-based phantom with an implanted copper wire (used as a substitute to a real DBS lead), as shown in Fig. 5-3 [107], and an ASTM phantom with a commercial DBS device implanted, as shown in Fig. 5-4 [108]. There are some apparent limitations when comparing the typical DBS patient and the experimental setups shown in Fig. 5-3 and 5-4. For example, the human head and torso on the ASTM phantom are very simplistic with sharp edges, and the real DBS leads are not externalized from the patient body. Although a real human brain model is very challenging to reconstruct, it is much more complex than a single tissue layer. Furthermore, DBS leads are manufactured at fixed lengths to be compatible with a wide range of human head sizes. There is often excess lead length that requires to be managed by the caring neurosurgeon. Fig. 5-5 illustrates nine DBS patients' lead trajectories and the possible variability across different DBS patients [109]. Because DBS implant heating effects are governed by electromagnetic radiation principles and have "antenna-like" characteristics, DBS lead positioning interaction with the human body will affect the overall electromagnetic distribution and, thus, potentially, the level of RF coupling an implanted DBS device will experience. Consequently, recent studies have investigated the role of surgical lead management, and the results have shown that different lead trajectories can have a substantial impact on localized RF heating effects [110]. DBS researchers have also started evaluating the use of more sophisticated human models in simulation and phantom structures with improved realism in the experiment [111, 112]. Although a conceptually logical step, several fundamental questions

remain and are explored in this chapter, which includes the investigation of using copper wire as a DBS lead substitute, the impact of lead trajectories, and the possible benefit of using a complex heterogeneous phantom for advanced DBS MRI safety studies.

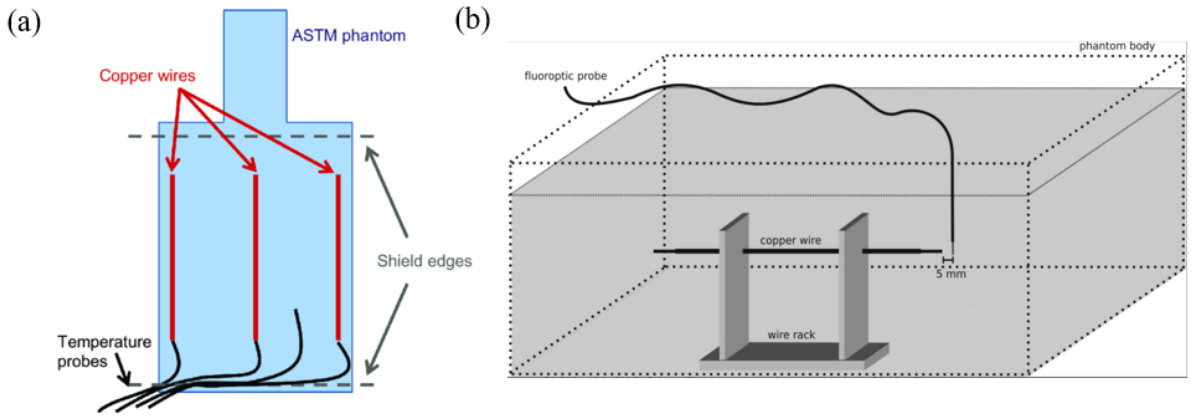

Fig. 5-2: Common magnetic resonance imaging experimental setups for implant safety investigations, (a) investigates the benefits of using radiofrequency shields to reduce temperature increases along copper wire inserts [105] and (b) studies the use of magnetic resonance thermometry to estimate the temperature in a copper wire [106].

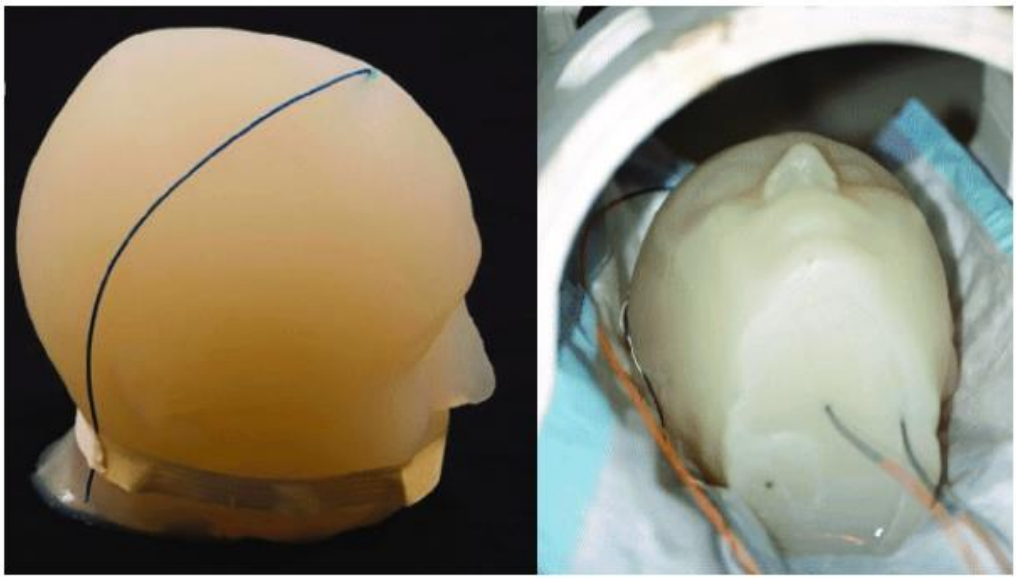

Fig. 5-3: Example gel-based head-only phantoms with implanted copper wires and temperature sensors for deep brain stimulation safety investigations [107].

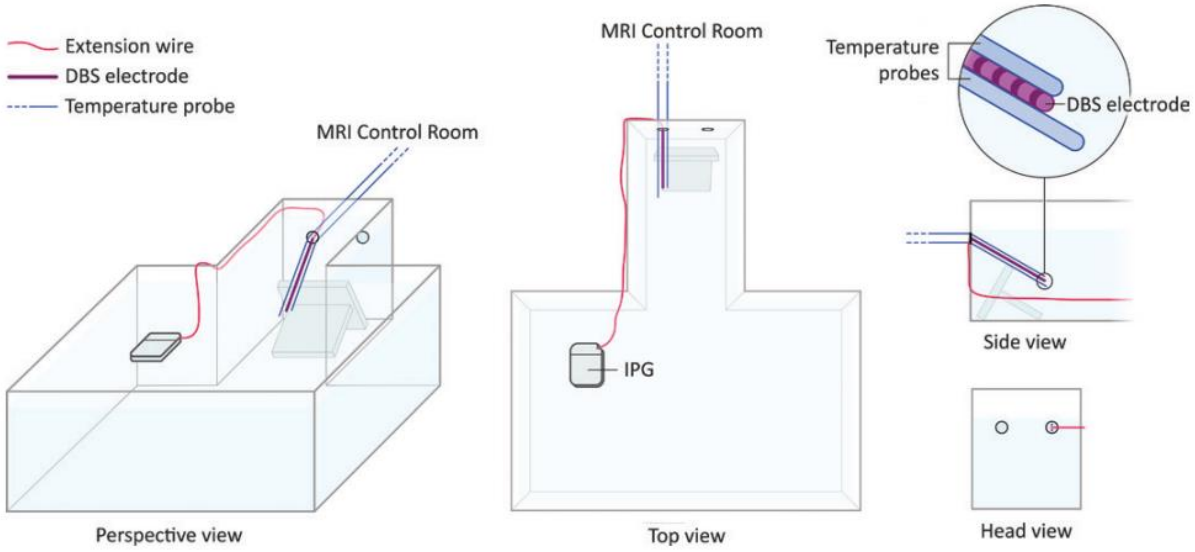

Fig. 5-4: A typical deep brain stimulation (DBS) magnetic resonance imaging experimental illustration using a commercial DBS device and an ASTM standard phantom with a rack for improved DBS lead positioning [108]. IPG = implantable pulse generator.

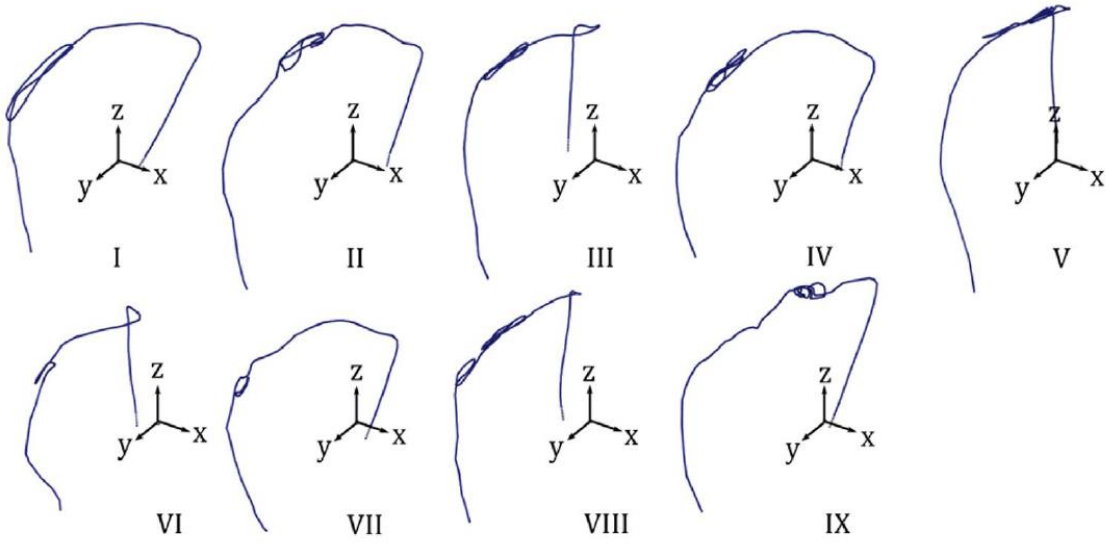

Fig. 5-5: Nine actual deep brain stimulation lead trajectories modeled from real patients for magnetic resonance imaging safety investigations [109].

5.2 DBS MRI Safety: Simple Phantom Study

The usage of DBS treatment continues to grow worldwide. MRI can play an important role in the workflow to fit patients with DBS devices, but there are safety concerns that must be considered when imaging is conducted post-implantation. In these situations, the RF

electromagnetic field can induce electrical current to flow along the device, increasing the possibility of exceeding the present MRI safety guidelines for local SAR and, in more severe incidences, causing tissue damage. Researchers thus far have relied heavily on phantom studies for safety investigations in advance of patient imaging and for demonstrating new methods to enhance MRI safety in proof-of-concept [113, 114]. Often, simple homogenous phantoms and/or copper wires are used respectively to emulate the electromagnetic behaviour of human tissue and commercial DBS leads during MRI. Given the simple construction of such setups, however, the level of realism can be somewhat limited, as the DBS lead trajectory post-implantation varies greatly amongst DBS patients. Alternatively, complex heterogeneous anthropomorphic phantom structures can be designed and assembled quite easily using 3-D printing methods, with the inclusion of actual DBS devices. Cost becomes more of a factor in this case, as DBS devices are expensive. These considerations make it important to examine the suitability of using copper wires to emulate MRI-DBS conditions. The present work addresses this aim by investigating the use of copper wire versus a commercial DBS lead in RF heating experimental setups testing two simple lead trajectories.

5.2.1 Material and Methods

To investigate the RF heating profiles of a commercial DBS lead and copper wire, RF heating experiments were conducted on a 3 T MRI system (Magnetom Prisma, Siemens Healthineers, Erlangan, DEU) configured for body coil RF transmission and reception using a turbo spin-echo (TSE) pulse sequence (TR / TE = 6000 ms / 103 ms, flip angle = 165, duration = 1:38 mins). A 19 cm x 33 cm x 13 cm rectangular container was filled with a poly-acrylic acid (10 g/L) and salt (1.32 g/L) solution that produced a conductivity of approximately 0.47 S/m and a relative permittivity of approximately 80. The gel-based solution filled the container to a depth of 9 cm. A 40-cm long commercial DBS lead (3387, Medtronics, Minneapolis, MN) and a 40-cm long insulated copper wire (AWG 22) with a 1.3 cm exposed tip were used in two experimental setups. In the first setup, the DBS lead and copper wire were routed such that the looped section (or a majority thereof) was externalized from the phantom solution with the tip-end submerged to an approximate depth of 6 cm into the phantom solution, as shown in Fig. 5-6 (a), using the DBS lead. In the second setup, the DBS lead and copper wire were fully immersed into the phantom, as shown in Fig. 5-6 (b), using the insulated copper wire. Temperature measurements for RF heating

effects were recorded at locations near the lead and wire tips, as shown in Fig. 5-7 using fiber-optic temperature sensors (OTG-MPK5, Opsens Inc., Quebec City, QC). Control measurements were recorded at the opposite end of the container using a fiber-optic temperature sensor (T1, Neoptix, Québec City, QB) to verify that RF heating effects were localized.

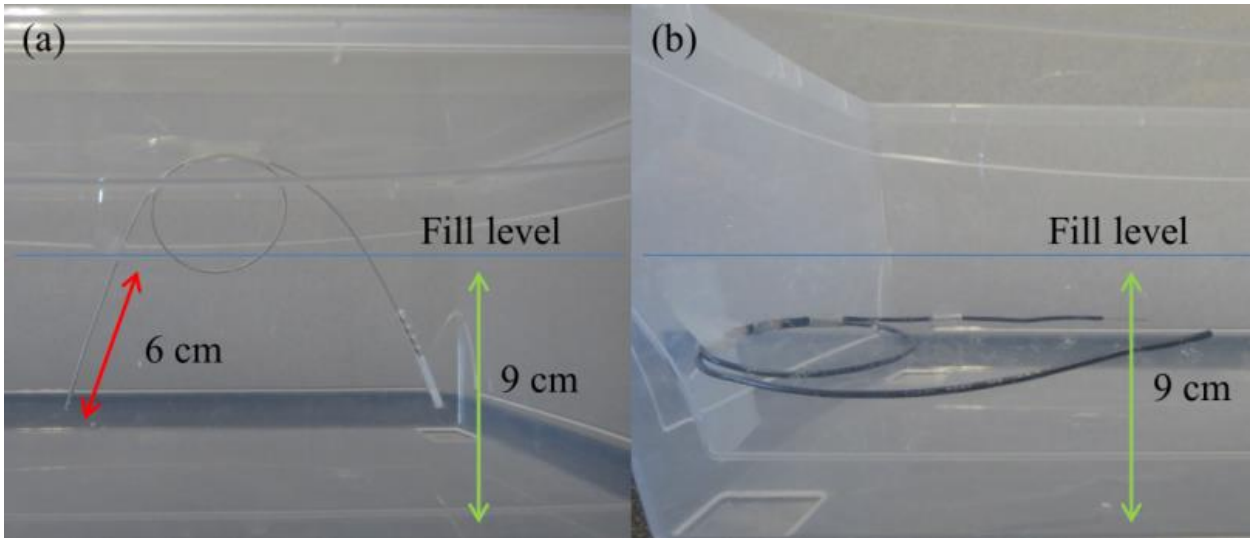

Fig. 5-6: Magnetic resonance imaging experimental setup and lead trajectory used; a) excess lead externalized with 6 cm insertion into phantom and b) lead fully submerged in phantom.

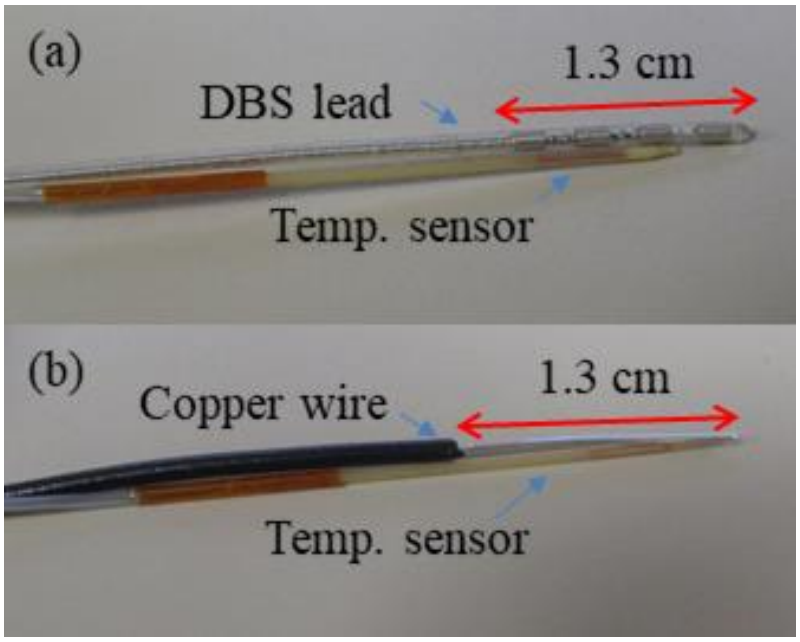

Fig. 5-7: Temperature sensor location on; a) commercial deep brain stimulation electrode and b) conventional insulated copper wire. Temp. = temperature.

5.2.2 Experimental Results

The MRI temperature results for the RF heating experiments are shown in Fig. 5-8. Fig. 5-8 plots the temperature elevations for TSE imaging for all test scenarios. Temperature increases for setup 1 were 1.6 ± 0.3ºC when imaging with the copper wire and 0.7 ± 0.3ºC when imaging with the DBS lead. For setup 2, temperature increases were 0.4 ± 0.3ºC for the copper wire and 0.1 ± 0.3ºC for the DBS lead. Fig. 5-9 shows a sample TSE image at a slice intersecting the DBS lead and copper wire. It can be observed that the lead and wire create an image artifact that extends beyond its size, thus impairing the diagnostic capabilities of MRI imaging in its surroundings. This is expected and is another challenge of imaging DBS patients.

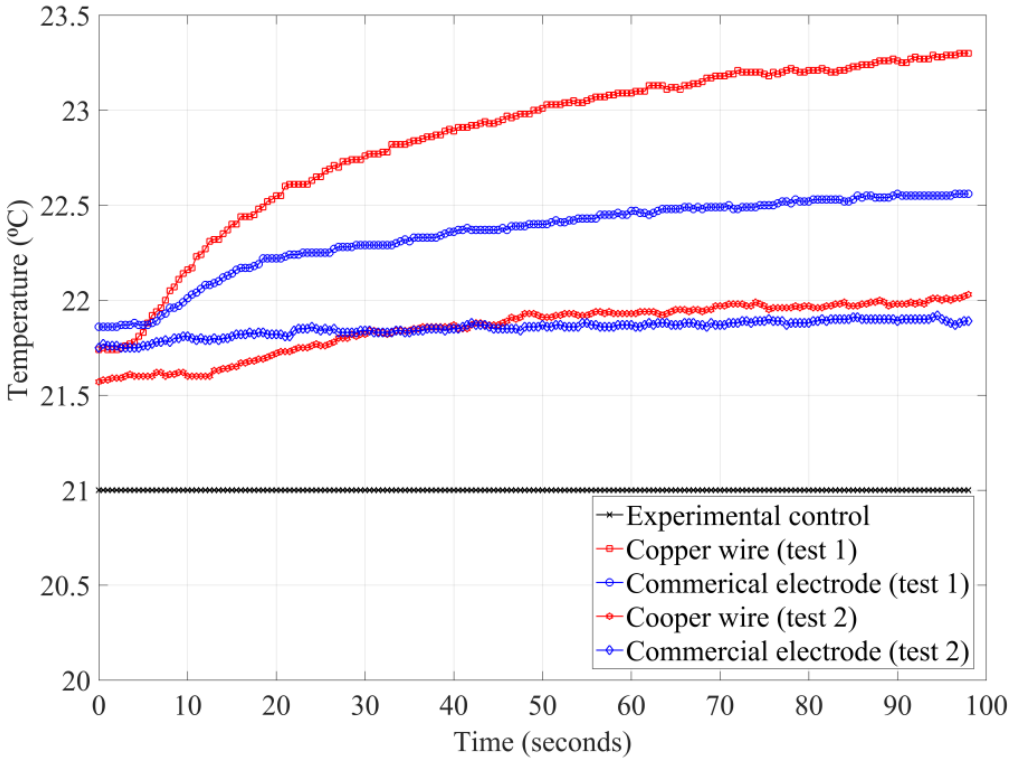

Fig. 5-8: Magnetic resonance imaging radiofrequency heating and experimental control temperature elevations. Temperature increases for test 1 were 1.6 ± 0.3ºC when imaging with the copper wire and 0.7 ± 0.3ºC when imaging with the deep brain stimulation lead. For test 2, temperature increases were 0.4 ± 0.3ºC for the copper wire and 0.1 ± 0.3ºC for the deep brain stimulation lead. The ambient phantom temperature (or experimental control) held steady for the entire imaging duration.

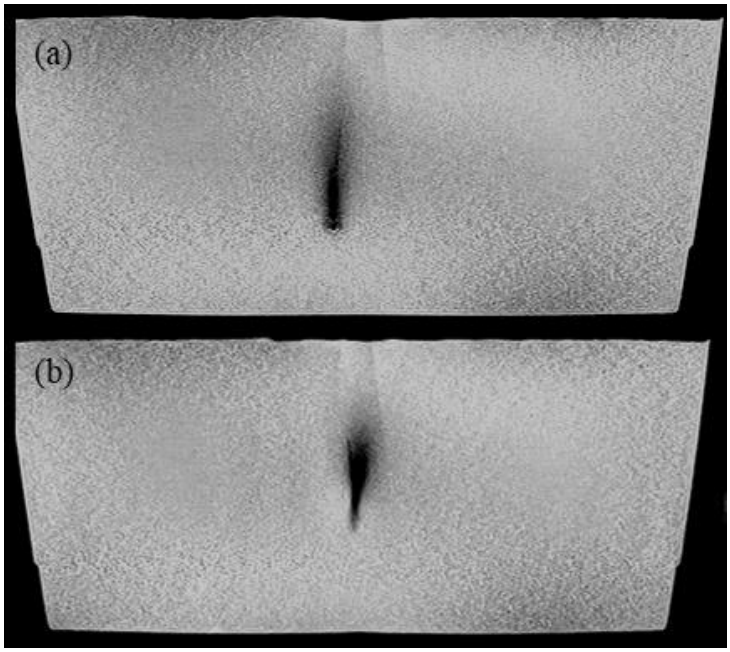

Fig. 5-9: Reconstructed turbo spin-echo image of the phantom with (a) inserted commercial deep brain stimulation lead and (b) inserted copper wire. As expected, a significant magnetic susceptibility artifact can be observed around the implanted deep brain stimulation lead and wire.

5.2.3 Discussion and Conclusion

The experimental results showed that the commercial DBS lead was more resistant to RF electromagnetic coupling than the conventional copper wire. The temperature increase obtained from the DBS lead was over 50% lower in both setups. Engineering design is likely the key contributor to this difference. For example, the DBS lead is a multi-layer structure that uses platinum-iridium wire and fluoropolymers for insulation. While the general heating characteristics of the DBS lead and copper wire seem consistent, the overall result suggests that moving toward a complex phantom structure with a commercial DBS device is advisable for improved realism while highlighting the significant difference in temperatures measured, a useful observation for researchers in the field to consider when conducting safety experiments. A new multi-layer phantom construction capable of replicating actual DBS lead trajectories is presented, and its utility is explored in the next section.

5.3 A New Anthropomorphic Heterogeneous Phantom

DBS is known to improve the quality of life for patients with certain neurological or psychiatric disorders [115–117]. Despite the treatment benefits of DBS, the mechanism underlying

the effect is poorly understood, limiting treatment evaluation and technological advancement. MRI offers excellent soft tissue contrast that can benefit the health management of DBS patients during pre- and post-surgery procedures [119]. Furthermore, functional magnetic resonance imaging (fMRI) is an effective, non-invasive technique for indirectly measuring neural activity in research settings to advance studies of DBS technology [120]. However, MRI of DBS patients is currently highly restricted due to safety concerns. In particular, RF electric field energy during MRI can couple with the implanted DBS leads and neurostimulator, inducing electrical current to flow into adjacent brain tissue. As a result, elevated local SAR and heating can occur, potentially causing bodily harm (e.g., tissue damage) [121–123].

Researchers have proposed different methods to overcome this challenge. Examples include the use of parallel RF transmission to generate a minimized electric field region at target locations surrounding the DBS device [124], a reconfigurable MRI birdcage coil that re-orients the inherent low electric field zone to a desired position (e.g., the tip of the DBS lead) [125], and electric field cancellation through modifications to the DBS lead trajectory [110].

Simple homogeneous phantoms (e.g., the ASTM International standard) play an important role in the initial verification of novel techniques and proof-of-concept demonstrations toward safe MRI of DBS patients [121–123]. However, given that DBS surgical procedure commonly involves the implantation of the device within multiple tissue compartments, including the penetration of leads with unilateral or bilateral electrodes culminating in deep brain structures (e.g., the thalamus), there may be advantages in engineering heterogeneous phantoms to provide a better approximation of the expected MRI-DBS device interactions. Recent studies show that in addition to the DBS electrode tip, there is the potential for other sites along a DBS lead trajectory to experience higher electric field coupling effects [124] and that the management of excess lead length, specifically at the entry point on the human skull to the brain target can significantly impact electric charge accumulation at the DBS electrodes [110]. Neurosurgeon habits and surgical procedures can vary with respect to implanting DBS devices, contributing to the complexity of imaging DBS patients [110] and suggesting that a strategy should be incorporated in MRI safety research to consider the effects of such factors. At present, approximating actual DBS lead trajectories in simple homogenous phantoms can be challenging without proper support structures such as a skull or a lack of compartments representative of different biological media [104, 126].

For these collective reasons, anthropomorphic heterogeneous phantoms with enhanced anatomical realism that capture the uniqueness of surgical procedures are desirable to enhance the utility of MRI safety research findings. Anthropomorphic phantoms are thus being created for such MRI applications and other applications [127, 128] and have become much more feasible in recent years due to advances in 3D printing technology.

This section presents the design, fabrication, and assembly of a 3D-printed anthropomorphic heterogeneous phantom with implanted bilateral DBS leads and a neurostimulator for MRI safety investigations at 3 T. The novel phantom especially provides a platform to replicate surgical procedures relating to the lead trajectory, a potential safety concern [110, 126]. Experimental demonstrations of RF heating utilizing the phantom in two configurations were conducted that recorded temperature elevations. The first configuration used a heterogeneous setup consisting of a human skull, two tissue-mimicking solutions, and a realistic DBS lead trajectory. The second configuration used a homogeneous setup that fills the phantom with a standard body average solution to assess the initial utility and gain preliminary insight on the potential 3 T MRI safety risk associated with a clinical DBS surgical procedure. The work concludes with a discussion of the results obtained in comparison to previous results in [129] and future considerations to validate the benefit of using such an anthropomorphic heterogeneous phantom.

5.3.1 Background

SAR is the primary MRI safety parameter used to assess levels of RF power deposition. Specifically,

$$SAR_{\Delta v}(t) = \int \frac{\sigma(r)|\boldsymbol{E}(r,t)|^2}{\rho(r)} dv, \tag{5-1}$$

where r is the position, σ is the conductivity of tissue, ρ is the mass density, $\boldsymbol{E}(r,t)$ is the total electric field vector at the position r as a function of time, dv is the differential volume element, and Δv is the volume over which the integral is calculated. In practice, safety monitoring equipment on MRI systems is designed to estimate SAR values that are temporally averaged and spatially averaged over the sensitive volume of the RF transmitter, such as the "head-averaged" or "body-averaged" SAR. This approach works well at 1.5 T and 3.0 T for most patient safety monitoring,

assuming in particular that the electric field varies slowly in space. Unfortunately, this is not the case for implanted conductive medical devices, such as those used in DBS. Electromagnetic simulations show that the component of the transmitted electric field that is tangential to the DBS lead may force charge to accumulate at the electrode, intensifying the local electric field at the tip region [114, 130]. Substantial current may flow into the surrounding neural tissues in this scenario, with the possibility of significant local temperature elevations and either transient or permanent deleterious effects [131].

As part of the strategies to overcome the limitations of head-averaged SAR in the present concept, increasing focus has been placed on understanding the localized temperature elevations that may occur during the MRI of DBS implants. The relationship between RF power deposition and temperature elevation is complex in tissue because blood flow provides a tempering effect. According to Penne's bioheat equation [125, 132]:

$$\rho c \frac{\partial T}{\partial t} - \nabla \cdot k \nabla T - Q_{met} + \rho_b c_b w (T - T_b) = (SAR)\rho, \tag{5-2}$$

where T is the temperature rise, c is the specific heat capacity, k is the thermal conductivity, Q_{met} is metabolic heating, ρ_b is the mass density of blood, c_b is the specific heat capacity of the blood, w is the perfusion of blood, T_b is the blood temperature, SAR is the local specific absorption rate, and all parameters are assumed to depend on position. Detailed explorations of this relationship are of interest, but for practical purposes, phantoms with implanted devices can be used in the absence of perfusion to assess worst-case scenarios of localized heating. Simplifying,

$$\rho c \frac{\partial T}{\partial t} - \nabla \cdot k \nabla T = (SAR)\rho \, . \tag{5-3}$$

Thus, mapping temperature elevations in time and space can, in principle, allow the local SAR to be estimated. Recognizing that the region of an intense electric field is highly localized, however, many MRI safety studies opt for the much simpler approach of affixing an MRI-compatible temperature probe to the tip of the implant. This approach is adopted in the present work, providing a good estimate of the worst-case temperature elevation in space for the specific MRI conditions described below.

5.3.2 Methods

This section describes a new phantom design, fabrication, and MRI experimental procedure to study DBS MRI patient safety implications.

5.3.2.1 Phantom Model and Fabrication

The computer-aided design (CAD) model of the anthropomorphic phantom consisted of a head, neck, and torso (Fig. 5-10) and was developed using Inventor 2019 (Autodesk, San Rafael, CA, USA). To represent the interaction of RF fields with patient geometry, the design included reasonably realistic yet generic features of the head, neck, and torso [Fig. 5-10 (b)]. Cut-out plates were located in the head and chest to allow easy filling and re-filling of the phantom, and various screw holes were placed for air to escape so that filling was achieved without air bubbles. Internally, thin beams were placed to support and guide the DBS leads and fiber-optic temperature sensors to the desired pathway from the skull to the chest cut-out plate. The beams also served as a mechanism to prevent significant shifting of devices along the pathway. To support the neck and ensure tight fitting, two nut and bolt lugs were included in the design. The rest of the phantom assembly incorporated a tongue and groove design for tight fitting.

The CAD phantom model was 3D printed (Viper SLA, 3D Systems, Rock Hill, SC, USA) using Accura ClearVue material (3D Systems, Rock Hill, SC, USA). To meet the size restriction on the 3D printer, the torso component of the model was printed in two pieces. The phantom was designed as a single-volume structure, and the general dimensions to the nearest centimeter are listed in Table 5-I.

Table 5-I: Assembled phantom dimensions

Head	Circumference = 62 cm	Height = 18 cm	
Neck	Circumference = 35 cm	Height = 6 cm	
Torso	Length = 45 cm	Width = 15 cm	Height = 21 cm

Interior wall thickness = 1 cm

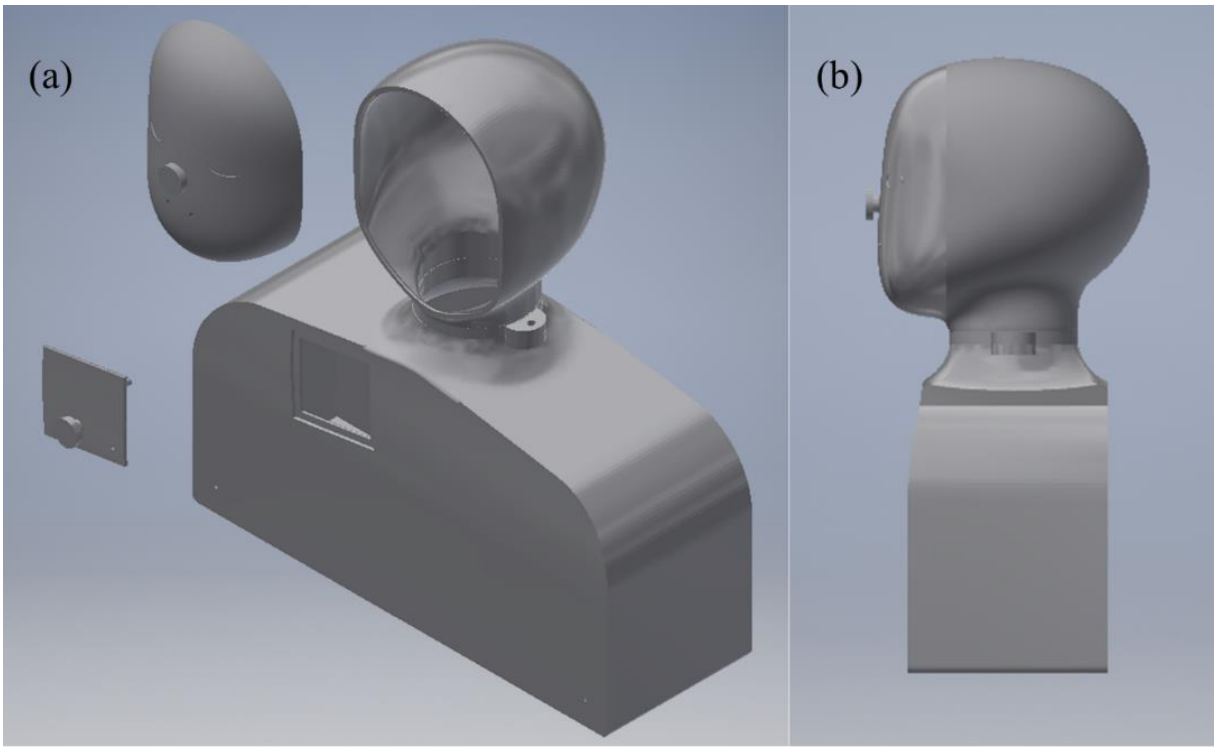

Fig. 5-10: Computer-aided design model of the anthropomorphic phantom, as designed in Autodesk Inventor 2019: (a) three-dimensional view and (b) side view.

5.3.2.2 Phantom Assembly and Implantation of the DBS Device

A human skull was included within the head cavity to account for the substantial variation in electromagnetic properties between bone and brain tissue [133]. The phantom was filled in a two-stage process: the skull fill stage, described here, and the final fill stage, described further below. The skull was filled with a gel consisting of bovine skin gelatin (170 g/L; 225 g bloom, Sigma Aldrich, St. Louis, MO, USA), sodium chloride (NaCl) (4.5 g/L; ACS reagent, Sigma Aldrich, St. Louis, MO, USA) and canola oil (3 % of total volume). The gel preparation followed the procedure reported by Lazebnik *et al*. [134] to emulate the electromagnetic characteristics of grey matter (relative permittivity of approximately 67, the electrical conductivity of approximately 0.69 S/m, as previously measured by our group [124]).

The first filling stage involved a special method to ensure that the gel-filled the skull without leaving air pockets. The skull and gel were placed into a plastic bag and vacuum sealed using a plastic tube located at a small opening in the bag. The vacuum suction compressed the bag, forcing the liquid solution into the skull. The vacuum suction was applied continuously until the

gel solidified, a process that took approximately 3 – 4 hours. As a consequence, the nasal and eye crevices in the skull were also filled, however, at minimal impact to the intended purpose of the phantom.

The DBS surgical procedure was then performed by an experienced neurosurgeon (B. D.). Two DBS leads (3387, Medtronics, Minneapolis, MN, USA) and an implantable pulse generator (IPG) neurostimulator (Activa PC, Medtronics, Minneapolis, MN, USA) were implanted into the head and torso, respectively. The leads were implanted through two targeted burr holes on the skull (in the right and left hemispheres) to the approximate depth of the thalamus and held in place by the support of the surrounding solidified gel. The DBS device placement and routing were representative of current surgical standards at Sunnybrook Health Sciences Centre in Toronto, ON, Canada. Fiber-optic temperature sensors (T1, Neoptix, Quebec City, QB, CAN) were sutured to each lead near the electrode tip and were implanted together with the DBS leads, labeled as 1* and 2* in Fig. 5-11 (a) to record changes in temperature during MRI. A section of the "excess" DBS lead wire was routed in a spiral trajectory and taped on the skull and then routed and taped around the approximate location of the ear to the IPG, located on the torso, via the thin beams placed near the neck, as shown in Figs. 5-11 (b) and 5-11 (c). The remaining loose wire was wrapped and taped to the deep surface of the IPG in a similar spiral pattern. The shallow surface of the IPG was then glued onto the interior surface of the chest cut-out plate. Three other temperature sensors (2 from Neoptix and 1 from Opsens, Quebec City, QB, CAN) were attached to record the temperature at the spiral trajectory labeled as 3 in Fig. 5-11 (a) at the left lead extension connection (OTG-MPK8, Opsens) labelled as 4 in Fig. 5-11 (b) and on the surface of the IPG labeled as 5 in Fig. 5-11 (c). All temperature sensors exited the phantom through a small hole on the chest cut-out plate and filled with silicon to prevent leakage.

The assembled phantom with a human skull, DBS leads, and IPG implanted as described above prior to the final fill stage is shown in Fig. 5-11 (c). The final layer, filling the remaining phantom volume, followed the ASTM International body average standard (poly-acrylic acid: 10 g/L and NaCl: 1.32 g/ L), producing a conductivity of approximately 0.47 S/m and relative permittivity of approximately 80.24 [104].

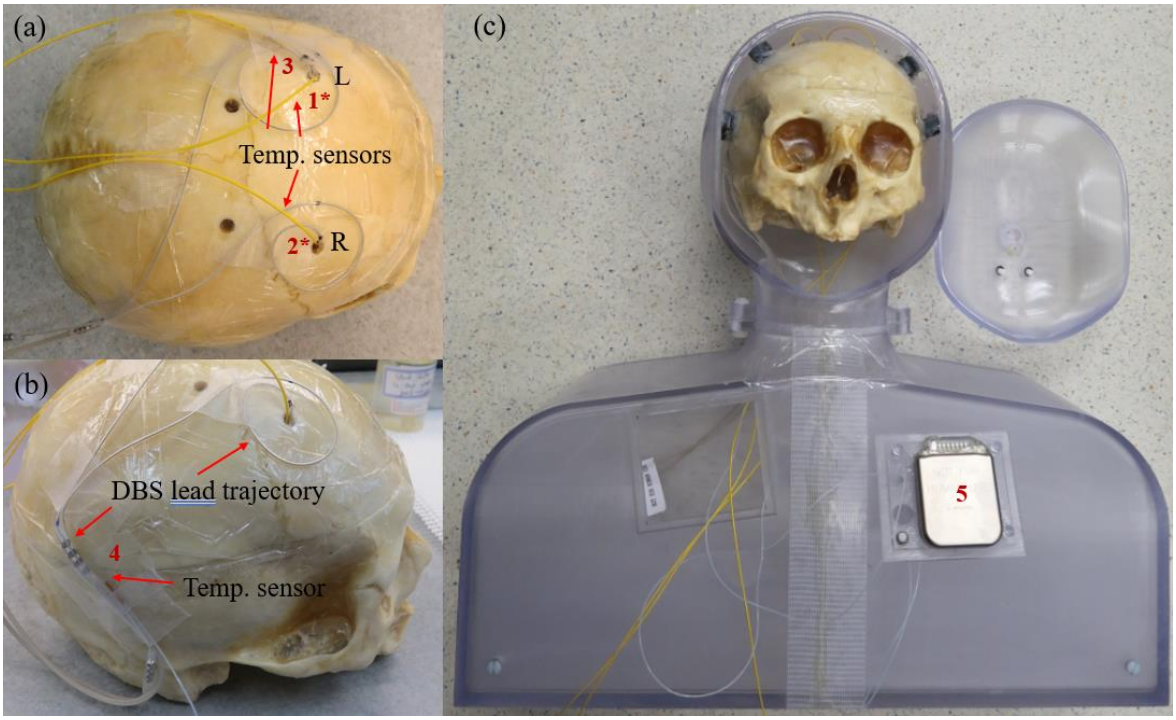

Fig. 5-11: Gelatin-filled human skull with implanted deep brain stimulation (DBS) leads and fiber-optic temperature sensors, and the assembled phantom: (a) location of the temperature sensors: sensors 1* and 2* were implanted to the approximate location of the thalamus inside the skull, whereas the sensor 3 was at the spiral trajectory outside the skull; (b) right DBS lead trajectory and the temperature sensor 4 located at the left DBS lead extension connection point outside the skull; and (c) assembled three-dimensional printed phantom with the skull, fiber-optic temperature sensors, implanted bilateral DBS leads and neurostimulator with the temperature sensor 5 located on the surface. The phantom is shown prior to the final fill. L = left; R = right; Temp = temperature.

5.3.2.3 Experimental Method

Current safety requirements for MRI-conditional DBS devices specify that the neurostimulator should be powered off during imaging [135, 136] and only powered on under clinician request. However, many DBS patients suffer from movement-related symptoms that can potentially produce substantial motion artifacts during MRI. Therefore, imaging is very desirable with the device powered on. RF heating experiments were thus conducted for the phantom with the implanted DBS device in "IPG on" and "IPG off" conditions using a 3 T MRI system (Magnetom Prisma, Siemens, Erlangen, GER). The experiments were conducted with turbo spin-echo (TSE) imaging, a pulse sequence that is capable of concerning RF power deposition and that is routinely avoided in clinical DBS patient studies [122, 124, 126]. The MRI system was

configured for RF transmission and reception using the standard birdcage coil. The absolute temperature elevations were recorded throughout imaging at the test points mentioned above with reference to Fig. 5-11: the DBS electrode tips; the spiral trajectory on the left DBS lead; the left DBS lead extension connection; and at the surface of the IPG.

For comparison, an analogous RF heating experiment was conducted with the phantom filled with only the ASTM International body average standard material, as commonly used in homogeneous phantom setups. The IPG with bilateral DBS leads was placed, routed, and taped along the interior walls (in a non-specific DBS lead trajectory) before routing the leads to the center of the head, similar to recent literature [126]. Temperature sensor locations remained consistent with the heterogeneous phantom setup.

5.3.3 Experimental Results

MRI TSE acquisition parameters and experimental results are reported in Table 5-II for a 6-feet tall, 200-pound male pseudo-patient. The spatially averaged SAR, as estimated by the MRI system, was 0.075 W/kg for the heterogeneous setup and 0.078 W/kg for the homogeneous setup. For the IPG off condition, the maximum elevations recorded for the heterogeneous and homogeneous setup were 1.1 ± 0.2°C (right hemisphere lead tip) and 0.8 ± 0.2°C (left hemisphere lead tip), respectively. For the IPG on condition (bilateral voltage amplitude = 4 V), the analogous maxima were 0.9 ± 0.2°C (left hemisphere lead tip) and 0.9 ± 0.2°C (right hemisphere lead tip), respectively. The remaining locations experienced temperature increases ranging from 0.1 ± 0.2 to 0.5 ± 0.2°C throughout. The variable measurement errors (i.e., ±0.3 and ±0.2) are due to the use of temperature sensors from different manufacturers.

Table 5-II: Summary of MRI acquisition parameters and RF heating results

TSE: repetition time = 6000 ms, echo time = 100 ms, flip angle = 165º, acquisition matrix = 256 x 512, field-of-view = 220 mm, phase encoding direction = R >> L, slice thickness = 5 mm, slices = 24, echo train = 9, measurement = 3, time = 8:50 mins					
Temperature increase (ºC)					
Heterogeneous phantom setup					
	L hemisphere (1)	R hemisphere (2)	L burr hole (3)	Lead ext. (4)	IPG (5)
IPG off	0.3 ± 0.2	1.1 ± 0.2	0.5 ± 0.2	0.4 ± 0.3	0.5 ± 0.2
IPG on	0.9 ± 0.2	0.4 ± 0.2	0.5 ± 0.2	0.3 ± 0.3	0.3 ± 0.2
Homogeneous phantom setup					

	L hemisphere (1)	R hemisphere (2)	L burr hole (3)	Lead ext. (4)	IPG (5)
IPG off	0.8 ± 0.2	0.7 ± 0.2	0.1 ± 0.2	0.2 ± 0.3	0.1 ± 0.2
IPG on	0.7 ± 0.2	0.9 ± 0.2	0.1 ± 0.2	0.2 ± 0.3	0.1 ± 0.2

L = left; R = right

Figures 5-12 (a) and 5-12 (b) display reconstructed transverse images of the phantom for the TSE parameters listed in Table 5-II for IPG off and on, respectively. In addition, to depict the MRI appearance of the phantom, Fig. 5-12 (c) shows a reconstructed sagittal image at a slice intersecting one of the DBS lead locations, as acquired from a separate TSE imaging session using the standard 20-channel receive-only head and neck array coil for signal reception and body coil for signal transmission.

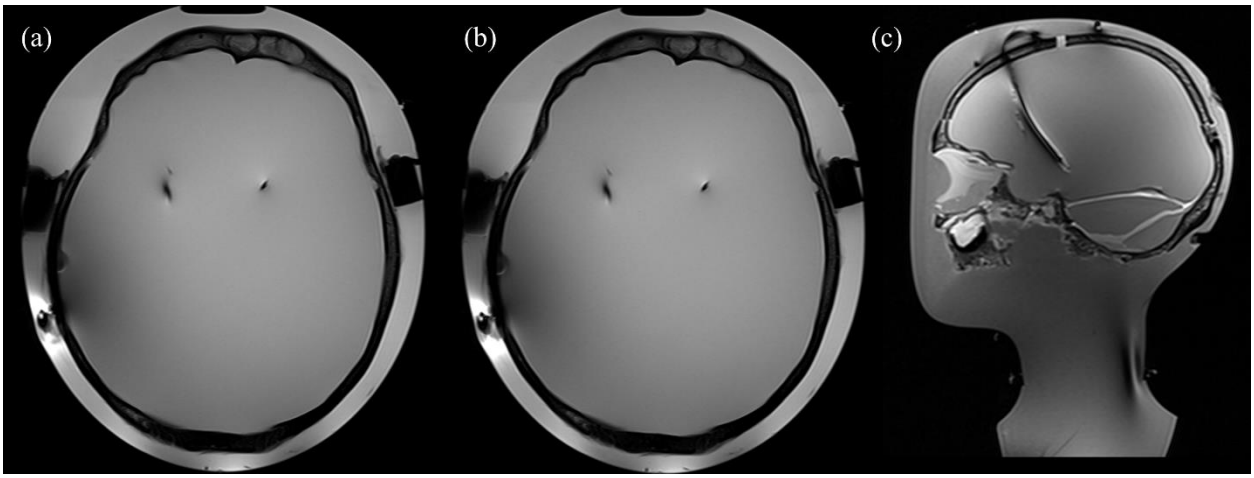

Fig. 5-12: Turbo spin-echo images of the phantom: (a) reconstructed transverse view for implantable pulse generator (IPG) off using transmit/receive birdcage coil; (b) reconstructed transverse view for IPG on using transmit/receive birdcage coil; and (c) a reconstructed sagittal view for phantom illustration purposes using 20 channel receive-only head and neck array coil and body coil for transmission acquired from a separate imaging session.

Overall, the MRI signals are as expected, with reasonable uniformity in most of the locations filled with gel. Signal heterogeneity within the skull and some signal artifacts local to the DBS lead, observed as reduced and elevated signal, appear to be consistent with a mismatch in the magnetic susceptibility of the DBS device in relation to the surrounding gel. Lastly, an elevated MRI signal was also observed along the electrode of the DBS device. The elevation is slight, consistent with a device designed to produce a low level of RF coupling and with the small temperature elevations reported in Table 5-II.

5.3.4 Discussion and Conclusion

Overall, the anthropomorphic phantom produced good reconstructed images with good homogeneity between the different layers and enabled a preliminary safety evaluation of a clinical DBS lead trajectory. A clear distinction between the brain, skull, and body boundaries was observed, and the implanted DBS device introduced small magnetic susceptibility and RF coupling artifacts. Two aspects of the RF coupling artifacts warrant further discussion below. First, the small amount of RF coupling, as confirmed by the temperature probe measurements, is an improvement when compared to more simplistic measurements previously conducted in the laboratory involving implanted wires in a homogeneous phantom [129]. As a result, for DBS patient safety studies, it appears advisable to use commercial devices rather than copper wire substitutes. This resiliency likely resulted from multiple factors, but especially the design of the DBS device itself, which is designated as MRI-conditional for imaging at 1.5 T with multi-layer construction and device shielding to external RF interference. For both experimental setups, maximum temperature elevations at the lead tips were approximately 1.0°C (the present MRI safety guideline limit [135, 136]) irrespective of whether the IPG was powered on or off. The additional temperature sensors placed at the left burr hole and lead extension connection experienced only marginal heating, a promising initial result as past work has suggested that heightened electric field intensity is possible in these regions under certain conditions [110, 124]. A second interesting observation was that markedly different temperature increases were measured at each DBS electrode/lead tip for the heterogeneous setup. Instead of similar bilateral heating (as observed in the homogeneous phantom setup), the temperature increase was strongly left-sided or right-sided depending on whether the IPG was powered on or off, respectively. These effects reflect the spatial asymmetry of the implanted DBS lead trajectories and that the RF coupling between the DBS leads is affected by the IPG power status under certain conditions. Such complexities could have important implications for MRI safety in DBS patients and highlight the importance of carefully conducted experiments using anthropomorphic phantoms with actual DBS devices to augment simpler experiments. More studies of this observation are warranted.

The DBS lead placements and trajectories used in the present study are representative of current practice at our institution, which is an active program of neuromodulation research. The initial results reported here will help to support off-label clinical research studies involving limited

MRI at 3 T toward an improved understanding of the DBS mechanism of action in patients [126, 137]. The anthropomorphic phantom will also be required in future research to develop safe procedures for RF-intensive MRI of DBS patients at 3 T and higher field strengths, as may be possible using methods such as pTx [124]. It is apparent from recent literature that pTx researchers are quickly moving toward more realistic human models in simulation studies, and thus, the anthropomorphic heterogeneous phantom construction presented here may be useful to others in this field [110, 124, 138].

Although the presented results are promising, and using improved phantoms is conceptually logical, more supportive evidence needs to be accumulated before further conclusions can be made. The phantom dimensions are realistic, but several physical attributes, such as the curvature of the neck, chin, and torso, need to be evaluated further to assess the impact on in vivo DBS safety experiments and, in particular, the realism of the tangential electric field component. Such assessments will likely involve electromagnetic simulations as part of predicting the effect of manipulating these attributes on biological responses.

In conclusion, a promising anthropomorphic heterogeneous phantom construction for investigations of MRI safety involving DBS is presented, along with preliminary MRI RF heating demonstrations that reported small temperature elevations pertaining to a clinically realistic bilateral DBS lead placement. As a final remark, the presented results cannot be generalized to all MRI systems or used to predict experimental outcomes at other institutions with similar DBS surgical procedures. The results are intended instead to promote further research and knowledge transfer, with the ultimate intention of progressing toward safe unrestricted MRI of DBS patients in the future.

Chapter 6

Conclusion and Future Work

This chapter summarizes this thesis, some final remarks and future work recommendations.

6.1 Conclusion

MRI safety of DBS patients will continue to be a future clinical challenge as ultra-high field MRI systems make further in-ways into imaging clinics. With MRI vendors now offering pTx functionality in many of their newer models, a platform to implement pTx safe mode methods on clinical systems, such as the technique presented in Chapter 1, may be possible in the future. The main safety concern with DBS devices originates from the risk of RF energy coupling onto the long conductive DBS leads, resulting in electrical charge accumulation that scatters into adjacent tissue, potentially causing bodily damage. Chapter 1 introduced the topics of DBS and how this treatment option can improve the quality of life for patients suffering from different neurological conditions. This was followed by a discussion on the current state of MRI safety and a review of experimental data that suggested the potential risks associated with imaging DBS patients. An introduction to the basic concept of pTx MRI followed, and the chapter concluded with a detailed discussion of the promising pTx safe mode technique used in this work.

Chapter 2 expanded on the topic of pTx and presented the pTx system architecture that demonstrated in proof-of-concept the proposed implant-friendly safe mode technique. Initial electromagnetic simulations showed that a ten-fold reduction in electric field strength was possible in a homogeneous head model with an implanted copper wire for a 4-channel pTx MRI. These simulation results were then experimentally verified and translated into negligible temperature elevations at the tip of the copper wire compared to imaging with the pTx coil set in quadrature mode and a standard commercial birdcage coil. The 4-channel pTx RF signal integrity measurements that followed showed that channel-to-channel variations in the system output power could vary by up to 2 dBm in the proposed setup. As a result, it supported the further study of system uncertainty and its effect on the proposed pTx safe mode and DBS device imaging safety.

Electromagnetic simulations demonstrated that for the 4-channel pTx setup when amplitude and phase varied between ± 0.5 dB and 10º, respectively, had a significant impact on the local 1-gram SAR near the wire tip, with simulation results showing over 150 and 300% increases, respectively. Moreover, in a worst-case scenario, it caused simulated temperature elevations of 1.48 ºC at the tip of a wire, which exceeded the present safety guidelines. Similar to the 1-gram SAR results, B_1 homogeneity was also negatively impacted by system uncertainties. Collectively, this led to the investigation of system channel count in Chapter 3 to mitigate some of these effects.

Chapter 3 started with a brief review of multi-channel MRI. A new 8- and 16-channel pTx configuration was then presented. The initial electromagnetic simulation results demonstrated that the proposed safe mode method was not limited to a specific channel count and that significant RF heating minimization could be achieved at both pTx channel counts. When analyzing the worst-case scenario for system uncertainty, it was concluded that the 8-channel pTx setup was the most optimal channel count of the two studied. The data suggested that with the additional signal modulation flexibility at 16 channels, it would be possible to compromise the pTx safe mode of imaging, which resulted in a greater temperature elevation (at the wire tip) than at 4 and 8 channels. Further study of the 8-channel pTx setup showed an improved worst-case system uncertainty result, a temperature elevation of 0.85 ºC, a result that was significantly lower than what was predicted for the 4-channel setup. Similarly, gains in B_1 homogeneity were also observed. As a result, a new 8-channel pTx system design architecture was proposed and described. The proposed pTx coil was then fabricated and benchtop characterized with minimum reflection coefficients and isolation between neighbouring channels of -12 and -8 dB, respectively.

The proposed implant-friendly safe mode technique has limitations that require study. Patient motion is a major concern in MRI, and the safe mode technique is derived from a fixed position in space. Chapter 4 first reviewed the challenges of patient motion and its effect on image reconstruction. This was followed by an electromagnetic simulation study that evaluated static phantom positional changes and their effect on temperature elevation during 4-channel pTx safe mode imaging. The simulation results were then experimentally verified and expanded to include additional positional changes with all temperature change readings under +0.5 ºC, with the exception of a +0.8 ºC temperature rise due to a -50º pitch rotation. Although such rotation is not realistic, the data suggested that it may be possible for the implanted DBS lead(s) to be shifted into

higher electric field zones. The experimental assessment of the pTx safe mode was further tested with clinically relevant pulse sequences, and it was found that the proposed pTx safe mode of imaging outperformed conventional imaging methods in all 10 of the RF heating imaging scenarios tested while maintaining comparable signal-to-noise ratios. Chapter 4 only studied one of the possible DBS lead orientations and did not consider the bilateral case in DBS patients. With conventional phantom structures lacking the physical structures to accommodate such experiments, an improved phantom design was necessary and was the topic of Chapter 5.

Chapter 5 started with a brief review of popular phantom structures, including the standard phantom used for verification experiments and its limitations for DBS applications. An initial study that investigated the heating transfer characteristics between an insulated copper wire and a commercial DBS lead showed that similar temperature heating profiles could be expected. However, the data suggested that DBS leads are better insulated and more resilient to RF heating effects than insulated copper wires, which resulted in the reduced absolute temperature changes observed. As a consequence, it may not be suitable to use copper wire as a substitute in advanced DBS patient safety studies. This led to the design and construction of a new anthropomorphic phantom with improved realism and the ability to better replicate the complex DBS lead trajectories across patients with implanted DBS devices. The RF heating experiments with the new phantom and implanted commercial DBS device showed marked differences in temperature increases when the device was powered on and off and when the phantom was in a homogeneous and heterogeneous configuration. These preliminary results demonstrated the complex nature of DBS device MRI safety, and that improved phantom structures may offer additional insights over conventional methods. The new phantom since its development has been utilized in several recent DBS patient studies [90, 139, 140]. This concluded the thesis, but much more work is required to ensure DBS patient safety at 3 T and beyond. The following section will present some recommendations for immediate and longer-term consideration.

6.2 Future Work

A fully operational 4- and 8-channel pTx MRI system at 3 T approved for DBS patient studies is an ongoing project and is a long-term goal that may take several years to complete.

Several immediate projects based on the work presented in this thesis would greatly contribute to its completion and are listed below.

1. The system uncertainty simulation results will require MRI experimental verification, and particularly the worst-case scenarios.
2. Although the phantom structure is constructed with realistic human features, the electromagnetic properties require validation and should be studied and compared to the present phantom standards to further support using sophisticated phantom structures for DBS applications. This would involve modelling and segmentation of the presented phantom and commercial DBS device to be imported into simulation software application such as FEKO.
3. In effort to advance from phantom to human or DBS patient imaging on the 8-channel pTx system, the full system including the coil will require MRI testing and, eventually, undergo electrical safety testing to be granted Siemens certification. An important initial step to receive research ethics board approval for human testing. A coil enclosure will be an essential part of this process and will require design and development.
4. Patient motion effects will require an additional study that includes using MRI-compatible motors with the new anthropomorphic phantom for improved realism of DBS patient motion. This study will also be expanded to examine the random combination of motion effects with system uncertainty to better mimic actual imaging conditions.
5. Real-time system power monitoring of all pTx channels and calibration procedures also require extensive development along with the implementation of a SAR estimation method to ensure normal system operating conditions and that RF power deposition or SAR remains within the recommended patient safety guidelines. A potential approach to real-time SAR estimation is the use of forward and reverse power measurements that may approximate the power dissipated from the RF coil.
6. The weighting factor, λ (presented in Chapter 1, section 1.5), may be optimized further (i.e., changing λ from 1 to 0.5) to determine if implant heating effects can remain suppressed at lower λ values. The 8-channel pTx system results have shown that improved system optimization opportunities may be possible. This would potentially provide greater gains in B_1 homogeneity (or improved image quality).

DBS patient safety concerns will remain and become increasingly problematic with greater clinical adoption of ultra-high field MRI systems. With promising DBS treatment outcomes for patients with psychiatric/cognitive disorders, the DBS patient population worldwide will continue to experience significant growth. MRI is becoming an indispensable diagnostic tool in the healthcare industry, and DBS MRI safety will be one of the many challenges of the future. The following are three longer-term recommendations for the pTx MRI platform,

1. Compatibility with a 7 T MRI system will inevitably be required, and similar topics presented in this thesis will be repeated to evaluate safety.
2. To enable full pTx mode, a full library of pulse sequences and a user interface will require development. For example, gradient-echo, spin-echo, diffusion-weighted, and echo-planar-based protocols are all commonly used in neuroimaging.
3. The exploration of other possible pTx system channel configurations such as 10 or 12.

References

[1] H. J. Kim, B.S. Jeon, J. Y. Lee, S. H. Paek and D. G. Kim, "The benefit of subthalamic deep brain stimulation for pain in Parkinson disease: a 2-year follow-up study," *Neurosurgery*, 2012;70:18–24.

[2] B. Davidson, P. Giacobbe, T. P. George, S. M. Nestor, J. S. Rabin, M. Goubran, A. J. Nyman, A. Baskaran, Y. Meng, C. B. Pople, S. J. Graham, F. Tam, C. Hamani and N. Lipsman, "Deep brain stimulation of the nucleus accumbens in the treatment of severe alcohol use disorder: a phase I pilot trial," *Mol Psychiatry* 2022. doi.org/10.1038/s41380-022-01677-6.

[3] L. Mallet, M. Polosan, N. Jaafari, N. Baup, M. L. Welter, D. Fontaine, S. T. du Montcel, J. Yelnik, I. Chéreau, C. Arbus, S. Raoul, B. Aouizerate, P. Damier, S. Chabardès, V. Czernecki, C. Ardouin, M. O. Krebs, E. Bardinet, P. Chaynes, P. Burbaud, P. Cornu, P. Derost, T. Bougerol, B. Bataille, V. Mattei, D. Dormont, B. Devaux, M. Vérin, J. L. Houeto, P. Pollak, A. L. Benabid, Y. Agid, P. Krack, B. Millet and A. Pelissolo, "Subthalamic nucleus stimulation in severe obsessive-compulsive disorder," *N Engl J Med.*, 2008;359:2121– 2134.

[4] L. Zrinzo, F. Yoshida, M.I. Hariz, J. Thornton, T. Foltynie, T. A. Yousry and P. Limousin, "Clinical safety of brain magnetic resonance imaging with implanted deep brain stimulation hardware: large case series and review of the literature," *World Neurosurgery*, 2011;76(1-2):164-172; discussion 169-173. doi:10.1016/j.wneu.2011.02.029.

[5] S. Falowski, Y. Safriel, M. P. Ryan and L. Hargens, "The rate of magnetic resonance imaging in patients with deep brain stimulation," *Stereotact. Funct. Neurosurg.*, 2016;94:147–153.

[6] J. A. Nyenhuis, S. -M. Park, R. Kamondetdacha, A. Amjad, F. G. Shellock and A. R. Rezai, "MRI and implanted medical devices: Basic interactions with an emphasis on heating," *IEEE Transactions on Device and Materials Reliability*, 2005;5(3):467-479.

[7] J. M. Bronstein, M. Tagliati, R. L. Alterman, A. M. Lozano, J. Volkmann, and A. Stefani, "Deep brain stimulation for parkinson disease," *Neurological Review*, 2011; 68(2):165-171.

[8] C. A. Davie "A review of Parkinson's disease," *British Medical Bulletin*, 2008;86:109-127.

[9] J. Obeso, M. Rodriguez-Oroz, B. Benitex-Temino, F. J. Blesa, J. Guridi, C. Marin and M. Rodriguez, "Functional organization of the basal ganglia: Therapeutic implications for Parkinson's disease," *Movement Disorders*, 2008;23(3): S548-S559.

[10] J. E. Kennedy, G. R. ter Haar, and D. Cranston, "High intensity focused ultrasound: surgery of the future?" *The British Journal of Radiology*, 2003;6:590-599.

[11] J. A. Obeso, C. W. Olanow, M. C. Rodriguez-Oroz, P. Krack, R. Kumar and A. E. Lang, "Deep-brain stimulation of the subthalamic nucleus or the pars interna of the globus pallidus in Parkinson's disease," *N Engl J Med.* 2001 Sep 27;345(13):956-63.

[12] F. M. Weaver, K. Follett, M. Stern, K. Hur, C. Harris, W. J. Marks Jr, J. Rothlind, O. Sagher, D. Reda, C. S. Moy, R. Pahwa, K. Burchiel, P. Hogarth, E. C. Lai, J. E. Duda, K. Holloway, A. Samii, S. Horn, J. Bronstein, G. Stoner, J. Heemskerk and G. D. Huang, "Bilateral deep brain stimulation vs best medical therapy for patients with advanced Parkinson disease: a randomized controlled trial," *JAMA*, 2009;301(1):63-73. doi:10.1001/jama.2008.929

[13] M. L. Kringelbach, N. Jenkinson, S. L. Owen, and T. Z. Aziz, "Translational principles of deep brain stimulation," *Nature Reviews Neuroscience*, 2007; 8(8): 623-635. doi:10.1038/nrn2196.

[14] D. G. Nishimura, Principles of magnetic resonance imaging. Stanford University, 1996.

[15] Siemens 1.5 T MRI scanner [Online]. Available: https://www.siemens-healthineers.com/magnetic-resonance-imaging/0-35-to-1-5t-mri-scanner. Accessed December 2020.

[16] D. D. Stark and W. G. Bradley, Magnetic resonant imaging, volume 1. Mosby Yearbook, St Louis, 1992.

[17] Standard test method for measurement of magnetically induced displacement force on medical devices in the magnetic resonance environment, ASTM International, West Conshohocken, PA., 2015.

[18] B. Davidson, F. Tam, B. Yang, Y. Meng, C. Hamani, S. J. Graham and N. Lipsman, "Three-tesla magnetic resonance imaging of patients with deep brain stimulators: Results from a phantom study and a pilot study in patients," *Neurosurgery*, 2021;88(2):349-355. doi:10.1093/neuros/nyaa439.

[19] J. S. Perlmutter and J. W. Mink, "Deep brain stimulation," *Annual Review of Neuroscience*, 2006; 29:229-257.

[20] Guidelines on exposure to electromagnetic fields from magnetic resonance clinical systems - Safety Code 26. [Online.] (https://www.canada.ca/en/health-canada/services/publications/health-risks-safety/safety-code-26-guidelines-electromagnetic-fields-magnetic-resonance-clinical-systems-exposure.html.)

[21] J. G. Delfino, D. M. Krainak, S. A. Flesher and D. L. Miller, "MRI-related FDA adverse event reports: A 10-yr review," *Med Phys.* 2019;46(12):5562-5571. doi: 10.1002/mp.13768.

[22] J. Henderson, J. Tkach, M. Phillips, K. Baker, F. G. Shellock and A. R. Rezai, "Permanent neurological deficit related to magnetic resonance imaging in a patient with implanted deep brain stimulation electrodes for Parkinson's disease: a case report," *Neurosurgery* 2005;57(5). doi: 10.1227/01.neu.0000180810.16964.3e

[23] ISO/TS 10974:2018(en), Assessment of the safety of magnetic resonance imaging for patients with an active implantable medical device. [Online.] (https://www.iso.org/obp/ui/en/#iso:std:iso:ts:10974:ed-2:v1:en) Accessed December 2023.

[24] A. R. Rezai, D. Finelli, J. A. Nyenhuis, G. Hrdlicka, J. Tkach, A. Sharan, P. Rugieri, P. H. Stypulkowski and F. G. Shellock, "Neurostimulation systems for deep brain stimulation: In vitro evaluation of magnetic resonance imaging-related heating at 1.5 tesla," *Journal of Magnetic Resonance Imaging*, 2002;15:241-250.

[25] P. Nordbeck, F. Fidler, I. Weiss, M. Warmuth, M. T. Friedrich, P. Ehses, W. Geistert, O. Ritter, P. M. Jakob, M. E. Ladd, H. H. Quick and W. Bauer, "Spatial distribution of RF-induced E-fields and implant heating in MRI," *Magn. Reson. Med.* 2008;60(2):312-319. doi:10.1002/mrm.21475.

[26] D. Shrivastava, A. Abosch, T. Hanson, J. Tian, A. Gupte, P. A. Iaizzo and J. T. Vaughan, "Effect of the extracranial deep brain stimulation lead on radiofrequency heating at 9.4 Tesla (400.2 MHz)," *Journal of magnetic resonance imaging*, 2010;32 (3):600-607. doi:10.1002/jmri.22292.

[27] M. K. Konings, L. W. Bartels, H. F. Smits, and C. J. Bakker, "Heating around intravascular guidewires by resonating RF waves," *Journal of Magnetic Resonance Imaging*, 2000;12:79-85.

[28] W. R. Nitz, A. Oppelt, W. Renz, C. Manke, M. Lenhart and J. Link, "On the heating of linear conductive structures as guide wires and catheters in interventional MRI," *Journal of Magnetic Resonance Imaging*, 2001;13:105-114.

[29] C. J. Yeung, R. C. Susil and E. Atalar, "RF heating due to conductive wires during MRI depends on the phase distribution of the transmit field," *Magn. Reson. Med.*, 2002;48(6):1096-1098. doi:10.1002/mrm.10310.

[30] B. Guerin, L. Angelone, D. Dougherty, and L. Wald, "Parallel transmission to reduce absorbed power around deep brain stimulation devices in MRI: Impact of number and arrangement of transmit channels," Magn Reson Med., 2020;83:299–311.

[31] C. E. McElcheran, B. Yang, K. J. T. Anderson, L. Golestanirad, S. J. Graham, "Parallel radiofrequency transmission at 3 tesla to improve safety in bilateral implanted wires in a heterogeneous model," *Magn Reson Med.*, 2017;78(6):2406-2415.

[32] E. Kazemivalipour, B. Keil, A. Vali, S. Rajan, B. Elahi, E. Atalar, L. L. Wald, J. Rosenow, J. Pilitsis and L. Golestanirad, "Reconfigurable MRI technology for low-SAR imaging of deep brain stimulation at 3T: Application in bilateral leads, fully-implanted systems, and surgically modified lead trajectories," *NeuroImage*, 2019;199:18–29.

[33] R. Das and H. Yoo, "RF heating study of a new medical implant lead for 1.5 T, 3 T, and 7 T MRI systems," *IEEE Trans. Electromagn. Compat.*, 2017; 59(2):360-366.

[34] L. Golestanirad, J. Kirsch, G. Bonmassar, S. Downs, B. Elahi, A. Martin, M. I. Iacono, L. M. Angelone, B. Keil, L. L. Wald and J. Pilitsis, "RF-induced heating in tissue near bilateral DBS implants during MRI at 1.5 T and 3T: The role of surgical lead management," *NeuroImage*, 2019;184:566-576.

[35] C. E. McElcheran, B. Yang, K. J. Anderson, L. Golenstani-Rad and S. J. Graham, "Investigation of parallel radiofrequency transmission for the reduction of heating in long conductive leads in 3 tesla magnetic resonance imaging," *PLoS ONE*, 2015;10:e0134379.

[36] A. T. Curtis, K. M. Gilbert, L. M. Klassen, J. S. Gati, and R. S. Menon, "Slice-by-slice B1+ shimming at 7 T," *Magn. Reson. Med.*, 2012;68(4):1109-1116. doi:10.1002/mrm.23319.

[37] B. Yang, P. S. Wei, C. E. McElcheran, F. Tam and S. J. Graham, "A platform for 4-channel parallel transmission MRI at 3 T: Demonstration of reduced radiofrequency heating in a test object containing an implanted wire," *J. Med. Biol. Eng.* 2019. https://doi.org/10.1007/s40846-019-00478-7

[38] G. Ferrand, M. Luong, A. Amadon, M. A. Cloos, E. Giacomini and L. Darrasse, "Generalized double-acquisition imaging for radiofrequency inhomogeneity mitigation in high-field MRI: experimental proof and performance analysis," *Magn. Reson. Med.*, 2012;67(1):175-182. doi:10.1002/mrm.23006.

[39] U. Katscher, P. Bornert, C. Leussler, and J. S. van den Brink, “Transmit SENSE,” *Magn. Reson. Med.*, 2003;49(1):144-150. doi:10.1002/mrm.10353

[40] P. Ullman, S. Junge, M. Wick, F. Seifert, W. Ruhm and J. Hennig, "Experimental analysis of parallel excitation using dedicated coil setups and simultaneous RF transmission on multiple channels," *Magn. Reson. Med.*, 2005;54:994–1001.

[41] W. Grissom, C.-Y. Yip, and D. Noll, "A new method for the design of RF pulses in Transmit SENSE," *Proceedings of the 2nd International Workshop on Parallel Imaging*, Zurich, Switzerland, 2004, p 95.

[42] P. G. Huray, Maxwell's Equations. Wiley-IEEE Press. 2009.

[43] C. A. Balanis, Antenna Theory: Analysis and Design (3rd ed.) 2005.

[44] C. E. McElcheran, L. Golestanirad, M. I. Iacono, P. S. Wei, B. Yang, K. J. T. Anderson, G. Bonmassar and S. J. Graham, "Numerical simulations of realistic lead trajectories and an experimental verification support the efficacy of parallel radiofrequency transmission to reduce heating of deep brain stimulation implants during MRI," *Sci Rep*, 2019;9:2124.

[45] R. F. Harrington, Field Computation by Moment Method, New York, IEEE Press, 1968, 1993.

[46] H. H. Pennes, "Analysis of tissue and arterial blood temperatures in the resting human forearm," *J Appl Physiol.*, 1948;1:93–122.

[47] A. Taflove, Computational Electrodynamics: The Finite-Difference Time-Domain Method, vol 3. Artech House, Boston, 2005.

[48] B. Yang, P. S. Wei, C. E. McElcheran, F. Tam and S. J. Graham, "A platform for 4-channel parallel transmission MRI at 3 T: Demonstration of reduced radiofrequency heating in a test object containing an implanted wire," *J. Med. Biol. Eng.* 2019, vol. 39(6), pp. 835-844. doi: 10.1007/s40846-019-00478-7

[49] J. T. Vaughan and J. R. Griffiths, RF Coils for MRI, Wiley 2012.

[50] B. Yang, F. Tam, C. Leone, V. Li, J. Rock and S. J. Graham, "A modular parallel radiofrequency transmission system platform for MRI safety investigations at 3 T", *Proc. 31th scientific meeting, Intl. Soc. Mag. Reson. Med.*, Toronto, 2023, p.2869.

[51] P. S. Wei, B. Yang, C. E. McElcheran, L. Golestanirad and S. J. Graham, "Reducing radiofrequency-induced heating in realistic deep brain stimulation lead trajectories using parallel transmission," *Proc. 26th scientific meeting, Intl. Soc. Mag. Reson. Med.,* Paris, France, 2018, p. 0638.

[52] M. Twieg, B. Mehta, S. Coppo, J. Ruff, R. Gumbrecht and M. A. Griswold, "A 16 channel head-only pTX array using high efficiency in-bore RFPAs at 3T," *Proc. 25th scientific meeting, Intl. Soc. Mag. Reson. Med.*, Honolulu, USA, 2017, p. 1054.

[53] F. E. Filci, A. Dogan, G. Cansiz, B. Sen, V. Acikel and E. Atalar, "Prototype hardware of FPGA controlled multi-channel all-digital RF transmitter for parallel magnetic resonance imaging," *Proc. 25th scientific meeting, Intl. Soc. Mag. Reson. Med.*, Honolulu, USA, 2017, p. 4347.

[54] L. Fickman, New discoveries of deep brain stimulation put it on par with therapeutics, https://uh.edu/news-events/stories/2021/march-2021/03252021-nuri-ince-deep-brain-stimulation-parkinsons.php. Accessed October 20, 2021.

[55] B. Davidson, F. Tam, B. Yang, Y. Meng, C. Hamani, S. J. Graham and N. Lipsman, "Three-tesla magnetic resonance imaging of patients with deep brain stimulators: Results from a phantom study and a pilot study in patients," *Neurosurgery*, 2021;88(2):349-355. doi:10.1093/neuros/nyaa439.

[56] C. E. McElcheran, B. Yang, K. J. T. Anderson, L. Golestanirad, S. J. Graham, "Parallel radiofrequency transmission at 3 tesla to improve safety in bilateral implanted wires in a heterogeneous model," *Magn Reson Med.*, 2017;78(6):2406-2415.

[57] H. H. Pennes, "Analysis of tissue and arterial blood temperatures in the resting human forearm," *Journal of Applied Physiology*, 1948 1:2, 93-122

[58] Y. Seo and Z. J. Wang, "MRI scanner-independent specific absorption rate measurements using diffusion coefficients," *J Appl Clin Med Phys.* 2017;18(4):224-229. doi:10.1002/acm2.12095.

[59] Medtronic Inc. MRI guidelines for Medtronic deep brain stimulation systems 2015. http://mriquestions.com/uploads/3/4/5/7/34572113/dbs_medtronics_contrib_228155.pdf. Accessed October 20, 2021.

[60] S. M. Sohn, L. DelaBarre, J. T. Vaughan and A. Gopinath, "RF multi-channel head coil design with improved B1+ Fields uniformity for high field MRI systems," 2012 *IEEE/MTT-S International Microwave Symposium Digest*, Montreal, QC, 2012, pp. 1-3, doi: 10.1109/MWSYM.2012.6259669.

[61] A. Deshmane, V. Gulani, M. A. Griswold and N. Seiberlich, "Parallel MR imaging," *J. Magn. Reson. Imaging*, 2012;36: 55-72. https://doi.org/10.1002/jmri.23639.

[62] J. M. Slipsager, S. L. Glimberg, J. Søgaard, R. R. Paulsen, H. H. Johannesen, P. C. Martens, A. Seth, L. Marner, O. M. Henriksen, O. V. Olesen and L. Højgaard, "Quantifying the financial savings of motion correction in brain MRI: A model-based estimate of the costs arising from patient head motion and potential savings from implementation of motion correction," *J. Magn. Reson. Imaging*, 2020;52:731–738.

[63] D. K. Sodickson and W. J. Manning, "Simultaneous acquisition of spatial harmonics (SMASH): fast imaging with radiofrequency coil arrays," *Magn Reson Med.* 1997;38(4):591-603. doi:10.1002/mrm.1910380414

[64] S. N. Williams, P. McElhinney and S. Gunamony, "Ultra-high field MRI: parallel-transmit arrays and RF pulse design," *Phys. Med. Biol.*, 2023;68,02TR02

[65] E. M. Lawrence, Y. Zhang, J. Starekova, Z. Wang, A. Pirasteh, S. A. Wells and D. Hernando, "Reduced field-of-view and multi-shot DWI acquisition techniques: Prospective evaluation of image quality and distortion reduction in prostate cancer imaging," *Magn Reson Imaging*. 2022;93:108-114. doi:10.1016/j.mri.2022.08.008

[66] M. Barth, F. Breuer, P.J. Koopmans, D. G. Norris and B. A. Poser "Simultaneous multi-slice (SMS) imaging techniques," *Magn Reson Med*. 2016;75(1):63-81. doi:10.1002/mrm.25897

[67] H. Fujita, "New horizons in MR technology: RF coil designs and trends," *Magn Reson Med Sci*, 2007;6(1), pp. 29–42.

[68] P. Nordbeck, F. Fidler, I. Weiss, M. Warmuth, M. T. Friedrich, P. Ehses, W. Geistert, O. Ritter, P. M. Jakob, M. E. Ladd, H. H. Quick and W. R. Bauer, "Spatial distribution of RF induced e-fields and implant heating in MRI," *Magn. Reson. Med.*, 2008;60, pp. 312–319.

[69] Medtronic Inc. 2020. FDA approves first-of-its-kind Percept™ PC neurostimulator with BrainSense™ technology. https://newsroom.medtronic.com/news-releases/news-release-details/fda-approves-first-its-kind-percepttm-pc-neurostimulator Accessed 10 March 2021.

[70] B. Davidson, F. Tam, B. Yang, Y. Meng, C. Hamani, S. J. Graham and N. Lipsman, "3-Tesla MRI of patients with deep brain stimulators: Results from a phantom study and a pilot study in patients," *Neurosurgery*, 2021;88(2), pp. 349-355.

[71] A. Boutet, I. Hancu, U. Saha, A. Crawley, D. S. Xu, M. Ranjan, E. Hlasny, R. Chen, W. Foltz, F. Sammartino, A. Coblentz, W. Kucharczyk and A. M. Lozano, "3-Tesla MRI of deep brain stimulation patients: safety assessment of coils and pulse sequences," *J. Neurosurg.*, 2019;132(2), pp. 586-594.

[72] A. L. Benabid, S. Chabardes, J. Mitrofanis and P. Pollak, "Deep brain stimulation of the subthalamic nucleus for the treatment of Parkinson's disease," *Lancet Neurol.*, 2009; 8, pp. 67-81.

[73] Medtronic Inc. 2020. Medtronic receives Health Canada license for the first-of-its-kind Percept™ PC neurostimulator with BrainSense™ Technology. https://www.medtronic.com/ca-en/about/news/percept-dbs.html. Accessed 11 May 2021.

[74] B. Yang, P. S. Wei, C. E. McElcheran, F. Tam and S. J. Graham, "A platform for 4-channel parallel transmission MRI at 3T: Demonstration of reduced radiofrequency heating in a test object containing an implanted wire," *J. Med. Biol. Eng.* 2019;39(6), pp. 835-844. doi: 10.1007/s40846-019-00478-7

[75] C. E. McElcheran, B. Yang, K. J. T. Anderson, L. Golenstani-Rad and S. J. Graham, "Investigation of parallel radiofrequency transmission for the reduction of heating in long conductive leads in 3Tesla magnetic resonance imaging," *PLoS ONE*, 2015;10(8), pp. e0134379.

[76] B. Yang, C. H. Chen and S. J. Graham, "RF heating dependence of head model positioning using 4-channel parallel transmission MRI and a deep brain stimulation construct," *IEEE Letters on Electromagnetic Compatibility Practice and Applications*, 2022; doi: 10.1109/LEMCPA.2022.3180974.

[77] B. Yang, F. Tam, B. Davidson, C. Hamani, N. Lipsman, C. H. Chen and S. J. Graham, "MRI safety of deep brain stimulation devices: Radiofrequency heating of a commercial

lead and an insulated copper wire," *Proc. Int. Soc. Magn. Reson. Med.* 28., Virtual, 2020, p. 4182.

[78] H. H. Pennes, "Analysis of tissue and arterial blood temperatures in the resting human forearm," *J. Appl Physiol.* 1948;1, pp. 93–122.

[79] Y. Seo and Z. J. Wang, "MRI scanner-independent specific absorption rate measurements using diffusion coefficients," *J. Appl. Clin. Med. Phys.*, 2017;18:224-229.

[80] C.E. McElcheran, L. Golestanirad, M. I. Iacono, P. S. Wei, B. Yang, K. J. T. Anderson, G. Bonmassar and S. J. Graham, "Numerical simulations of realistic lead trajectories and an experimental verification support the efficacy of parallel radiofrequency transmission to reduce heating of deep brain stimulation implants during MRI," *Scientific reports*, 2019;9(1), 1-14.

[81] A. S. Childs, S. J. Malik, D. P. O'Regan and J. V. Hajnal, "Impact of number of channels on RF shimming at 3T," *Magn. Reson. Mater. Phy.* 2013;26, 401–410.

[82] B. Yang, F. Tam, B. Davidson, P. S. Wei, C. Hamani, N. Lipsman, C. H. Chen and S. Graham, "Technical note: An anthropomorphic phantom with implanted neurostimulator for investigation of MRI safety," *Med. Phys.* 2020;47(8), 3745-3751.

[83] B.Yang, F. Tam, M. Arianpouya, C. Leone, V. Li, J. Rock and S. Graham, "A modular parallel radiofrequency transmission system platform for MRI safety investigations at 3 T," *Proc. Int. Soc. Magn. Reson. Med.* 31., Toronto, Canada, 2023, p. 2869.

[84] K. Bötzel, V. Tronnier, and T. Gasser, "The differential diagnosis and treatment of tremor," *Dtsch Arztebl Int.* 2014;111(13):225-236. doi:10.3238/arztebl.2014.0225.

[85] Medtronic Inc. MRI guidelines for Medtronic deep brain stimulation systems 2015. http://mriquestions.com/uploads/3/4/5/7/34572113/dbs_medtronics_contrib_228155.pdf.

[86] Medicines and Healthcare Products Regulatory Agency. Safety guidelines for magnetic resonance imaging equipment in clinical use 2014. https://www.gov.uk/government/publications/safety-guidelines-for-magnetic-resonance-imaging-equipment-in-clinical-use.

[87] J. Maclaren, M. Herbst, O. Speck, and M. Zaitsev, "Prospective motion correction in brain imaging: A review," *Magn. Reson. Med*. 2013;69: 621-636. https://doi.org/10.1002/mrm.24314

[88] Medtronic Inc. (2020), Medtronic receives CE Mark approval for the Percept™ PC neurostimulator DBS system with BrainSense™ technology. https://newsroom.medtronic.com/news-releases/news-release-details/medtronic-receives-ce-mark-approval-percepttm-pc-neurostimulator Accessed 10 March 2021.

[89] Medtronic Inc. (2020), FDA approves first-of-its-kind Percept™ PC neurostimulator with BrainSense™ technology. https://newsroom.medtronic.com/news-releases/news-release-details/fda-approves-first-its-kind-percepttm-pc-neurostimulator Accessed 10 March 2021.

[90] B. Davidson, F. Tam, B. Yang, Y. Meng, C. Hamani, S. J. Graham and N. Lipsman, "3-Tesla MRI of patients with deep brain stimulators: Results from a phantom study and a pilot study in patients," *Neurosurgery*, 2021; vol. 88(2), pp. 349-355.

[91] A. Boutet, I. Hancu, U. Saha, A. Crawley, D. S. Xu, M. Ranjan, E. Hlasny, R. Chen, W. Foltz, F. Sammartino, A. Coblentz, W. Kucharczyk and A. M. Lozano, "3-Tesla MRI of deep brain stimulation patients: safety assessment of coils and pulse sequences," J *Neurosurg*, 2019;vol. 132(2), pp. 586-594.

[92] R. Das and H. Yoo, "RF heating study of a new medical implant lead for 1.5 T, 3 T, and 7 T MRI systems," *IEEE Trans. Electromagn. Compat.*, 2017;vol. 59, no. 2, pp. 360-366.

[93] C. E. McElcheran, B. Yang, K. J. T. Anderson, L. Golenstani-Rad and S. J. Graham, "Investigation of parallel radiofrequency transmission for the reduction of heating in long conductive leads in 3 Tesla magnetic resonance imaging," *PLoS ONE*, 2015;vol. 10, issue 8, pp. e0134379.

[94] A. Boutet, T. Rashid, I. Hancu, G. J. B. Elias, R. M. Gramer, J. Germann, M. Dimarzio, B. Li, V. Paramanandam, S. Prasad, M. Ranjan, A. Coblentz, D. Gwun, C. T. Chow, R. Maciel, D. Soh, E. Fiveland, M. Hodaie, S.K. Kalia, A. Fasano, W. Kucharczyk, J. Pilitsis

and A. M. Lozano, "Functional MRI safety and artifacts during deep brain stimulation: Experience in 102 patients," *Radiology*, 2019;vol. 293(1), pp. 174–183.

[95] B. Yang, P.S. Wei, C. E. McElcheran, F. Tam and S. J. Graham, "A platform for 4-channel parallel transmission MRI at 3 T: Demonstration of reduced radiofrequency heating in a test object containing an implanted wire," *J. Med. Biol. Eng*. 2019;vol. 39(6), pp. 835-844. doi: 10.1007/s40846-019-00478-7

[96] H. H. Pennes, "Analysis of tissue and arterial blood temperatures in the resting human forearm," *J Appl Physiol.* 1948;vol. 1, pp. 93–122.

[97] B. Yang, P. S. Wei and S. J. Graham, "Parallel RF transmission for safe 3 T MRI of deep brain stimulation devices: Effect of mis-positioned suppression mode," Proc. 27th scientific meeting, *Intl. Soc. Mag. Reson. Med.*, Montreal, 2019, p. 4181.

[98] C. J. Wargo, J. Moore and J. C. Gore, "A comparison and evaluation of reduced-FOV methods for multi-slice 7 Tesla human imaging," *Magn. Reson. Imaging* 2013;31(8):1349–1359.

[99] B. Bhusal, J. Stockmann, B. Guerin, A. Mareyam, J. Kirsch, L. L. Wald, M. J. Nolt, J. Rosenow, R. Lopez-Rosado, B. Elahi and L. Golestanirad, "Safety and image quality at 7T MRI for deep brain stimulation systems: Ex vivo study with lead-only and full-systems," *PLoS ONE* 2021;16(9):e0257077.

[100] B. Yang, F. Tam, B. Davidson, P. S. Wei, C. Hamani, N. Lipsman, C. -H. Chen and S. J. Graham, "Technical note: An anthropomorphic phantom with implanted neurostimulator for investigation of MRI safety," *Med. Phys*., 2020;47(8):3745-3751.

[101] L. P. Panych and B. Madore, "The physics of MRI safety," *J Magn Reson Imaging*, 2018;47(1):28-43.doi:10.1002/jmri.25761.

[102] M. J. Firbank, A. Coulthard, R. M. Harrison and E. D. Williams, "A comparison of two methods for measuring the signal to noise ratio on MR images," *Phys. Med. Biol.*, 1999;44:261-264.

[103] B. Yang, F. Tam, C. McElcheran and S. J. Graham, "Another alternate integrated circuit approach to modulation of radiofrequency transmission signals in magnetic resonance imaging," *Concepts Magn. Reson. Part B.* 2018;47B:e21359. https://doi.org/10.1002/cmr.b.21359

[104] ASTM International. ASTM F2182–02 Standard test method for measurement of radio frequency induced heating on or near passive implants during magnetic resonance imaging. https://www.astm.org. Accessed October 23, 2019.

[105] C. Favazza, D. King, H. Edmonson, J. P. Felmlee, P. J. Rossman, N. J. Hangiandreou, R. E. Watson and K. R. Gorny, "Use of a radio frequency shield during 1.5 and 3.0 Tesla magnetic resonance imaging: experimental evaluation," *Medical devices* 2014;7:363-70. 10.2147/MDER.S68657.

[106] P. Ehses, F. Fidler, P. Nordbeck, E. D. Pracht, M. Warmuth, P. M. Jakob and W. R. Bauer, "MRI thermometry: Fast mapping of RF-induced heating along conductive wires," *Magn. Reson. Med.*, 2008;60:457-461. https://doi.org/10.1002/mrm.21417

[107] G. Bonmassar and P. Serano "MRI-induced heating of coils for microscopic magnetic stimulation at 1.5 Tesla: An initial study," *Frontiers in Human Neuroscience*, 2020;14. 10.3389/fnhum.2020.00053.

[108] A. Boutet, C. T. Chow, K. Narang, G. J. B. Elias, C. Neudorfer, J. Germann, M. Ranjan, A. Loh, A. J. Martin, W. Kucharczyk, C. J. Steele, I. Hancu, A. R. Rezai and A. M. Lozano, "Improving safety of MRI in patients with deep brain stimulation devices," *Radiology*, 2020;296:2, 250-262.

[109] C. E. McElcheran, L. Golestanirad, M. I. Iacono, P. S. Wei, B. Yang, K. J. T. Anderson, G. Bonmassar and S. J. Graham, "Numerical simulations of realistic lead trajectories and an experimental verification support the efficacy of parallel radiofrequency transmission to reduce heating of deep brain stimulation implants during MRI," *Sci Rep*, 2019;9:2124.

[110] L. Golestanirad, J. Kirsch, G. Bonmassar, S. Downs, B. Elahi, A. Martin, M. I. Iacono, L. M. Angelone, B. Keil, L. L. Wald and J. Pilitsis, "RF-induced heating in tissue near

bilateral DBS implants during MRI at 1.5 T and 3T: the role of surgical lead management," *NeuroImage*, 2019;184:566–576.

[111] B. Guerin, L. Angelone, D. Dougherty, and L. Wald, "Parallel transmission to reduce absorbed power around deep brain stimulation devices in MRI: impact of number and arrangement of transmit channels," *Magn Reson Med.*, 2020;83:299–311.

[112] B. Bhusal, J. Stockmann, B. Guerin, A. Mareyam, J. Kirsch, L. L. Wald, M. J. Nolt, J. Rosenow, R. Lopez-Rosado, B. Elahi and L. Golestanirad, "Safety and image quality at 7T MRI for deep brain stimulation systems: Ex vivo study with lead-only and full-systems," *PLoS ONE*, 2021;16(9): e0257077. https://doi.org/10.1371/journal.pone.0257077

[113] J. Kahan, A. Papadaki, M. White, L. Mancini, T. Yousry, L. Zrinzo, P. Limousin, M. Hariz, T. Foltynie and J. Thornton, "The safety of using body-transmit MRI in patients with implanted deep brain stimulation devices," *PLoS ONE*, 2015;10:e0129077.

[114] C. E. McElcheran, B. Yang, K. J. Anderson, L. Golenstani-Rad and S. J. Graham, "Investigation of parallel radiofrequency transmission for the reduction of heating in long conductive leads in 3 tesla magnetic resonance imaging," *PLoS ONE*, 2015;10:e0134379.

[115] H. J. Kim, B.S. Jeon, J. Y. Lee, S. H. Paek and D. G. Kim, "The benefit of subthalamic deep brain stimulation for pain in Parkinson disease: a 2-year follow-up study," *Neurosurgery*, 2012;70:18–24.

[116] J. L. Ostrem, C.A. Racine, G. A. Glass, J. K. Grace, M. M. Volz, S. L. Heath and P. A. Starr, "Subthalamic nucleus deep brain stimulation in primary cervical dystonia," *Neurology*, 2011;76:870–878.

[117] L. Mallet, M. Polosan, N. Jaafari, N. Baup, M. L. Welter, D. Fontaine, S. T. du Montcel, J. Yelnik, I. Chéreau, C. Arbus, S. Raoul, B. Aouizerate, P. Damier, S. Chabardès, V. Czernecki, C. Ardouin, M. O. Krebs, E. Bardinet, P. Chaynes, P. Burbaud, P. Cornu, P. Derost, T. Bougerol, B. Bataille, V. Mattei, D. Dormont, B. Devaux, M. Vérin, J. L. Houeto, P. Pollak, A. L. Benabid, Y. Agid, P. Krack, B. Millet and A. Pelissolo, "Subthalamic nucleus stimulation in severe obsessive-compulsive disorder," *N Engl J Med.*, 2008;359:2121– 2134.

[118] T. E. Schlaepfer, M. X. Cohen, C. Frick, M. Kosel, D. Brodesser, N. Axmacher, A. Y. Joe, M. Kreft, D. Lenartz and V. Sturm, "Deep brain stimulation to reward circuitry alleviates anhedonia in refractory major depression," *Neuropsychopharmacology*, 2008;33:368–377.

[119] A. L. Benabid, S. Chabardes, J. Mitrofanis, and P. Pollak, "Deep brain stimulation of the subthalamic nucleus for the treatment of Parkinson's disease," *Lancet Neurol.*, 2009;8:67–81.

[120] H. K. Min, S. C. Hwang, M. P. Marsh, I. Kim, E. Knight, B. Striemer, J. P. Felmlee, K. M. Welker, C. D. Blaha, S. Y. Chang, K. E. Bennet and K. H. Lee, "Deep brain stimulation induces BOLD activation in motor and non-motor networks: an fMRI comparison study of STN and EN/GPi DBS in large animals," *NeuroImage*, 2012;63:1408–1420.

[121] A. Amjad, R. Kamondetdacha, A.V. Kildishev, S. M. Park and J. A. Nyenhuis, "Power deposition inside a phantom for testing of MRI heating," *IEEE Trans Magn.* 2005;41:4185–4187.

[122] D. W. Carmichael, S. Pinto, P. Limousin-Dowsey, S. Thobois, P. J. Allen, L. Lemieux, T. Yousry and J. S. Thornton, "Functional MRI with active, fully implanted, deep brain stimulation systems: safety and experimental confounds," *NeuroImage*, 2007;37:508–517.

[123] R. Yang, J. Zheng, W. Kainz, and J. Chen, "Numerical investigations of MRI RF-induced heating for external fixation device in TEM and birdcage body coils at 3 T," *IEEE Trans Electromagn Compat.*, 2018;60:598–604.

[124] C. E. McElcheran, B. Yang, K. J. T. Anderson, L. Golestanirad, and S. J. Graham, "Parallel radiofrequency transmission at 3 Tesla to improve safety in bilateral implanted wires in a heterogeneous model," *Magn Reson Med.* 2017;78:2406–2415.

[125] E. Kazemivalipour, B. Keil, A. Vali, S. Rajan, B. Elahi, E. Atalar, L. L. Wald, J. Rosenow, J. Pilitsis and L. Golestanirad, "Reconfigurable MRI technology for low-SAR imaging of deep brain stimulation at 3T: application in bilateral leads, fully-implanted systems, and surgically modified lead trajectories," *NeuroImage*, 2019;199:18–29.

[126] A. Boutet, I. Hancu, U. Saha, A. Crawley, D. S. Xu, M. Ranjan, E. Hlasny, R. Chen, W. Foltz, F. Sammartino, A. Coblentz, W. Kucharczyk and A. M. Lozano, "3-Tesla MRI of

deep brain stimulation patients: safety assessment of coils and pulse sequences," *J. Neurosurg*, 2019;1–9.

[127] A. T. Mobashsher and A. M. Abbosh, "Three-dimensional human head phantom with realistic electrical properties and anatomy," *IEEE Antennas Wireless Propag Lett.*, 2014;13:1401–1404.

[128] M. J. Burfeindt, T. J. Colgan, R. O. Mays, J. D. Shea, N. Behdad, B. D. Van Veen and S. C. Hagness, "MRI-derived 3-D-printed breast phantom for microwave breast imaging validation," *IEEE Antennas Wireless Propag Lett.*, 2012;11:1610–1613.

[129] B. Yang, P.-S. Wei, C. E. McElcheran, F. Tam, and S. J. Graham, "A platform for 4-channel parallel transmission MRI at 3 T: demonstration of reduced radio frequency heating in a test object containing an implanted wire," *J Med Biol Eng.* 2019;39:835–844.

[130] V. Acikel and E. Atalar, "Modeling of radio-frequency induced currents on lead wires during MR imaging using a modified transmission line method," *Med Phys.*, 2011;38:6623–6632.

[131] A. A. Gupte, D. Shrivastava, M. A. Spaniol, and A. Abosch, "MRI-related heating near deep brain stimulation electrodes: more data are needed," *Stereotact Funct Neurosurg.*, 2011;89:131–140.

[132] H. H. Pennes, "Analysis of tissue and arterial blood temperatures in the resting human forearm," *J Appl Physiol.*, 1948;1:93–122.

[133] ITIS Foundation. Dielectric Properties. https://itis.swiss/virtual-population/tissue-properties/database/dielectric-properties. Accessed October 23, 2019.

[134] M. Lazebnik, E. L. Madsen, G. R. Frank, and S. C. Hagness, "Tissue-mimicking phantom materials for narrowband and ultrawideband microwave applications," *Phys Med Biol.*, 2005;50:4245–4258.

[135] Medtronic Inc. MRI guidelines for Medtronic deep brain stimulation systems 2015. http://mriquestions.com/uploads/3/4/5/7/34572113/dbs_medtronics_contrib_228155.pdf. Accessed October 23, 2019.

[136] Medicines and Healthcare Products Regulatory Agency. Safety guidelines for magnetic resonance imaging equipment in clinical use 2014. https://www.gov.uk/government/publications/safety-guidelines-for-magnetic-resonance-imaging-equipment-in-clinical-use. Accessed October 23, 2019.

[137] S. Raymaekers, L. Luyten, C. Bervoets, L. Gabriels, and B. Nuttin, "Deep brain stimulation for treatment-resistant major depressive disorder: a comparison of two targets and long-term follow-up," *Transl Psychiatry*, 2017;7: e1251.

[138] B. Guerin, L. Angelone, D. Dougherty, and L. Wald, "Parallel transmission to reduce absorbed power around deep brain stimulation devices in MRI: impact of number and arrangement of transmit channels," *Magn Reson Med.*, 2020;83:299–311.

[139] C. T. Chow, S. Kashyap, B. Yang, J. Germann, B. Santyr, A. Naheed, M. Colditz, S. Varughese, N. Owsicki, S. Graham, A. Boutet, K. Uludağ and A. M. Lozano, "Optimizing fMRI parameters to minimize artifacts induced by implanted DBS systems," *Organization for Human Brain Mapping*, Montreal, Canada, 2023. p.1356

[140] C. T. Chow, C. Sarica, B. Yang, K. Pourhossein, A. Naheed, S. Graham and M. Hodaie, "Assessment of MR safety parameters for peripheral field stimulation for facial pain," *International Neuromodulation Society*, Vancouver, Canada, 2024. – *submitted Oct 2023*

Appendix I – Copyright Permission

RF Heating Dependence of Head Model Positioning Using 4-Channel Parallel Transmission MRI and a Deep Brain Stimulation Construct

Author: Benson Yang

Publication: IEEE Letters on Electromagnetic Compatibility Practice and Applications

Publisher: IEEE

Date: September 2022

Thesis / Dissertation Reuse

The IEEE does not require individuals working on a thesis to obtain a formal reuse license, however, you may print out this statement to be used as a permission grant:

Requirements to be followed when using any portion (e.g., figure, graph, table, or textual material) of an IEEE copyrighted paper in a thesis:

1) In the case of textual material (e.g., using short quotes or referring to the work within these papers) users must give full credit to the original source (author, paper, publication) followed by the IEEE copyright line © 2011 IEEE.

2) In the case of illustrations or tabular material, we require that the copyright line © [Year of original publication] IEEE appear prominently with each reprinted figure and/or table.

3) If a substantial portion of the original paper is to be used, and if you are not the senior author, also obtain the senior author's approval.

Requirements to be followed when using an entire IEEE copyrighted paper in a thesis:

1) The following IEEE copyright/ credit notice should be placed prominently in the references: © [year of original publication] IEEE. Reprinted, with permission, from [author names, paper title, IEEE publication title, and month/year of publication]

2) Only the accepted version of an IEEE copyrighted paper can be used when posting the paper or your thesis on-line.

3) In placing the thesis on the author's university website, please display the following message in a prominent place on the website: In reference to IEEE copyrighted material which is used with permission in this thesis, the IEEE does not endorse any of [university/educational entity's name goes here]'s products or services. Internal or personal use of this material is permitted. If interested in reprinting/republishing IEEE copyrighted material for advertising or promotional purposes or for creating new collective works for resale or redistribution, please go to

http://www.ieee.org/publications_standards/publications/rights/rights_link.html to learn how to obtain a License from RightsLink.

If applicable, University Microfilms and/or ProQuest Library, or the Archives of Canada may supply single copies of the dissertation.

JOHN WILEY AND SONS LICENSE TERMS AND CONDITIONS

Aug 25, 2023

This Agreement between Benson Yang ("You") and John Wiley and Sons ("John

Wiley and Sons") consists of your license details and the terms and conditions

provided by John Wiley and Sons and Copyright Clearance Center.

License Number 5616001189126

License date Aug 25, 2023

Licensed Content

Publisher John Wiley and Sons

Licensed Content

Publication Medical Physics

Licensed Content

Title **Technical Note: An anthropomorphic phantom with implanted neurostimulator for investigation of MRI safety**

Licensed Content

Author Benson Yang, Fred Tam, Benjamin Davidson, et al

Licensed Content

Date May 25, 2020

Licensed Content

Volume 47

Licensed Content

Issue 8

Licensed Content

Pages 7

Type of use Dissertation/Thesis

Requestor type Author of this Wiley article

Format Electronic

Portion Full article

Will you be translating? No

Title PhD Thesis

Institution name McMaster University

Expected presentation date Dec 2023

Requestor Location Benson Yang 2075 Bayview Avenue, S652a Toronto, ON M4N 3M5 Canada Attn: Benson Yang

Publisher Tax ID EU826007151

Total 0.00 USD

JOHN WILEY AND SONS LICENSE TERMS AND CONDITIONS

Aug 25, 2023

This Agreement between Benson Yang ("You") and John Wiley and Sons ("John

Wiley and Sons") consists of your license details and the terms and conditions

provided by John Wiley and Sons and Copyright Clearance Center.

License Number 5616001448445

License date Aug 25, 2023

Licensed Content

Publisher John Wiley and Sons

Licensed Content

Publication Medical Physics

Licensed Content

Title **Technical note: System uncertainty on four- and eight-channel parallel RF transmission for safe MRI of deep brain stimulation devices**

Licensed Content

Author Benson Yang, Chih-Hung Chen, Simon J. Graham

Licensed Content

Date Jul 19, 2023

Licensed Content

Volume 0

Licensed Content

Issue 0

Licensed Content

Pages 7

Type of use Dissertation/Thesis

Requestor type Author of this Wiley article

Format Electronic

Portion Full article

Will you be translating? No

Title PhD Thesis

Institution name McMaster University

Expected Dec 2023 presentation date

Requestor Location Benson Yang 2075 Bayview Avenue, S652a Toronto, ON M4N 3M5 Canada Attn: Benson Yang

Publisher Tax ID EU826007151

Total 0.00 USD